EXACT SOLUTIONS FOR AXISYMMETRIC AND NONPOLYTROPIC ASTROPHYSICAL WINDS

João José de Faria Graça Afonso Lima

A Thesis Submitted for the Degree of PhD
at the
University of St Andrews

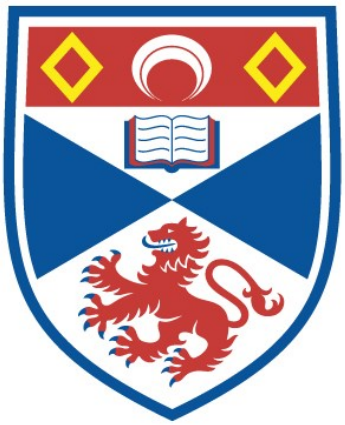

1995

Exact Solutions for Axisymmetric and Nonpolytropic Astrophysical Winds

João José de Faria Graça Afonso Lima

December, 5 1994

Submitted for the degree of Doctor in Philosophy

In Memory of José Baptista

Abstract

Astrophysical outflows are common in a large variety of objects with very different length-scales. They can be almost spherical, as in the case of the solar wind, or show a high degree of anisotropy as in pre-main sequence stars, star-forming regions or even extragalactic objects.

This work is aimed at finding exact solutions of the axisymmetric wind equations in which all variables depend not only on the distance to the central object but on latitude as well. The geometry of the stream/field-lines is taken as helicoidal and this seems to be a good approximation in some examples of collimated flows.

From a simple hydrodynamic approach, a straighforward technique based on separation of the variables yields the most general solution of the wind equations under the above assumptions. The way the different variables depend on latitude is controlled by three anisotropy parameters which are related to typical ratios at the base of the atmosphere. The density needs to be higher at the equator than at the pole for the outflow to be able to accelerate. In these circumstances, the radial velocity always increases from equator to pole. Contrary to Parker's model of the solar wind, the solution does not pass through any critical point, since no polytropic law is assumed. However, the general behaviour is similar, with a high acceleration at the base and the velocity rapidly attaining an almost constant asymptotic value. The heating rate that sustains this rapid increase is mostly concentrated near the surface of the central object.

The inclusion of the magnetic field in the analysis introduces two critical points: the Alfvenic point and an extra $X-$type point filtering the solution that gives a vanishing pressure at infinity. If the density anisotropy is too low the wind is unable to accelerate to large asymptotic values. The dependence of the angular velocity of the roots of the fieldlines with latitude reproduces well the observed rotation profile of photospheric magnetic features. The mass loss rate can be substantially increased if the structure of the outflow is highly anisotropic.

Some applications to the solar wind are also discussed. In particular, recent results from *ULYSSES* (pointing out that solar speed increases with latitude while the density decreases from equator to the pole) are in good agreement with the general behaviour of the solutions presented in this work.

Declaration

In accordance with the regulations of the University of St Andrews as of December 1993,

1. I, João José de Faria Graça Afonso Lima, hereby certify that this thesis has been composed by myself, that it is a record of my own work, and that it has not been accepted in partial or complete fulfilment of any other degree or professional qualification.

   Signed: Date: 7th Dec 1994

2. I was admitted to the Faculty of science of the University of St Andrews under Ordinance General No 12 in October 1990 and as a candidate for the degree of PhD on the same date.

   Signed: Date: 7th Dec 1994

3. I hereby certify that the candidate has fulfilled the conditions of the resolution and regulations appropriate to the degree of PhD.

   Signed: Date: 7.12.94

4. In submitting this thesis to the University of St Andrews I understand that I am giving permission for it to be made available for use in accordance with the regulations of the University Library for the time being in force, subject to any copyright vested in the work not being affected thereby. I also understand that the title and abstract will be published, and that a copy of the work may be made and supplied to any bona fide library or research worker.

Acknowledgments

These last few years in St.Andrews have proved to be a very enjoyable experience. I'm grateful to everybody at the Solar Group in St.Andrews that made this possible. In particular, special thanks to my supervisor Prof. Eric Priest for his guidance and constant support, my office mates Craig, Nick and Apollonia and the five-a-side football group.

I was also privileged to meet new friends, like Shaun and Steph, with whom shopping was always an exciting experience, Luis and all those long discussions during tea break (or how will Portugal qualify for the World Cup 94 ?), António always trying to play golf in two different courses at the same time, and Charles and his exquisite concept of a football team (Wimbledon !)... or keep in touch with old ones and specially Vítor. Thanks also to all Living Dead players and the Ardgowan bunch.

Special thanks to Prof. Kanaris Tsinganos for his warm welcome in Crete and also Cristophe and Giorgos who helped me during my stay there. My deep gratitude also to Prof. Teresa Lago, by making it possible for me to follow my studies in Astronomy and to everybody at the Centre for Astrophysics in Porto.

Finally, all this effort would be meaningless without the support of my family and Carmina.

The author wishes to acknowledge a grant from *Junta Nacional de Investigação Científica e Tecnológica* – BD/732/90-RM, funds from the *Science and Engineering Research Council* and from the *Erasmus* Programme.

Contents

Chapter 1

Introduction

1.1 Observations

1.1.1 The Concept of Solar Wind

Since early days the Sun has been the object of much fascination. Phenomena like sunspots have been observed and recorded for over two millenia. While the mechanisms behind such events were largely unknown, the amount of data collected over the years meant that the nearest of the stars was also the best understood.

In the first half of this century, the term "solar corpuscular radiation" was widely adopted to explain polar aurorae, geomagnetic storms and even the modulation of the emission of cosmic rays. Such emissions of particles were thought to be temporary rather than having a continuous nature. In the 1950's new observations suggested that the zodiacal light was strongly polarized. This was attributed to the scattering of sunlight by electrons (Behr and Siedentopf 1953). At about the same time, observations of the ionic tails of comets showed them to be always pointing away from the Sun. In order to explain this phenomenon, Biermann (1951, 1953) suggested that both the acceleration and ionization of the molecules in the comet's tail was a result of the interaction of the tail with a continuous flow of ions from the Sun. Such a flow with velocities ranging from 500 to 1500 km s^{-1} would also rule out the presence of any stationary interplanetary gas (Biermann, 1957).

One of the first attempts to model the solar corona was undertaken by Chapman (1957) who considered a static and spherically symmetric model, while recognizing that the actual corona is dynamic and asymmetric. By then observations had established that coronal temperatures are of the order of $10^6 K$. Under these conditions the electron conductivity is extremely high. Making use of this fact, Chapman solved the static equilibrium equations for a fluid subject to gravity and for which energy transfer is by conduction. For reasonable values of temperature and density at the base of the corona, his solution yields values of the pressure near the earth of around 10^{-5}dynes cm^{-2}. This corresponds to 7 or 8 orders of magnitude greater than the average pressure of the interstellar medium and indicates that this model is unable to blend into

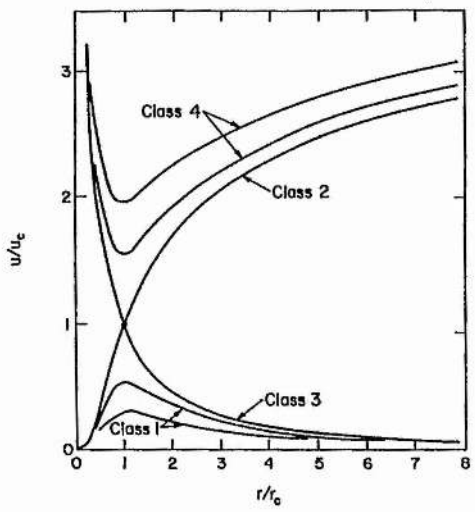

Figure 1.1: Solutions of the solar wind equations as in Parker (1963) (taken from Hundhausen (1972))

its background.

Motivated by Biermann's suggestions and the pressure mismatch in Chapman's static model, Parker (1958a) argued that the solar corona couldn't be in complete hydrostatic equilibrium out to large distances. He proposed a continuous outward expansion of gas from the Sun, which he called the Solar Wind (Parker, 1958b). This would be a natural consequence of the very high temperatures prevalent in the solar corona. His ingenious model starts by taking the equation of motion for a steady expansion of the corona, which he assumes to be isothermal as a first approximation. Using mass conservation he arrives at the solution illustrated in Fig.1.1.

Since the relevant solution must start with low velocities at the base of the corona and attain high values asymptotically, as suggested by Biermann, Parker (1963) argues that it must pass through the critical point (r_c, u_c) with positive slope (solution of Class 2 in Fig.1.1). This point is coincident with the sonic point (*i.e.* the point where the flow speed equals the sound speed of the plasma) and the corresponding solution is often referred as the supersonic expansion of the corona. Such a solution gives zero pressure at infinity and is thus able to merge with the low pressure of the interstellar medium. Note that solutions of Class 1, also called "solar breezes", lead to finite pressures at large distances and are thus unable to merge with the interstellar background. They show the same mismatch as Chapman's static model. Also, they correspond to subsonic values of the velocity u at large distances. Finally, solutions of Classes 3 and 4 are overruled since they correspond to supersonic values of the velocity close to the Sun.

For the solution of interest, Parker showed that velocities of a few hundred $\mathrm{km\,s^{-1}}$ at the orbit of the Earth could result from coronal temperatures of the order of $10^6 K$. This was in

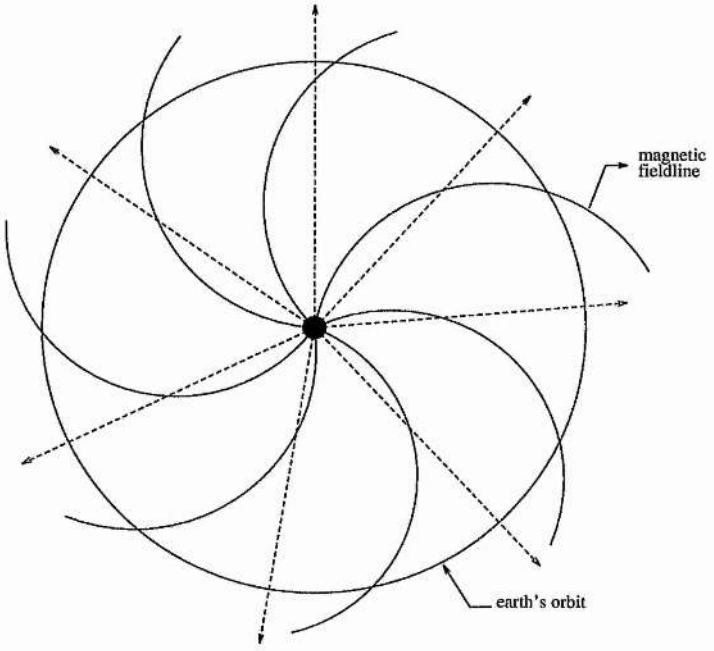

Figure 1.2: Magnetic fieldline geometry for a rotating Sun

close agreement with Biermann's suggestions regarding the motion of comet tails. However, the resulting electron density at the Earth's orbit is now known to be to high by at least a factor of 10^2. Such a discrepancy is related to the assumption of an isothermal corona. Later he relaxed this assumption by constructing a model which is isothermal close to the base and adiabatic at large distances. Parker's ideas were largely contested at the time but were later confirmed by observations carried out firstly by Lunik III and Venus I in 1959 and later by Mariner 2 in 1962. This latter set of observations as reported by Neugebauer and Snyder (1966) corresponded to three continuous months of data and showed that (i) a solar wind is present at all times, (ii) the outflow speed varies between 300 and 800 km s^{-1} with an average of 500 km s^{-1}, (iii) this velocity is correlated with geomagnetic activity, (iv) the average proton density is about 5 cm^{-3}.

In the original article Parker (1958a) also investigated the effect of the outflow of gas upon the general form of the interplanetary magnetic field. Due to the high electrical conductivity of the plasma, the magnetic field lines are "frozen-in" to the plasma (see Sect.1.3). Thus a magnetic field line from a given area on the sun will be drawn out along the path folowed by the fluid elements emanating from that area. Assuming a spherically symmetric outflow of material and taking account of the rotation of the Sun, the resulting geometry of the field lines corresponds to an Archimedean spiral (Fig.1.2). The surface on which each field line makes an angle of 45° with the radius vector was estimated by Parker to be at around 2.5 a.u.

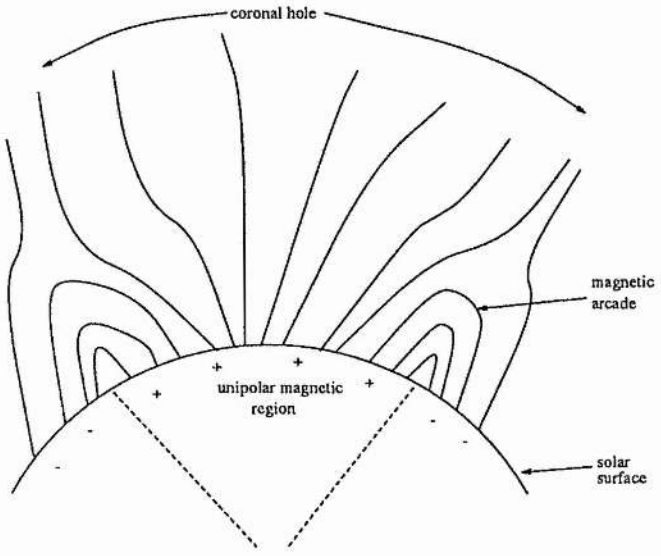

Figure 1.3: Schematic diagram of a coronal hole surrounded by a pair of magnetic arcades

1.1.2 Coronal Holes and High-Speed Streams

Coronal holes are regions of lower density and temperature than the surrounding corona and are associated with open magnetic field lines. They were first recognized by Waldmeier (1957) using synoptic maps of the monochromatic corona. For a review of their properties see Bohlin (1976) and Priest (1982).

Skylab observations (coinciding with the decline of the solar cycle) suggested that coronal holes cover a substantial part of the solar surface. Nearly 20% of the sun was covered by coronal holes, while there was an essentially constant area of 15% covered by polar ones (Bohlin, 1976). They also seem to have a long lifetime reaching in some cases 10 solar rotations. Differential rotation in coronal holes is negligible when compared with other solar features like sunspots. The emergence of coronal holes is associated with the development of active regions. When the active region is wide enough, the hole may arise between a set of coronal arcades and over a unipolar magnetic region. If this region is narrow than the gap between the arcades can be covered by a single coronal straemer and no coronal hole is formed (Bohlin and Sheeley Jr., 1978). The resulting geometry is sketched in Fig.1.3.

The most important property of coronal holes is their association with high-speed streams. In fact some have been identified as the source of several of these recurrent supersonic streams (Krieger et al., 1973). In order to explain how such a low density hole can provide such acceleration, Kopp and Holzer (1976) suggested that the boundaries of coronal holes might diverge appreciably faster than r^2 near the base of the corona. Under these conditions new critical points

may arise, in addition to the Parker-type solar wind point. These reflect the interplay between gravitational and area-change terms in the equations. Thus the supersonic transition may occur in one of these extra critical points, before the Parker-type point, while the flow will remain supersonic beyond then.

The properties of a specific coronal hole were studied in detail by Munro and Jackson (1977). They found that the increase of the polar hole's cross section between the surface to $3R_\odot$ is about 7 times greater than for a radial boundary. From 3 to $6R_\odot$ the hole is almost radial. This means that 60% of the solar atmosphere in the northern hemisphere above $3R_\odot$ is connected to only 8% at the solar surface. Their results show that the transonic point lies between 2.2 and $3.0R_\odot$ for coronal temperatures between 10^6 and $2.5 \times 10^6 K$. The corresponding velocity at $5R_\odot$ is a factor of two larger than the velocity of a radially flowing isothermal solar wind model (Parker, 1958a) with $T = 2 \times 10^6 K$.

1.1.3 General Properties of the Solar Wind

The form in which the solar corona expands as a wind is dependent on the stage of the solar cycle. As sunspot minimum approaches, the configuration is dominated by both polar coronal holes (one in each pole) which are connected at large distances by a neutral current sheet. In this case the sheet is almost flat and shows a small inclination with respect to the solar equator (Mihalov et al., 1990; Suess et al., 1993). After solar minimum, it deviates rapidly from that orientation and becomes warped around the equator. An observer at the earth sees a sequence of alternating polarities which are associated with the flow coming from different sides of the current sheet. Towards solar maximum, the activity increases and consequently also the number of coronal holes.

On the basis of various parameters measured at the Earth's orbit, the solar wind flow inside 1 a.u. can be separated into one of three different classes: high-speed streams, low-speed streams and transient solar wind (Hundhausen et al., 1971; Withbroe et al., 1991). The first class, described in the previous section, corresponds to flow speeds of the order of 700 $\mathrm{km\,s^{-1}}$ at the Earth's orbit and is associated with a steady-state emission originating from coronal holes. Low-speed streams have much lower velocities of the order of 300 $\mathrm{km\,s^{-1}}$. There are strong suggestions that these originate in streamers or in the interface between these and other regions. Evidence for this relies heavily on observations of polarity reversals in the solar wind which were traced back to the location of streamers (Gosling et al., 1981). Transient flows resulting from solar flares and in general coronal mass ejections are an important source of the variable component of the solar wind although they only contribute to about 5% of the mass loss from the Sun. For a summary of the various parameters of the solar wind see Table1.1.

There are strong suggestions that the wind speed increases with latitude, at least around solar minimum. Coles et al (1980) investigated the variation of the solar wind with the solar cycle. Using an indirect method based on interplanetary scintillation, they concluded that the wind

Parameter	Low Speed	High Speed	Average
n (cm^{-3})	11.9	3.9	8.7
V ($km\,s^{-1}$)	327	702	468
nV ($10^8\ cm^{-2}\ s^{-1}$)	3.9	2.7	3.8
T_p ($10^5\ K$)	0.34	2.3	1.2
T_e ($10^5\ K$)	1.3	1.0	1.4
B ($10^{-5}\ Gauss$)	6.2	6.2	6.2

Table 1.1: Solar wind parameters at the orbit of the earth (Feldman et al 1977)

speed is lower near the equator than for higher latitudes. Such a difference was more drastic during the years of declining activity (see also Rickett and Coles (1991)) Observations carried out by Pioneer 10 and 11 close to the ecliptic suggest an average heliomagnetic latitude gradient in the solar wind speed of the order of 17 $km\,s^{-1}$/deg (Mihalov et al., 1990). This was attributed to a displacement of the neutral sheet relative to the equator. A similar trend was encountered using data from the Pioneer Venus orbiter and IMP 8 (Gazis, 1993).

Launched in October 1990, *ULYSSES* is the first probe aimed at mesuring the solar wind properties away from the ecliptic and in the polar regions. On its way to the south pole, its first observations clearly indicate a pronounced increase with latitude in the maximum speed of a major high-speed stream (Bame et al., 1993). The average speed of the wind increases typically from around 450 $km\,s^{-1}$ just below the ecliptic to values close to 750 $km\,s^{-1}$ for latitudes close to 56° S (McComas et al., 1994; Goldstein et al., 1994; Phillips et al., 1994). The corresponding latitudinal gradient is higher near the equator, while closer to the pole the velocity distribution flattens out to an almost constant value. The minimum speed of the persistent solar wind also reveals a slight increase from the equator to the south pole. Also important is the detection of a substantial variation of the average proton density with latitude, decreasing towards the pole.

These recent observations call for 2D models of the solar wind that take into account the above trends for both the velocity and density distributions.

1.1.4 Winds in Other Stars

The case for nonradiative heating processes from other stars has been studied in detail by Linsky (1985). He argued that solar-like stars (defined as stars with turbulent magnetic fields strong enough to control the dynamics and energetics in its outer atmospheric regions) are common in almost all spectral types. Dwarf stars of spectral types G, K and M have measured magnetic fields. Those of spectral type A7-F7 show solar-like indirect indicators. Other groups of stars which are clearly solar-like include the rapidly rotating subgiants of spectral type F, G and early

K in spectroscopic binaries (e.g. RS CVn and W UMa) and active Pre-Main Sequence stars (e.g. T Tauris). The hot A and B stars, A dwarfs and cool giants and supergiants show no evidence of being solar-like. We should note that for most of these stars there is no direct measure of the magnetic field strength. These conclusions are mainly based upon indirect indicators of magnetic activity such as the photometric variability on rotational time scales, indicating the presence of dark spots or nonthermal microwave and X-ray emission.

In terms of the type of wind they emit we can divide stars in three different classes (Dupree, 1986). The first one comprises the hot OB stars. Since they don't have a convection zone, their violent winds must have a radiative nature. The second class corresponds to the main sequence stars. There is no direct detection of winds in any of these stars, with a convective structure similar to our sun. It is often assumed that since these show evidence of the presence of a corona (*e.g.* by the detection of X-ray flux) they must posess some kind of solar type wind. Also, the X-ray flux is in some way related to the rotation and is thus probably due to dynamo action, as in the case of the Sun. Finally, the third group includes cold giants and super-giants. Their winds are massive and slow, with no associated emission in X-rays.

1.1.5 From Winds to Jets

The presence of collimated flows is very common in astrophysical objects, namely stellar objects (Paresce and Nota, 1989) and star-forming regions and associated young stars (see Reipurth (1989), Mundt et al (1990) and reviews by Mundt (1986) and Bachiller and Gómez-González, (1992)). These outflows, assuming sometimes the characteristics of jets, show similar properties, namely very small length-scales of collimation and association with accretion disks. In the case of pre-main sequence stars of low-to-medium luminosity, high-velocity jets with collimation length scales as low as 100 A.U. are often observed. Sometimes Herbig-Haro (HH) objects are powered by these jets or simply appear as bright knots in the jet structure. Certain sequences of HH objects show a helicoidal distribution, which can be explained if the jet itself has such a geometry or else due to precession of the source.

One important class of pre-main sequence stars often associated with outflows that show a high degree of anisotropy are T Tauri stars.

T Tauri stars

T Tauri stars are low-mass pre-main sequence stars that show a high degree of variability. Alfred Joy discovered them in the Taurus-Auriga cloud and named the class after its brightest member, T Tauri (Joy, 1945). Because they're very young stars that only recently have become visible in the optical region, they are often seen projected onto nebulosities. For an extended review on their properties, see Bertout (1989).

Rotation in T Tauri stars is surprisingly low if we take into account their strong activity and young age. Rotational speeds are an order of magnitude or more below breakup velocity.

This means that newly formed stars must loose a substantial part of their primordial angular momentum during contraction to the main sequence and before the T Tauri phase. Strong winds could acoount for this braking. In other words, the angular momentum problem has been solved at an earlier phase of evolution than represented by the T Tauri stars (Vogel and Kuhi, 1981). Although this first survey imposed upper limits on $v \sin i$ of about 25 $\mathrm{km\,s^{-1}}$, Bouvier et al (1986) improved on this resolution. Their work revealed a distribution of rotational velocities for low-mass T Tauri stars ($M < 1.25 M_{\odot}$) ranging from 6 to about 30 $\mathrm{km\,s^{-1}}$ and with a peak at around 15 $\mathrm{km\,s^{-1}}$. For high mass T Tauri's, they've found velocities from 15 to 75 $\mathrm{km\,s^{-1}}$. Hartmann et al (1986) reported on a survey of 50 T Tauri's. The great majority of low-mass stars ($M < 1.0 M_{\odot}$) show values of $v \sin i < 20$ $\mathrm{km\,s^{-1}}$, with higher-mass stars exhibiting larger velocities than lower-mass ones.

It is believed that, after the T Tauri phase, low-mass stars will spin-up on their radiative evolutionary tracks, during contraction towards the main sequence where they arrive with rotational velocities of 20 to 100 $\mathrm{km\,s^{-1}}$, in agreement with the values found for Pleiades K dwarfs. These observations support a general picture by which low-mass stars are either born slowly rotating or are spun down very quickly at an early age (*i.e.* before the T Tauri phase). They subsequently spin up quite dramatically during contraction to the main sequence, where they undergo a rapid phase of spin-down (Hartmann and Noyes, 1987).

There are strong suggestions that magnetic fields might play a leading role in the variability observed in T Tauri stars. If this is the case, then rotational velocity will be a crucial parameter determining the strength of a dynamo-generated magnetic field. Bouvier (1989) found a correlation between X-ray emission and rotation in T Tauri's similar to the one derived for other late-type active dwarfs and RS CVn systems. He proposed that this is the result of a solar-type magnetic dynamo operating in T Tauri stars, with rotation as the governing parameter. Attempts to observe the photometric variability of T Tauri stars on time scales comparable to the rotational period have revealed both regular and irregular light variations taking place on time scales of days to weeks (Bouvier and Bertout, 1989). This modulation was attributed to the presence of dark spots on the stellar surface, a direct indicator of strong magnetic fields. In their sample of nine T Tauri stars, Bouvier and Bertout found that the fractional area covered by spots ranges from 3 to 17% of the total stellar surface, while they are typically $750K$ colder than the surrounding phostosphere. These values are similar to the ones found in RS CVn systems. For comparison, sunspots cover a much smaller area of the solar surface ($< 1\%$) and are significantly colder than spots on late-type active stars, with a temperature difference close to $1800K$.

In summary, observations of T Tauri's point to a scenario of a high degree of activity in which magnetic fields play an important role. In this sense they are sometimes seen as stars similar to our sun, just before the main sequence stage.

Be stars

From a different class of stars, Chen et al (1989) describe the wind of the B_e star λ Pavonis based on the profiles of UV spectral lines. They assign two different regions in its atmosphere, namely a region which is rotating and a region which is expanding. In the first one the radial velocity is close to zero whereas the rotational velocity increases monotonically. This increase outside the photosphere can only be explained by the presence of magnetic fields. In the expanding region rotation is no longer important, the wind is accelerated to a maximum and decelerates further out.

Ringuelet and Iglesias (1991) discuss the existence of a nonexpanding envelope surrounding Be stars. Apart from an expanding chromosphere their model incorporates also an outer cool envelope. Thus, the rotational velocity increases from the photosphere up to the Alfvén radius, due to the presence of a magnetic field. As the expansion velocity increases, dissipation sets in and the velocity is decelerated, though it does not necessarily decrease immediately, as is the case with λ Pav. In this dissipating region, there is a slight temperature rise but finally both T and V_{rot} decay fast so as to originate a non-rotating nonexpanding cool envelope.

Extragalactic Outflows

For objects of galactic dimensions the presence of jets is very common The length-scales of collimation for these objects are extremely small and the jets remain collimated up to large distances. They are usually associated with active galactic active and became known after the discovery of the optical jet of M87 (see for example Owen et al (1989)).

No fluid motion is directly measurable in extragalactic jets. Only proper motions of associated luminous structures can be estimated. The common scenario includes a massive central object with an associated accretion disk. Closer to this object and at distances of a few parsecs, the emission shows a series of nodes, often on only one side of the nucleous. Further away from the object (distances of the order of a kpc), nodes or filamentary structures are observed, from one or both sides of the emitting region, and independently of the structure at the scale of a pc. This jet finally extends into a lobe.

As in the case of stellar jets, there is evidence for the existence of a helicoidal magnetic field. In fact, the borders of the lobe show a magnetic field which is parallel to the axis of the jet, while in the central region it is essentially perpendicular to it. This could be easily explained by an effect of projection of a helicoidal field.

In summary, the fact that similar characteristics are found in collimated outflows emerging from objects with very different sizes suggests that a common physical mechanism is responsible for the appearence of this type of flow.

1.2 Theoretical Models for Stellar Winds

In Sect.1.1.1 we've already discussed the hydrodynamic model of Parker (1958a; 1963) describing the general expansion of the solar corona. Weber and Davis (1967) improved on this model by including the effects of a magnetic field. The geometry of the magnetic field is assumed radial in the meridional plane ($B_\theta = 0$) - a split-monopole. Since they only considered the flow near the equatorial plane, the model is one-dimensional (1D). All forces perpendicular to this plane are ignored. The energy equation is approximated by the polytropic law. The final solution passes through three critical points. The first is the slow mode critical point, where the fluid velocity equals the velocity of propagation of the slow wave. This is slightly less than the pure sound speed (Parker's critical point) since, due to the presence of the magnetic field, the sound wave is transformed into a magneto-acoustic wave. The second critical point is the Alfvenic point, where the speed equals the radial Alfvén velocity. Finally, the third critical point is the fast mode critical point; here the velocity equals the speed of propagation of the fast wave. This is very nearly equal to the Alfvén velocity which is slightly larger than the radial Alfvén velocity. Both the slow and fast mode singularities are of X-type. The Alfvenic singularity is of higher order. The torque exerted by the magnetic field in the equatorial plane leads to the spin down of the sun with a time-scale of 7×10^9 yr. However, this model is unable to reproduce the physical conditions both at the Earth and at the Sun, or in other words, the energy supply given by any constant value of γ is incorrect. Another constraint of this model is related to the fact that no cross-field equation was solved; the force-balance perpendicular to the poloidal magnetic field (θ direction) was not considered. Only the r- and ϕ-components of the momentum equation were solved.

Pneuman and Kopp (1971) solved numerically the hydromagnetic equations for a helmet streamer type configuration. Their three-step iterative technique was based on the assumption of an isothermal atmosphere with the neglect of solar rotation.

Sakurai (1985; 1990) proposed a two-dimensional generalisation of the Weber and Davis model. This work presents a method to solve the 2-D wind problem numerically (steady, axisymmetric model with frozen-in magnetic fields). It constitutes a natural extension of the 1-D Weber-Davis model (Weber and Davis, 1967) and satisfies the cross-field balance of forces. The magnetic field is assumed of split-monopole geometry. The wind solution along the magnetic field is given by the Bernoulli equation which presents two critical points: the slow mode and the fast mode critical points. The equation of force balance across the field lines is singular at the Alfvén point, and the two regularity conditions there are obtained by using l'Hospital's rule. These are sufficient to determine the magnetic flux function (and thus the shape of the magnetic field), without assuming any conditions at infinity (this is so because the flow far from the star is faster than the fast mode speed, so that no MHD signal can propagate upstream - the solution there is completely determined by the condition within this critical point). The results show a poleward deflection of the flow due to the build up of toroidal magnetic field in the wind. The flow is collimated. This

is a result of the fact that both the magnetic pressure and the magnetic tension due to B_ϕ are directed towards the pole and constrain the outflow. It also means that the cross section of the flow channel near the rotation axis becomes smaller than for radial expansion. The acceleration is smaller near the pole and all three critical surfaces are pushed out. Near the equator the opposite holds: a wider opening of the flow channel, higher acceleration and critical surfaces pushed inwards. The mass flux per unit magnetic flux is also enhanced near the equator. Due to the strong pinching force, a polar column of high density gas is formed around the rotational axis. Similar results were shown to be valid in the case of a wind from an accretion disk (Sakurai, 1987). In the solar case, this concentration of higher density material around the pole contradicts recent solar observations obtained by *ULYSSES* suggesting a distribution of density that increases from pole to equator (Sect. 1.1.3).

Heyvaerts and Norman (1989) have established that any stationary axisymmetric magnetized wind will collimate along the symmetry axis for large distances from the central object. Only for singular solutions or those with a vanishing poloidal current, can the asymptotic form be paraboloidal. All the other cases show a cylindrical geometry. In a complementary study, Sauty and Tsinganos (Sauty and Tsinganos, 1994) have presented a criterion in terms of the distribution of energy across the streamlines in the meridional plane, for the transition of the asymptotic geometry of the outflow from the radial one of a classical wind to the cylindrical shape of a jet.

Global solutions describing steady hydromagnetic flows in open magnetic fields were presented by Low and Tsinganos (1986). Rotation was ignored and the magnetic field was assumed purely poloidal. The novel approach was to deduce the heating rate self-consistently from the equations rather than adopting a polytropic law. Also, density was taken as spherically symmetric and the resulting solutions showed either zero or a low terminal speed. This also was the case when the model was improved with the inclusion of static zones (Tsinganos and Low, 1989). The argument is as follows. A dipolar magnetic field needs to be kept open by a pressure that must decrease towards the pole. If the density does not vary with latitude, there is a smaller pressure gradient to drive the flow near the pole, exactly where the magnetic field is open to allow the wind to escape. The resulting acceleration is too low, since gravity dominates, and the flow does not reach a high enough terminal speed. The only way out is to allow density to increase with latitude, faster than the pressure (Tsinganos and Vlastou-Tsinganos, 1988; Hu and Low, 1989).

Tsinganos and Trussoni (1990) have looked at solutions of the hydrodynamic set of equations for a helicoidal geometry of the streamlines. The latitudinal dependence of the different quantities was assumed *a priori*. Thus, the increase of the radial speed from equator to poles (as in jets), and the increase of the density towards the equator (as in disks), was controlled by a single parameter. Such a choice for the density distribution was in part motivated by earlier observations of a coronal hole at sunspot minimum (Munro and Jackson, 1977). The solution does not pass through any critical point since the energy exchange mechanisms in the plasma are not constrained by the polytropic assumption. Allowing for flaring streamlines, by including both components of the poloidal speed, Tsinganos and Sauty (1992a) have shown that only those streamlines that initially

converge towards the pole contribute to the acceleration of the outflow. If, on the contrary, they converge to the equator, there is an initial deceleration and lower asymptotic speeds, contrary to what happens in polytropic flows. In any case, asymptotically they become radial.

The model was later extended with the inclusion of a magnetic field and keeping the same helicoidal geometry (Tsinganos and Trussoni, 1991). In this case the wind solution (with zero pressure at infinity) must pass through two critical points. The first one is the familiar Alfvenic point where the flow speed equals the Alfvenic speed. The second is an X-type point which seems to be associated with the slow/fast MHD mode wave speed (Tsinganos, 1994). A more general model including the effects of V_θ and B_θ but ignoring rotation was later developed by the same authors (Trussoni and Tsinganos, 1993), while a detailed topological analysis of the equations in the case of spherically symmetric pressure and neglecting rotation has been presented by Tsinganos and Sauty (1992b) (see also Tsinganos et al (1993)).

Following a slightly different approach, Lima and Priest (1993) have looked for the most general solution of the hydrodynamic equations relevant for stellar winds with a helicoidal geometry. This work generalizes Tsinganos and Trussoni (1990) model for a general density and velocity distributions. The development of this model will be presented in detail in Chapter 2. The inclusion of a general helicoidal magnetic field is the subject of Chapter 3 (Lima and Priest, 1994).

1.3 MHD Equations and Assumptions

The mathematical description of most wind problems is based on the MHD approach. This requires the plasma to be quasi-neutral and dominated by collisions and the typical velocities non-relativistic. The basic equations in this treatment are Maxwell's equation for the divergence of the magnetic field, the induction equation, plus a set of plasma equations describing conservation of mass, momentum and energy. The system is usually closed by an equation of state.

The first of these equations simply states that there are no magnetic monopoles, or in mathematical terms

$$\nabla \cdot \mathbf{B} = 0, \tag{1.1}$$

for the magnetic field **B**. The induction equation describes the interplay between the magnetic and velocity fields and assumes the form

$$\frac{\partial \mathbf{B}}{\partial t} = \nabla \times (\mathbf{V} \times \mathbf{B}) + \eta \nabla^2 \mathbf{B}, \tag{1.2}$$

where η is the magnetic diffusivity. The first term on the right-hand side of the above equation is called the convective term, while the second term is the diffusive term. A straigthforward dimensional analysis of the above equation shows that the ratio of the convective to the diffusive term is equal the so-called magnetic reynolds number $R_M = L_0 V_0/\eta$, where L_0 and V_0 are typical length-scales and velocities of the plasma. In the limit of large length-scales, R_M is very large and the convection term dominates over the diffusive term. This means that the plasma is frozen-in to the magnetic field. It moves freely along the field lines while for motion perpendicular to **B** both the plasma and the magnetic field move together. We will use the induction equation under this limit.

The plasma equation for conservation of mass states the fact that there are no sources or sinks of mass and can be written as

$$\frac{\partial \rho}{\partial t} + \nabla \cdot (\rho \mathbf{V}) = 0, \tag{1.3}$$

where **V** is the velocity and ρ the density. The momentum equation in the limit of negligible viscosity takes the form

$$\rho \frac{D\mathbf{V}}{Dt} = -\nabla p + \frac{1}{4\pi}(\nabla \times \mathbf{B}) \times \mathbf{B} - \frac{\rho G M}{r^2}\hat{\mathbf{e}}_r, \tag{1.4}$$

where p denotes the pressure, r the radial distance to the central object, M the mass of the central object and G the gravitational constant.

Note that in the above equation we have used the so-called material derivative defined as

$$\frac{D}{Dt} \equiv \frac{\partial}{\partial t} + (\mathbf{V} \cdot \nabla) \tag{1.5}$$

This denotes the time rate of change following the motion of the volume of fluid. In terms of variables fixed in space, this rate of change is composed of two parts: the first term on the right-hand side of Eq.(1.5) corresponds to the change at a fixed point in space, while the second term represents the difference between the two values of the given quantity (at the same instant) for two points $d\mathbf{r}$ apart, where $d\mathbf{r}$ is the distance moved by the above volume during the time dt. This second term is often called the convective derivative.

The momentum equation, Eq.(1.4), expresses the fact that the rate of change of the velocity following the motion equals all the forces per unit mass that act on the fluid, namely in our case the presure gradient, the Lorentz force and the gravitational force.

Finally, the energy equation can be expressed as

$$T\frac{\mathrm{D}s}{\mathrm{D}t} = \frac{\mathrm{D}Q}{\mathrm{D}t}, \tag{1.6}$$

where T is the temperature, s the entropy per unit mass of the fluid and Q is the heat content per unit mass of the fluid. This equation states that the rate of change of entropy following the motion of the volume of fluid equals the rate of external energy addition (sources minus sinks). In a transition where the heat gains are balanced by the losses, the entropy is conserved and the transition is said to be adiabatic.

To be able to use the above equation we must define the entropy in terms of measurable quantities. Starting with the familiar thermodynamic relation

$$\mathrm{d}Q = \mathrm{d}e + p\mathrm{d}v, \tag{1.7}$$

where e is the internal energy per unit mass and $v = 1/\rho$ is the specific volume, we shall procceed to introduce the concept of an ideal gas. For such a gas the internal energy, e, is the sum of the separate energies of the different molecules and independent of the distances between them, i.e. independent of ρ. The highly ionized atmosphere around an astrophysical object can be regarded as an ideal gas to a very high degree of approximation. Under these conditions it is found that both the internal energy and the ratio p/ρ are functions of temperature only

$$e \equiv e(T) = c_v T \tag{1.8}$$

$$\frac{p}{\rho} = \frac{k_B}{m} T, \tag{1.9}$$

where k_B is the Boltzmann's constant, m is the mean particle mass and c_v is the specific heat at constant volume defined by

$$c_v = \left(\frac{\partial Q}{\partial T}\right)_v = \left(\frac{\partial e}{\partial T}\right)_v, \tag{1.10}$$

the last equality arising from Eq.(1.7). Analogously, the specific heat at constant pressure c_p is defined by

$$c_p = \left(\frac{\partial Q}{\partial T}\right)_p = \left(\frac{\partial e}{\partial T}\right)_p + p\left(\frac{\partial v}{\partial T}\right)_p. \tag{1.11}$$

For an ideal gas, substitution of Eqs.(1.8), (1.9) into Eq.(1.11) yields

$$c_p = c_v + \frac{k_B}{m}. \tag{1.12}$$

Also the ratio of specific heats is defined as

$$\Gamma = \frac{c_p}{c_v}. \tag{1.13}$$

From Eq.(1.8), (1.9), (1.12), (1.13) it is straightforward to deduce an expression for the internal energy per unit mass for an ideal gas

$$e = \frac{1}{\Gamma - 1}\frac{p}{\rho}. \tag{1.14}$$

Finally, if we define $\sigma = \mathrm{D}Q/\mathrm{D}t$ as the rate at which energy is added into the fluid per unit mass we can re-write Eq.(1.6) as

$$\frac{D}{Dt}\left(\frac{p}{(\Gamma-1)\rho}\right) + p\frac{D}{Dt}\left(\frac{1}{\rho}\right) = \sigma. \tag{1.15}$$

Note that all the equations introduced up to now are time-dependent. However, the general characteristics of the astrophysical winds we will be interested in studying do not vary significantly with time. Most fluctuations are believed to be small-scale effects which do not affect the overall configuration of the outflow. Bearing this in mind we will turn our attention to the steady state solutions of the MHD equations, i.e. with $\partial/\partial t = 0$. Re-writing these equations under this assumption, we have

$$\nabla \cdot \mathbf{B} = 0, \tag{1.16}$$

$$\nabla \times (\mathbf{V} \times \mathbf{B}) = 0, \tag{1.17}$$

$$\nabla \cdot (\rho \mathbf{V}) = 0, \tag{1.18}$$

$$\rho(\mathbf{V} \cdot \nabla)\mathbf{V} = -\nabla \mathbf{p} + \frac{\mathbf{1}}{4\pi}(\nabla \times \mathbf{B}) \times \mathbf{B} - \frac{\rho \mathbf{G}\mathbf{M}}{\mathbf{r^2}}\hat{\mathbf{e}}_\mathbf{r}, \tag{1.19}$$

$$(\mathbf{V}\cdot\nabla)\left(\frac{p}{(\Gamma-1)\rho}\right)+p(\mathbf{V}\cdot\nabla)\left(\frac{1}{\rho}\right)=\sigma, \tag{1.20}$$

$$p=\frac{k_B}{m}\rho T. \tag{1.21}$$

The above equations will be the starting point of the models developed in the following chapters.

1.4 General Overview

We've seen in the previous sections how Parker's ingenious and simple model of the solar wind opened up a whole new area in astrophysical plasmas. Observations indicate that winds can go from the almost spherically symmetric solar wind to highly collimated outflows common at very different lengthscales. Thus, any realistic model must include the dependence both with distance to the central object as well as with latitude.

Starting with a simple hydrodynamic model (Chapter 2) we intend to seek general solutions of the axisymmetric equations governing the dynamics of winds. Apart from using helicoidal geometry for the streamlines, the minimum possible number of assumptions regarding the form of the various physical quantities will be used. Chapter 3 generalizes this model by including the effect of the magnetic field. Several applications will be discussed in Chapter 4, while Chapter 5 will be devoted to the final conclusions and discussion of future prospects of work.

Chapter 2

Hydrodynamic Model

2.1 Introduction

The main goal of this chapter is to find exact solutions of the steady hydrodynamic set of equations, relevant to the description of the dynamical state of an astrophysical wind. The model to be developed will be essentially two-dimensional, with all variables depending on both distance and the latitude. We will model the atmosphere surrounding the central rotating object as a compressible and inviscid fluid.

2.2 Basic Equations and Assumptions

The hydrodynamic equations describing the steady state of a fluid in the presence of the gravitational field of a central object are the equation of conservation of mass, the momentum equation, the energy equation and an equation of state. They constitute a special case of the system of Eqs.(1.16)-(1.21) in the case of a vanishing magnetic field **B**. We will write them down for easy reference

$$\nabla \cdot (\rho \mathbf{V}) = 0, \tag{2.1}$$

$$\rho(\mathbf{V} \cdot \nabla)\mathbf{V} = -\nabla p - \frac{\rho G M}{r^2}\mathbf{e}_r, \tag{2.2}$$

$$(\mathbf{V} \cdot \nabla)\left(\frac{p}{(\Gamma - 1)\rho}\right) + p(\mathbf{V} \cdot \nabla)\left(\frac{1}{\rho}\right) = \sigma, \tag{2.3}$$

$$p = \frac{k_B}{m}\rho T. \tag{2.4}$$

These six equations determine ρ, p, T and the three components of $\mathbf{V}$, for a given σ.

When $\sigma = 0$, there is no net rate of external energy addition and the change of state is called adiabatic. Under these conditions, Eq.(2.3) gives $p = K\rho^{\Gamma}$ along any streamline $\Psi = \text{const}$ (while K varies between streamlines). This corresponds to a polytropic relation between pressure and density with a constant polytropic index $\gamma = \Gamma$. In general $\sigma \neq 0$ and the polytropic index defined by

$$\gamma(r) = \left[\frac{\partial lnp}{\partial ln\rho}\right]_{\Psi=const} \tag{2.5}$$

is no longer a constant. Under these conditions the form of the heating rate is not restricted *a priori* so as to satisfy the polytropic law, but is deduced self-consistently from Eqs.(2.1)-(2.3) — see Tsinganos and Trussoni (1990), hereafter refered as TT90.

Appropriate for most astrophysical objects, we will use spherical polar coordinates (r, θ, ϕ), with θ as the co-latitude. Let us assume axial symmetry, *i.e.* $\partial/\partial\phi = 0$, which seems to be a very good approximation Another assumption will be to take the velocity field as helicoidal (*i.e.* $V_\theta = 0$). The expression "helicoidal" refers to the shape of the streamlines. Under this assumption they are helices around cones of opening angle θ. Their projections on the meridional plane are straight lines $\theta = \text{const}$. In fact, from Eq.(2.1) and the assumption of axisymmetry we can write the poloidal mass flux as

$$\rho \mathbf{V}_P(r,\theta) = \frac{1}{4\pi}\nabla \times \left(\frac{\Psi(r,\theta)}{r\sin\theta}\hat{\mathbf{e}}_\phi\right), \tag{2.6}$$

where $\Psi(r,\theta)$ is the Stokes stream function. The contours $\Psi(r,\theta) = \text{const}$ give the projections of the streamlines on the meridional plane (Tsinganos 1982). From Eq.(2.6) we obtain

$$\begin{aligned} \rho V_r &= \frac{1}{4\pi r^2 \sin\theta}\frac{\partial\Psi}{\partial\theta}, \\ \rho V_\theta &= -\frac{1}{4\pi r\sin\theta}\frac{\partial\Psi}{\partial r}. \end{aligned} \tag{2.7}$$

Thus, the condition $V_\theta = 0$ is equivalent to stating that the stream function Ψ depends only on θ, or in other words the streamlines projected on the poloidal plane correspond to contours $\theta = \text{const}$ (straight lines).

This last assumption of helicoidal fields is in good agreement with several pieces of observation. These include regions of star formation such as in HL Tauri (Mundt et al., 1990), stellar objects like AG Carinae (Paresce and Nota, 1989) or even galactic structures of the type of M87 (Owen et al., 1989). All of the above show bipolar outflows originating from the central object which could be supported by fields with helicoidal geometry.

Under the above assumptions, the system of equations, Eqs.(2.1)-(2.3) can be re-written as a system of 5 scalar equations in 5 unknowns (V_r, V_ϕ, ρ, p, and σ)

$$\frac{\partial}{\partial r}(\rho r^2 V_r) = 0, \tag{2.8}$$

$$\rho V_r \frac{\partial V_r}{\partial r} - \rho \frac{V_\phi^2}{r} = -\frac{\partial p}{\partial r} - \frac{\rho GM}{r^2}, \tag{2.9}$$

$$\rho V_\phi^2 \frac{cos\theta}{sin\theta} = \frac{\partial p}{\partial \theta}, \tag{2.10}$$

$$\rho V_r \frac{\partial V_\phi}{\partial r} + \rho \frac{V_r V_\phi}{r} = 0, \tag{2.11}$$

$$V_r \frac{\partial}{\partial r}\left(\frac{p}{(\Gamma - 1)\rho}\right) + p V_r \frac{\partial}{\partial r}\left(\frac{1}{\rho}\right) = \sigma. \tag{2.12}$$

This system can be supplemented by the Equation of state, Eq.(2.4) to determine the temperature T. The extra assumption $V_\theta = 0$ means that the heating rate σ can no longer be chosen freely but is instead determined by Eq.(2.12). In other words, the details of the energy exchange mechanisms in the plasma are not prescribed in our model. They are in any case highly uncertain and this enables us to obtain analytical solutions.

2.3 Method of Solution

Let us now denote the radius of the base of the atmosphere by r_0 and normalize all physical quantities with respect to their values at r_0. In particular, $R = r/r_0$. To transform the system of partial differential equations, Eqs.(2.8), (2.12), into a system of ordinary differential equations, we will assume that the remaining independent variables R and θ are separable. Thus, we can write the radial velocity as

$$V_r(R, \theta) = V_0 Y(R) v_r(\theta). \tag{2.13}$$

For conservation of mass, Eq.(2.8), the density must have the form

$$\rho(R, \theta) = \rho_0 \frac{g(\theta)}{Y R^2}, \tag{2.14}$$

while the ϕ-component of the momentum equation, Eq.(2.11) gives

$$V_\phi(R, \theta) = V_1 \frac{v_\phi(\theta)}{R}. \tag{2.15}$$

This represents the law of conservation of angular momentum. In the above equations, V_0, ρ_0 and V_1 are reference values of the radial velocity, density and azimuthal velocity, respectively, at the base of the atmosphere and for some appropriate latitudes. Also, $v_r(\theta)$, $g(\theta)$ and $v_\phi(\theta)$ are for the moment completely arbitrary functions of the co-latitude. We can now define

$$\lambda = \frac{V_1}{V_0} \tag{2.16}$$

as the ratio between the values of the azimuthal velocity and the radial velocity at the base of the atmosphere and

$$\nu = \frac{V_{\rm esc}}{V_0} \tag{2.17}$$

as the ratio between the escape speed and the radial velocity at the base of the atmosphere, where $V_{\rm esc}$ is given by

$$V_{\rm esc} = \sqrt{\frac{2GM}{r_0}}. \tag{2.18}$$

To eliminate the pressure term between the r- and θ- components of the momentum equation, Eqs.(2.9), (2.10), let us differentiate the first one with respect to θ and the second with respect to r, and add them. The resulting expression is

$$\frac{\mathrm{d}}{\mathrm{d}\theta}(gv_r^2)\frac{1}{R^2}\frac{\mathrm{d}Y}{\mathrm{d}R} - \frac{\mathrm{d}}{\mathrm{d}\theta}(gv_\phi^2)\frac{\lambda^2}{YR^5} + \frac{\mathrm{d}g}{\mathrm{d}\theta}\frac{\nu^2}{2YR^4} + gv_\phi^2\cot\theta\frac{\mathrm{d}}{\mathrm{d}R}\left(\frac{\lambda^2}{YR^4}\right) = 0. \tag{2.19}$$

Our aim is to seek separable solutions of this first-order differential equation. In general, in order for this to become an ordinary differential equation involving functions of R alone, the θ-dependence needs to factor out and so the functions of θ that appear in each term need to be proportional to one another. Thus, looking at the second and fourth term, we may first write

$$\frac{\mathrm{d}}{\mathrm{d}\theta}(gv_\phi^2) = 2\epsilon(gv_\phi^2)\cot\theta, \tag{2.20}$$

say, where ϵ is a constant, or equivalently,

$$\frac{\mathrm{d}}{\mathrm{d}\theta}\left(\frac{gv_\phi^2}{\sin^{2\epsilon}\theta}\right) = 0, \tag{2.21}$$

which implies that

$$gv_\phi^2 = \sin^{2\epsilon}\theta. \tag{2.22}$$

Here, we have assumed that the integration constant is one, without loss of generality. Any other value different from one can be incorporated into the radial dependence of ρV_ϕ^2. In what follows all constants of integration will be chosen so that the simplest possible solution is obtained. Considering the third and fourth terms we can write

$$\frac{\mathrm{d}g}{\mathrm{d}\theta} = 2\epsilon\delta gv_\phi^2\cot\theta = 2\epsilon\delta\cos\theta\sin^{2\epsilon-1}\theta, \tag{2.23}$$

say, where δ is a constant. Integrating Eq.(2.23) and substituting into Eq.(2.22), we obtain for the latitudinal dependences of the density and azimuthal velocity

$$g(\theta) = 1 + \delta \sin^{2\epsilon} \theta, \tag{2.24}$$

$$v_\phi(\theta) = \frac{\sin^\epsilon \theta}{\sqrt{1 + \delta \sin^{2\epsilon} \theta}}. \tag{2.25}$$

Finally, comparing the first and last term in Eq.(2.19) we can put

$$\frac{\mathrm{d}}{\mathrm{d}\theta}(g v_r^2) = 2\epsilon\mu g v_\phi^2 \cot\theta = 2\epsilon\mu \cos\theta \sin^{2\epsilon-1}\theta, \tag{2.26}$$

say, where μ is the third arbitrary constant. This gives, after integration, the following latitudinal variation of the radial velocity

$$v_r(\theta) = \sqrt{\frac{1 + \mu \sin^{2\epsilon} \theta}{1 + \delta \sin^{2\epsilon} \theta}}. \tag{2.27}$$

Note that there is another class of solutions of Eq.(2.19). If we put $\epsilon = 0$ and $\epsilon\delta \neq 0$, Eq.(2.23) yields, after integration,

$$g(\theta) = 2\epsilon\delta \log(\xi \sin\theta), \tag{2.28}$$

$$v_\phi(\theta) = \frac{1}{\sqrt{2\epsilon\delta \log(\xi \sin\theta)}}, \tag{2.29}$$

valid for $\epsilon\delta > 0$. However such a solution is unphysical due to the presence of the singularity at $\theta = 0$ (the pole). A similar class of solutions occurs for $\epsilon = 0$ and $\epsilon\mu > 0$.

We will thus take Eqs.(2.24), (2.25), (2.27) as the most general solution of Eq.(2.19). From Eq.(2.24) it is obvious that this is only valid for $\epsilon \geq 0$. Otherwise, there is a singularity at $\theta = 0$. The case $\epsilon = 0$ corresponds to a density distribution which does not vary with latitude. Also, from Eqs.(2.25) and (2.27) the two other constants should satisfy $\delta \geq -1$ and $\mu \geq -1$.

So far this derivation has introduced three parameters which control the latitudinal behaviour of the various hydrodynamic quantities. The parameter δ can be understood as the ratio between density at the equator to density at the polar axis, for the same distance. In fact,

$$\delta = \frac{\rho(\overline{r}, \pi/2)}{\rho(\overline{r}, 0)} - 1 \tag{2.30}$$

for any value of $\overline{r}$. The higher is δ the more the density distribution deviates from spherical symmetry. This value is being assumed constant throughout the whole atmosphere. Note in passing that observations of a polar coronal hole between 2-5$R_\odot$ reported by Munro and Jackson (1977) yield values of density which follow Eq. (2.24) with $\epsilon = 1$ and $\delta = 2.14$.

In this solution, the special case $\epsilon = 1$ and $\mu = -1$ corresponds to the latitudinal dependences adopted in a similar model by TT90. However, their approach was to specify *a priori* the form of $v_r(\theta)$, $g(\theta)$ and $v_\phi(\theta)$ so that (i) the degree of collimation of the outflow is controlled by a

single parameter, δ, in a way that reproduces astrophysical outflows from, almost spherical winds to highly collimated jets, (ii) the density increases towards the equator so as to simulate the presence of an equatorial disk of material, (iii) the azimuthal velocity is zero on the flow axis and (iv) the variables separate in the momentum equation. In the approach presented here, we have deduced the most general separable solution of the equations of conservation of mass and momentum. This gives three parameters, δ, ϵ and μ, the first of which was already present in the previous study, while the latter two are new. We will investigate their influence on the form of the solutions in the following sections.

We should note at this point one crucial difference between this model and the TT90 one. In this treatment the radial velocity does not become zero at the equator, unless $\mu = -1$. In their model this always happens, since it was assumed $v_r \propto \cos\theta$. In the two cases there is an outflow in both the northern and southern hemispheres. The subtle difference is due to the fact that such a solution comes directly from the equations in the present treatment, whereas in TT90 the sign of $\mathbf{V}$ has to be reversed for $\theta > \pi/2$, which is possible since the set of Eqs.(2.1), (2.4) is invariant under the transformation $\mathbf{V} \rightarrow -\mathbf{V}$ (see also Low and Tsinganos (1986) and Tsinganos and Low (1989)).

At this stage we still have to deduce the form of the pressure $p(R,\theta)$ and heating rate $\sigma(R,\theta)$, together with an equation for $Y(R)$. Substituting Eqs.(2.13)-(2.15), with the angular dependences as given by Eqs.(2.24), (2.25) and (2.27), into the r- and θ- components of the momentum equation, we find that for the variables to separate we must have

$$Q(R,\theta) = Q_0(R) + Q_1(R)\sin^{2\epsilon}\theta, \tag{2.31}$$

where $Q(R,\theta)$ is the dimensionless pressure defined by

$$Q(R,\theta) = 2p(R,\theta)/\rho_0 V_0^2. \tag{2.32}$$

Also, $Q_0(R)$ and $Q_1(R)$ are given by

$$Q_1(R) = \frac{\lambda^2}{\epsilon Y R^4}, \tag{2.33}$$

$$\frac{\mathrm{d}Q_1}{\mathrm{d}R} = -\frac{2\mu}{R^2}\frac{\mathrm{d}Y}{\mathrm{d}R} + \frac{2\lambda^2}{YR^5} - \frac{\delta\nu^2}{YR^4}, \tag{2.34}$$

$$\frac{\mathrm{d}Q_0}{\mathrm{d}R} = -\frac{\nu^2}{YR^4} - \frac{2}{R^2}\frac{\mathrm{d}Y}{\mathrm{d}R}. \tag{2.35}$$

The function $Q_0(R)$ represents the spherically symmetric part of the pressure and coincides with its value at the polar axis, while $Q_1(R)$ includes the anisotropy effects. Note also that Eq.(2.33)

is only valid for $\epsilon \neq 0$. Since this parameter was already constrained to non-negative values to prevent a singularity at the pole, we will take $\epsilon > 0$ for the remaining of this chapter.

Similarly, to obtain a separable solution from the heat equation, Eq.(2.12), we must have

$$\sigma(R,\theta) = \left[\sigma_0(R) + \sigma_1(R)\sin^{2\epsilon}\theta\right]\frac{(1+\mu\sin^{2\epsilon}\theta)^{1/2}}{(1+\delta\sin^{2\epsilon}\theta)^{3/2}}, \tag{2.36}$$

where $\sigma_0(R)$ and $\sigma_1(R)$ represent, respectively, the isotropic and anisotropic parts of the heating rate. This gives

$$\sigma_0(R) = \frac{V_0^3 Y}{2r_0(\Gamma-1)}\left[\frac{\mathrm{d}Q_0}{\mathrm{d}R}YR^2 + \Gamma Q_0\frac{\mathrm{d}Y}{\mathrm{d}R}R^2 + 2\Gamma Q_0 YR\right], \tag{2.37}$$

$$\sigma_1(R) = \frac{V_0^3 Y}{2r_0(\Gamma-1)}\left[\frac{\mathrm{d}Q_1}{\mathrm{d}R}YR^2 + \Gamma Q_1\frac{\mathrm{d}Y}{\mathrm{d}R}R^2 + 2\Gamma Q_1 YR\right]. \tag{2.38}$$

We still have to deduce an equation for the radial dependence of the radial velocity, $Y(R)$. Differentiating both sides of Eq.(2.33) and comparing with Eq.(2.34) we find the following nonlinear first-order differential equation for $Y(R)$

$$\frac{\mathrm{d}Y}{\mathrm{d}R} = \frac{Y}{R}\left[\frac{\epsilon\delta\nu^2 R - 2(\epsilon+2)\lambda^2}{\lambda^2 - 2\mu\epsilon Y^2R^2}\right]. \tag{2.39}$$

If $\mu > 0$, this expression has a critical point at the values (R_0, Y_0), say, of (R, Y) given by

$$R_0 = \frac{2(2+\epsilon)\lambda^2}{\epsilon\delta\nu^2}, \quad Y_0 = \sqrt{\frac{\epsilon}{2\mu}}\left(\frac{\delta\nu^2}{2(2+\epsilon)\lambda}\right). \tag{2.40}$$

To classify the nature of this critical point, let us make a first-order expansion around (R_0, Y_0) by writing

$$R = R_0(1+\eta), \quad Y = Y_0(1+\tau) \tag{2.41}$$

where η, τ represent small increments such that $\eta, \tau \ll 1$. In the set of coordinates (η, τ) this critical point corresponds to $(0,0)$. Substituting Eqs.(2.41) into Eq.(2.39), using Eq.(2.40) and keeping the analysis linear (*i.e.* ignoring terms of second order or higher in η, τ), we arrive at

$$\frac{\mathrm{d}\tau}{\mathrm{d}\eta} = -A\left(\frac{\eta}{\eta+\tau}\right), \tag{2.42}$$

where

$$A = \frac{\epsilon^2\delta^2\nu^4}{4\lambda^3(2+\epsilon)\sqrt{2\mu\epsilon}}. \tag{2.43}$$

We can now invoke the linear result of Appendix A to classify the critical point $(\eta, \tau) = (0,0)$. In this case, comparing Eq.(2.42) with Eq.(A.1) we find $a = b = 1$, $c = -A$, $e = 0$, and thus

$(a + e) = 1$. The determinant Δ given by Eq.(A.7) corresponds to $\Delta = 1 - 4A$. For most applications of interest, $\delta^2\nu^4 \gg \lambda^3$, so that Eq.(2.43) implies that $1 - 4A < 0$. Under these conditions, Eq.(A.6) gives m_1, m_2 as complex conjugates and we fall into Case 4 of Table A.1. The critical point is a spiral point of the linear system, Eq.(2.42). This is also the case for the nonlinear system, Eq.(2.39), if we are close enough to the critical point that terms of second order or higher in η, τ are negligible when compared with terms of first order. Such a point is however unphysical, since it does not link a flow coming from the surface of the star and going to large distances. To obtain physically acceptable solutions we therefore need $\mu \leq 0$, for which Eq.(2.39) has no singularity.

The case $\mu = 0$ can be integrated analytically to give

$$Y \propto e^{mR} R^{-n}, \tag{2.44}$$

where $m = \epsilon\delta\nu^2/\lambda^2$ and $n = 2(\epsilon + 2)$. Since $m, n > 0$, the increase with R of the exponential is faster than the decrease of the power term and the solution diverges for large values of R. We shall therefore also exclude this case.

Going back to Eq.(2.39), the radial velocity in the region $R > 1$ is monotonically accelerating only if $\delta > \delta_0$, say, where

$$\frac{1}{\delta_0} = \frac{\epsilon\nu^2}{2(\epsilon + 2)} \left(\frac{V_r(r_0, 0)}{V_\phi(r_0, \pi/2)} \right)^2 - 1. \tag{2.45}$$

For a solar-like central object ($M = M_\odot$, $R = R_\odot$), using for the base of the atmosphere a polar radial velocity $V_r(r_0, 0) = 5$ km s^{-1} (or $\nu = 120$) and an equatorial azimuthal velocity $V_\phi(r_0, \pi/2) = 2.5$ km s^{-1}, this constraint gives $\delta > 10^{-4}$. Analogously, for a star of $12M_\odot$ and $6R_\odot$ (e.g. B star), using the values $V_r(r_0, 0) = 5$ km s^{-1} (or $\nu = 170$) and $V_\phi(r_0, \pi/2) = 100$ km s^{-1}, and still assuming $\epsilon = 1$, the same constraint implies that $\delta > 10^{-1}$.

For $\delta < \delta_0$ the radial velocity has a minimum at R_0 and is monotonically accelerating for $R > R_0$. This includes the case $\delta = 0$ (spherical symmetric density distribution) and the case $\delta < 0$, in which the density is higher at the polar regions than at the equatorial ones.

In summary, the parameter space of interest, for which the wind is accelerating from the base of the atmosphere, there are no unphysical critical points in the radial velocity profile and $Y(R)$ does not diverge at large R, is thus

- $\epsilon > 0$,
- $\delta > \delta_0$,
- $-1 \leq \mu < 0$.

The final solution is

$$V_r(R,\theta) = V_0 Y(R)\sqrt{\frac{1+\mu\sin^{2\epsilon}\theta}{1+\delta\sin^{2\epsilon}\theta}}, \tag{2.46}$$

$$V_\phi(R,\theta) = \frac{V_1}{R}\frac{\sin^{\epsilon}\theta}{\sqrt{1+\delta\sin^{2\epsilon}\theta}}, \tag{2.47}$$

$$\rho(R,\theta) = \frac{\rho_0}{Y R^2}(1+\delta\sin^{2\epsilon}\theta), \tag{2.48}$$

with the function $Y(R)$ defined by Eq. (2.39), while the pressure is given by Eqs.(2.31), (2.33), (2.35) and the heating rate $\sigma(R,\theta)$ is given by Eqs. (2.36) – (2.38). Also, V_0, V_1, ρ_0 can be written in terms of reference values at the base of the atmosphere, using Eqs.(2.46)-(2.48).

$$V_0 = V_r(R=1,\theta=0°), \tag{2.49}$$

$$V_1 = \sqrt{1+\delta}V_\phi(R=1,\theta=90°), \tag{2.50}$$

$$\rho_0 = \rho(R=1,\theta=0°). \tag{2.51}$$

Since pressure and density do not follow a polytropic law $p \propto \rho^\gamma$, with γ constant (but instead the polytropic index is given by Eq. (2.5)), the usual sound speed $V_s^2 = \partial p/\partial\rho$ is ill-defined. We can however define an effective sound speed corresponding to a constant $\gamma = \Gamma$, where Γ is the ratio of specific heats, as given by Eq. (1.13) (for a monatomic gas, $\Gamma = 5/3$)

$$V_s^2 = \Gamma\frac{p}{\rho} = \frac{\Gamma k_B}{m}T, \tag{2.52}$$

the last equality arising from the ideal gas law, Eq.(1.21). The Mach number M corresponds to

$$M = \frac{V_r}{V_s}. \tag{2.53}$$

2.4 Parametric Study of the Solution

2.4.1 Latitudinal Variations

We can first see the influence of the different parameters on the form of the solution by taking a closer a look at the angular dependences. Starting with the radial velocity, Fig. 2.1 shows that v_r never increases from pole to equator. In fact from the relation

$$\frac{v_r(\pi/2)}{v_r(0)} = \sqrt{\frac{1+\mu}{1+\delta}}, \tag{2.54}$$

we always have $v_r(0) > v_r(\pi/2)$ for any values of δ and μ, providing the wind is accelerating ($\delta > \delta_0$). In other words, an accelerated wind emerging from the less dense polar regions, with respect to the denser equatorial ones, is always collimated around the polar axis with a higher velocity at the poles than near the equator. The cone around the polar axis where the velocity attains high values is narrower for large values of δ and smaller values of ϵ. In particular, and from Eq. (2.27), for $\epsilon = 1$, $\mu = -1$ and $\delta = 10$, the radial velocity for a given radius has decreased to 10% of its value at the pole for latitudes of 18°, while for $\delta = 10^3$ this occurs for latitudes of 73°. In other words the flow is more collimated around the pole for higher values of δ. Note that this notion of collimation should not be confused with cylindrical geometry for the streamlines. In this helicoidal model, where the streamlines are straight lines in the meridional plane, we shall refer to velocity collimation around the polar axis in the broader sense of high speeds near the poles and lower values near the equator. Increasing ϵ produces a sharper drop closer to the equator. Fig. 2.1(c) shows that the radial velocity is zero at the equator only for $\mu = -1$, where the drop from pole to equator is largest. In some sense, δ and ϵ control the collimation of the outflow whereas μ is associated to the value of V_r at the equator.

The latitudinal behaviour of the azimuthal velocity is such that increasing δ results in lower values of v_ϕ throughout with a more isotropic distribution in latitude, as can be seen in Fig. 2.2(a). With the value of δ fixed, rotation at the equator is the same for all values of ϵ and decreases sharply towards the poles for high ϵ (Fig. 2.2(b)).

Figure 2.3 shows that the distribution of density has a peak at the equator for $\delta > 0$. This maximum increases with the increase of δ. Fixing this parameter, the thickness of the region around the equator, for which there is a higher density of material, is smaller for larger ϵ. This can be used to model a disk of high mass density.

In most cases, as we shall see later, the anisotropic part of the heating rate, $\sigma_1(R)$, is negligible when compared with the spherically symmetric part, $\sigma_0(R)$. Looking back at Eq. (2.36) we can thus write the heating rate as $\sigma(R,\theta) \simeq \sigma_0(R)s(\theta)$, where

$$s(\theta) = \frac{(1+\mu\sin^{2\epsilon}\theta)^{1/2}}{(1+\delta\sin^{2\epsilon}\theta)^{3/2}}. \tag{2.55}$$

In these circumstances the heating rate varies with latitude very similarly to the radial velocity

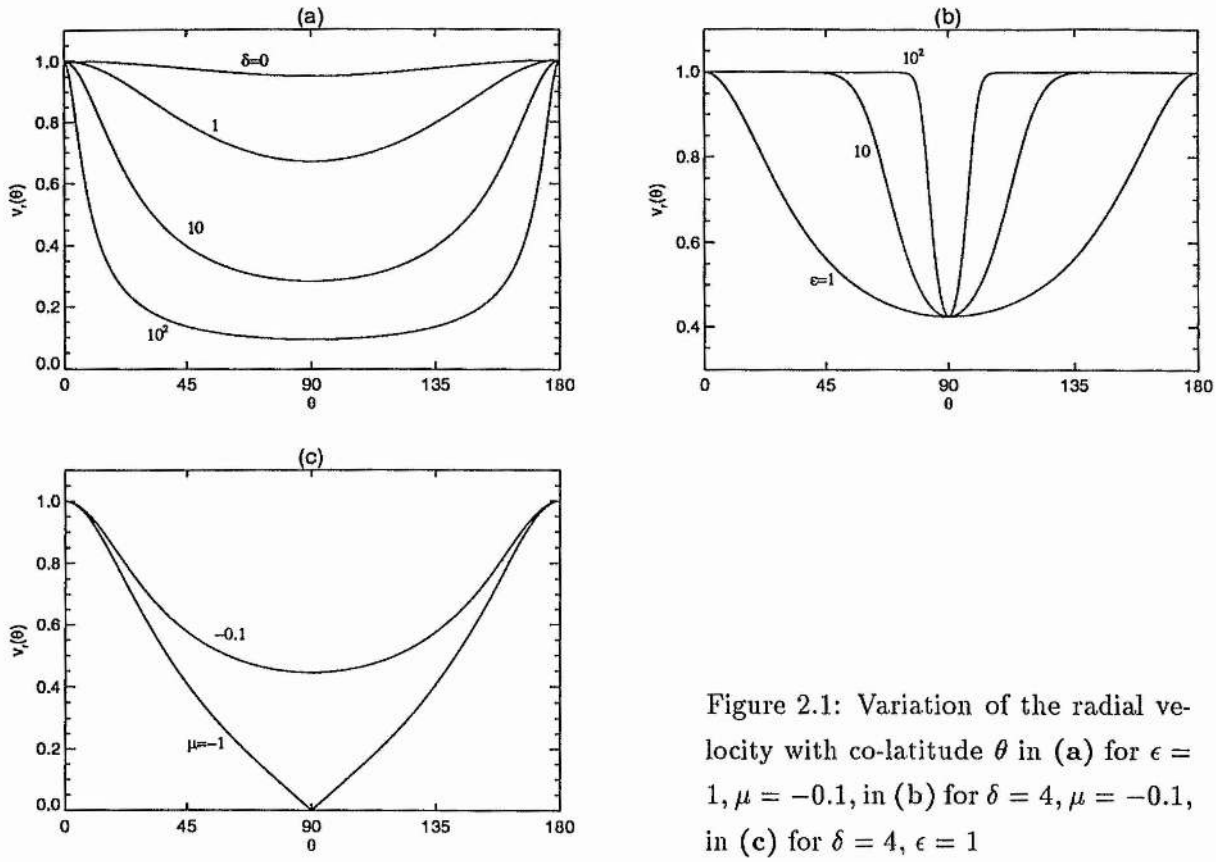

Figure 2.1: Variation of the radial velocity with co-latitude θ in **(a)** for $\epsilon = 1, \mu = -0.1$, in (b) for $\delta = 4, \mu = -0.1$, in **(c)** for $\delta = 4, \epsilon = 1$

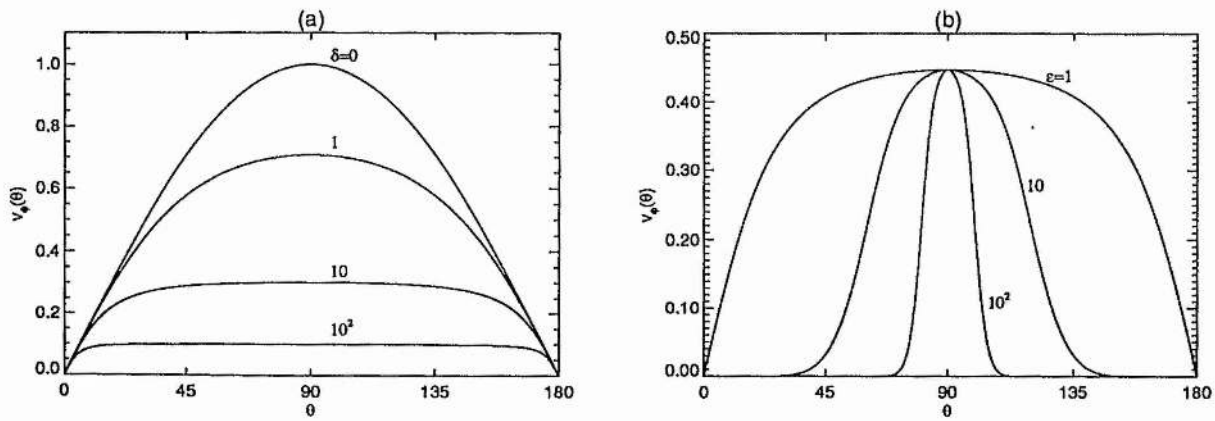

Figure 2.2: Variation of the azimuthal velocity with co-latitude θ in **(a)** for $\epsilon = 1$, in **(b)** for δ=4

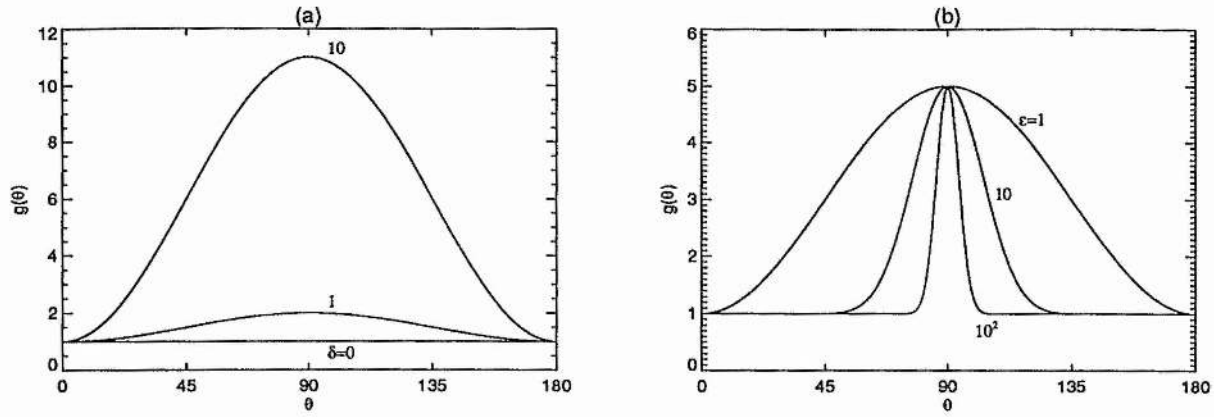

Figure 2.3: Variation of the density with co-latitude θ in **(a)** for $\epsilon = 1$, $\mu = -1$, in **(b)** for $\delta = 4$, $\mu = -1$

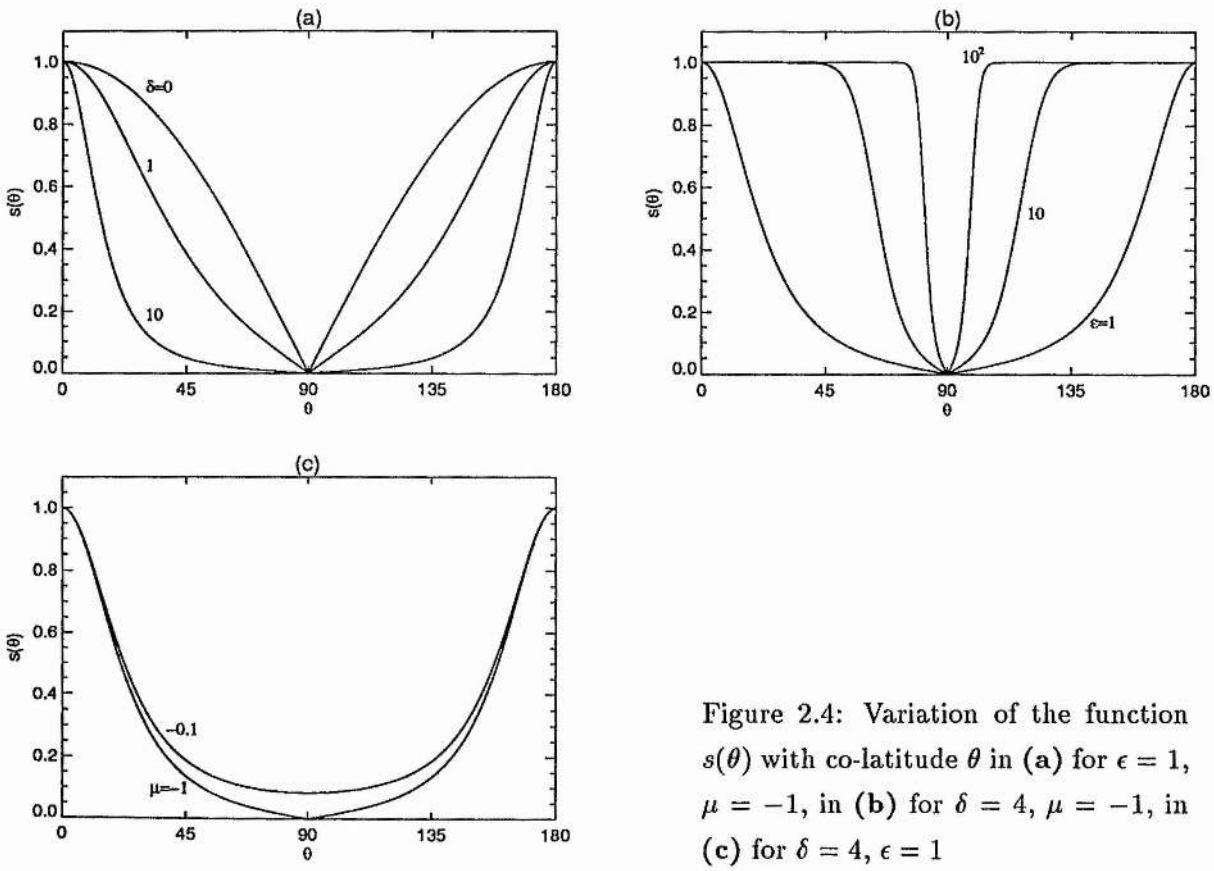

Figure 2.4: Variation of the function $s(\theta)$ with co-latitude θ in **(a)** for $\epsilon = 1$, $\mu = -1$, in **(b)** for $\delta = 4$, $\mu = -1$, in **(c)** for $\delta = 4$, $\epsilon = 1$

(Fig. 2.4). In particular, σ is more concentrated towards the pole for high values of δ and small values of ϵ. If we include σ_1, the general qualitative behaviour is similar.

2.4.2 Asymptotic Analysis

After discussing the forms of the various latitudinal dependences, we now proceed to investigate the variation with radial distance of the different physical quantities.

Equations (2.35) and (2.39) constitute a system of first-order differential equations for $Q_0(R)$ and $Y(R)$, which can be integrated numerically. For that purpose we need one boundary condition for each of these two variables. For the function $Y(R)$, which represents the dimensionless radial velocity at the pole, we will adopt $Y(R=1)=1$. This corresponds to defining the constant V_0 as $V_0 = V_r(R=1, \theta=0)$, from Eq. (2.46). The boundary condition on the dimensionless pressure at the pole, $Q_0(R)$, can be obtained after some analysis on the asymptotics for large R. In this limit, and retaining only higher order terms, Eq.(2.39) can be written as

$$\frac{\mathrm{d}Y}{\mathrm{d}R} \simeq -\left(\frac{\delta\nu^2}{2\mu}\right)\frac{1}{YR^2}, \tag{2.56}$$

where we have neglected terms of order lower than $O(R^{-3})$. This can be easily integrated to give

$$Y(R) \simeq \sqrt{1+\frac{\delta\nu^2}{|\mu|}\left(1-\frac{1}{R}\right)}, \tag{2.57}$$

valid for large values of R. Note that coincidentally, the above expression is equivalent to the solution of the general equation, Eq.(2.39), for $\lambda = 0$. In other words, the asymptotic value of Y equals its value in the case of no rotation. When $R \to \infty$, Eq. (2.57) reduces to

$$Y_\infty = \sqrt{1+\frac{\delta\nu^2}{|\mu|}}. \tag{2.58}$$

To find the asymptotic behaviour of $Q_0(R)$ for large R we can substitute $\mathrm{d}Y/dR$ given by Eq. (2.56) on the right-hand side of Eq. (2.35) to obtain

$$\frac{\mathrm{d}Q_0}{\mathrm{d}R} \simeq -\nu^2\left(1-\frac{\delta}{\mu}\right)\frac{1}{YR^4}, \tag{2.59}$$

which is always negative. For large R and to zeroth-order, $Y \simeq Y_\infty$. Thus if we substitute this in the above expression and integrate, we find the following asymptotic form for large R

$$Q_0(R) \simeq \frac{\nu^2}{3Y_\infty}\left(1+\frac{\delta}{|\mu|}\right)\frac{1}{R^3}. \tag{2.60}$$

Here we have neglected terms with order lower than R^{-3} and assumed that Q_0 drops to zero at

infinity. In fact, for the pressure to go to zero at infinity, for any value of θ, Eq. (2.31) implies that Q_0 must vanish there. This is a normal requirement in stellar wind models and is related to the possibility of merging such solutions into the low pressure of the interstellar background (Hundhausen 1972).

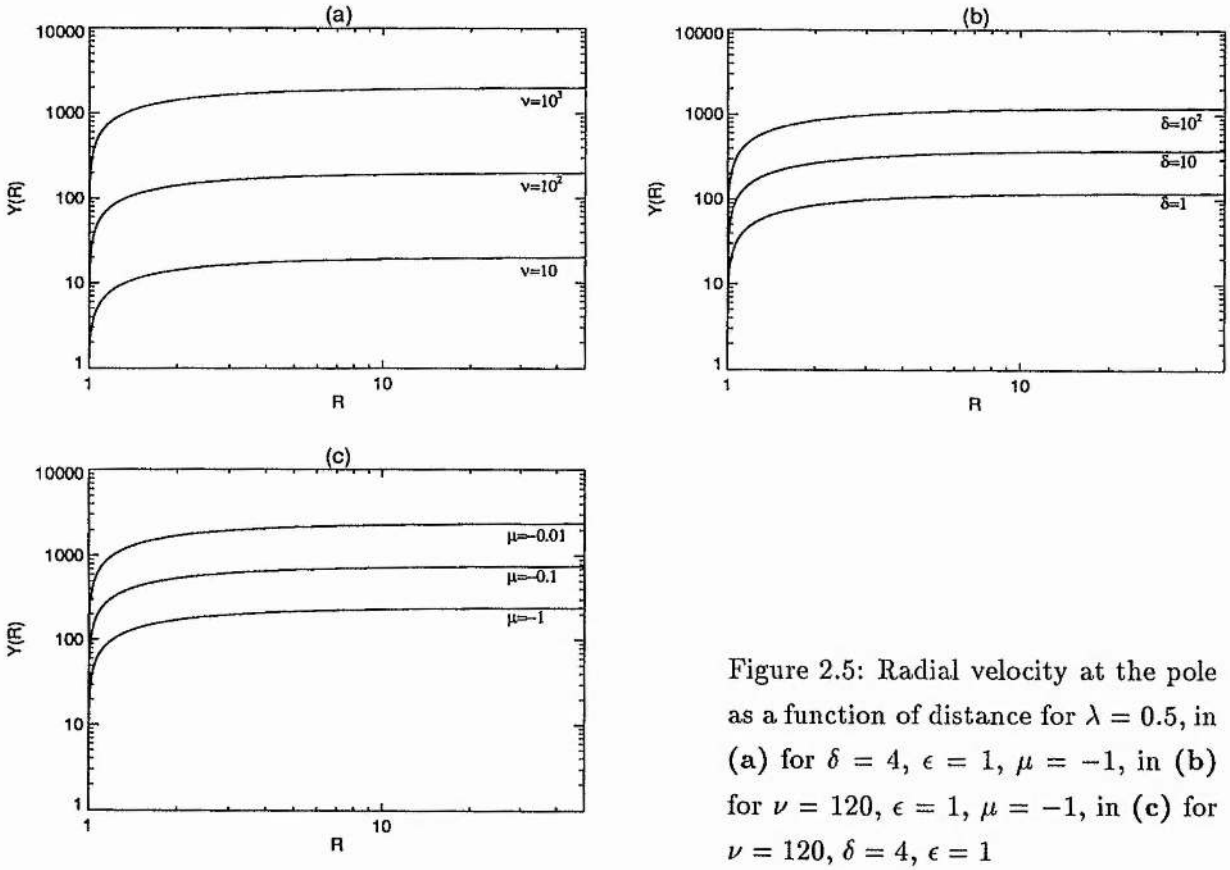

Figure 2.5: Radial velocity at the pole as a function of distance for $\lambda = 0.5$, in **(a)** for $\delta = 4$, $\epsilon = 1$, $\mu = -1$, in **(b)** for $\nu = 120$, $\epsilon = 1$, $\mu = -1$, in **(c)** for $\nu = 120$, $\delta = 4$, $\epsilon = 1$

Equation (2.60) can now be used as a boundary condition for $Q_0(R)$, as follows. Starting with $Y(R = 1) = 1$, we integrate Eq.(2.39) until $R = R_f$ (typically, $R_f \sim 10^8$). At this point $Y_f \equiv Y(R_f) \simeq Y_\infty$, and thus we can use Eq. (2.60) with $R = R_f$ to obtain $Q_0^f = Q_0(R_f)$. This will be used as the boundary condition for Q_0. We can now integrate Eqs. (2.35) and (2.39) backwards, from $R = R_f$ to $R = 1$, with boundary conditions $Q_0 = Q_0^f$ and $Y = Y_f$, respectively. The value $Y = 1$ should be reproduced again at $R = 1$. Simultaneously, all remaining radial functions can be calculated. Thus, $Q_1(R)$ is given by Eq.(2.33), while $\sigma_0(R)$ and $\sigma_1(R)$ are given by Eqs. (2.37) and (2.38), respectively.

A simple Fortran code making use of subroutine D02BAF of the NAG library was developed. This routine implements a Merson form of the Runge-Kutta method to integrate a system of first-order ordinary differential equations (Hall and Watt 1976).

The form of $Y(R)$ is shown in Fig. 2.5. There is a high acceleration close to the base of the

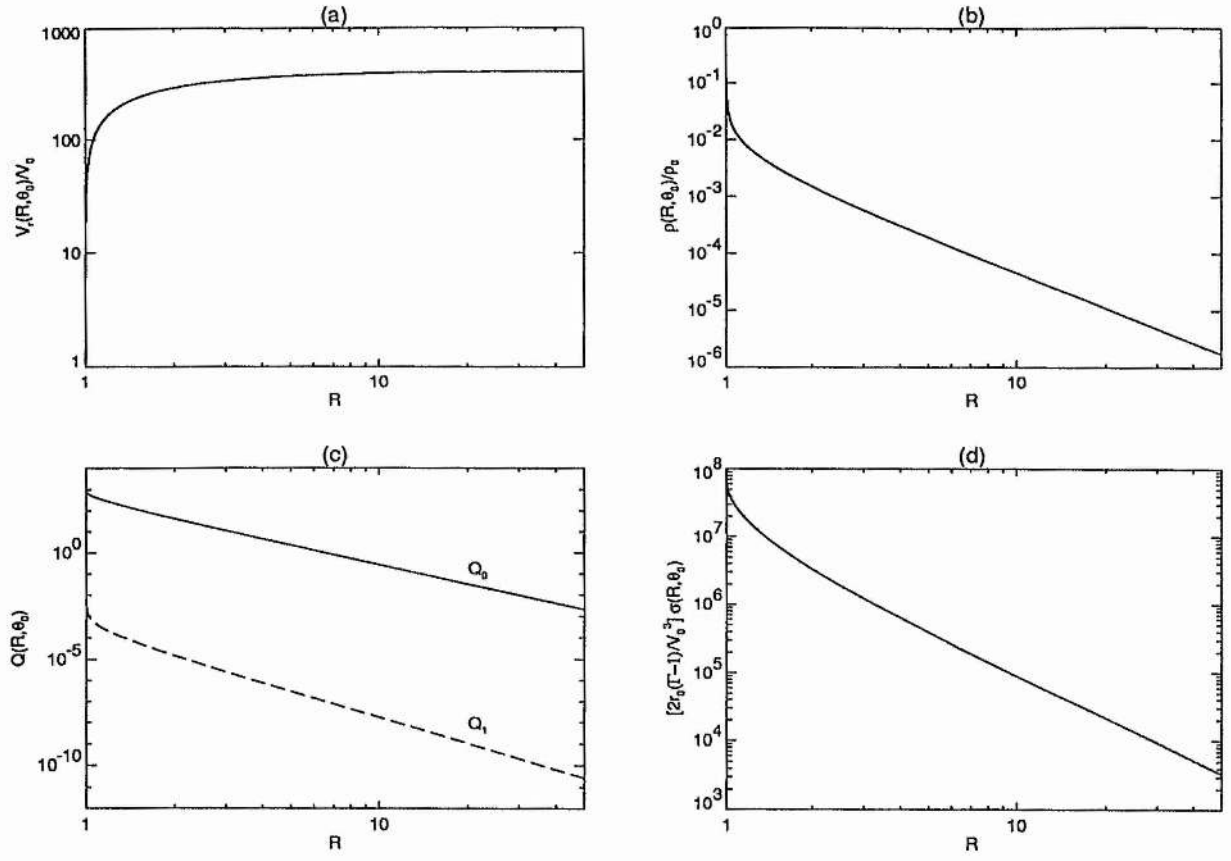

Figure 2.6: Radial velocity, density, pressure and heating rate as functions of distance for $\lambda = 0.5$, $\nu = 120$, $\delta = 4$, $\epsilon = 2$, $\mu = -0.1$ for a co-latitude of $\theta_0 = 60°$

atmosphere and Y reaches very rapidly its asymptotic value Y_∞. In fact,

$$\left(\frac{\mathrm{d}Y}{\mathrm{d}R}\right)_{R=1} = \frac{\epsilon\delta\nu^2 - 2(\epsilon+2)\lambda^2}{\lambda^2 - 2\mu\epsilon} \tag{2.61}$$

which is positive if $\delta > \delta_0$ — see Eq. (2.45). The initial acceleration can be very high for sufficiently high values of ν, so that $\delta\nu^2 \gg \lambda^2$. Note that both this initial acceleration and the asymptotic value of Y given by Eq. (2.58) depend on $\delta\nu^2$ but not on δ or ν separately.

Notice the absence of a critical point in the radial velocity profile, which is related to our inability to define the sound speed for this non-polytropic atmosphere, as discussed in Sect. 2.3. This is in sharp contrast with Parker's polytropic model of the solar wind Parker (1958a, 1963) , where there is a critical point in the velocity profile corresponding to the point where the outflow speed equals the sound speed.

We should stress at this point that under the assumption of separability, the variation of the

different variables with the parameters of the problem is a combination of the variation of both their latitudinal parts and their radial dependences. For instance, the radial velocity at large distances is given by

$$V_r^{\infty}(\theta) \equiv V_r(R \to \infty, \theta) \simeq V_0 \sqrt{1 + \frac{\delta \nu^2}{|\mu|}} \sqrt{\frac{1 - |\mu| \sin^{2\epsilon} \theta}{1 + \delta \sin^{2\epsilon} \theta}}. \tag{2.62}$$

This means that the variation of V_r^{∞} with ϵ comes only from its latitudinal dependence as given by Eq. (2.62). In fact this asymptotic value increases with ϵ for $0° < \theta < 90°$ (see Fig. 2.1(b)) even though Y_{∞} only depends on δ, ν and μ. Since ν measures the strength of the gravitational force, which is spherically symmetric, we always have $V_r^{\infty} \propto \nu$, independently of latitude. This relation can be understood as follows. The greater the escape speed, the higher has to be the initial acceleration needed to overcome the gravitational potential and still accelerate the outflow — see Eq. (2.61). This results in higher values of V_r for large distances R.

The density decreases sharply near the base of the atmosphere due to the rapid increase of Y (Fig. 2.6(b)). However, ρ attains its asymptotic decay as $1/R^2$ within a few radii, thus giving for large R

$$\rho^{\infty}(\theta) \simeq \sqrt{\frac{|\mu|}{|\mu| + \delta \nu^2}} \frac{(1 + \delta \sin^{2\epsilon} \theta)}{R^2}. \tag{2.63}$$

This shows that asymptotically the density, while decreasing with ϵ and increasing with $|\mu|$ (*i.e.* opposite to the radial velocity), increases with δ similarly to the radial velocity. If the pressure and density were to satisfy a polytropic relationship $p \propto \rho^{\gamma}$ then the larger velocities, found by increasing δ, would be associated with a faster drop of the density for larger δ. Here exactly the opposite holds because we do not use the polytropic relation, and thus no straightforward relation between pressure and density.

As for the pressure, close to the star the spherically symmetric part , Q_0, decays very rapidly with distance, since Y is increasing sharply and thus the contribution of the second term on the right-hand side of Eq.(2.35) is dominant. Further out Q_0 goes as $1/R^3$ — see Eq.(2.60). The anisotropic term, $Q_1(R)$, decays asymptotically as $1/R^4$, as given by Eq.(2.33), with $Y = Y_{\infty}$. Even though at the base $Q_1(R = 1) = \lambda^2/\epsilon$ can be larger than $Q_0(R = 1)$, for some choice of parameters, after a certain value of R, Q_0 takes over Q_1. In other words, conservation of momentum implies that, at least for large distances, most of the contribution to the total pressure comes from the spherically symmetric terms, namely the gravitational force term and the spherically symmetric part of the inertial term. This has implications in terms of the acceleration of the outflow. In fact, since the isotropic part of the pressure, Q_0 is much greater than its anisotropic contribution, Q_1, the variation of the pressure with latitude is negligible. Thus there is a strong acceleration of the outflow near polar regions for high values of δ. In fact, at the equator the outward forces acting on the plasma are the pressure and the centrifugal force, while inwardly the plasma only feels the gravitational force. At the pole, and for the same radial

variable	pole	equator
$V_r \propto$	$\sqrt{\frac{\delta\nu^2}{\lvert\mu\rvert}}$	$\nu\sqrt{\left(\frac{\delta}{1+\delta}\right)\left(\frac{1}{\lvert\mu\rvert}-1\right)}$
$\rho R^2 \propto$	$\sqrt{\frac{\lvert\mu\rvert}{\delta\nu^2}}$	$\left(\frac{1+\delta}{\sqrt{\delta}}\right)\frac{\sqrt{\lvert\mu\rvert}}{\nu}$
$pR^3 \propto$	$\sqrt{\frac{\delta\nu^2}{\lvert\mu\rvert}}$	$\sqrt{\frac{\delta\nu^2}{\lvert\mu\rvert}}$
$\sigma R^2 \propto$	$\nu^3\left(\frac{\delta}{\lvert\mu\rvert}\right)^{3/2}$	$\nu^3\left(\frac{\delta}{1+\delta}\right)^{3/2}\left(\frac{1+\lvert\mu\rvert}{\lvert\mu\rvert^3}\right)^{1/2}$

Table 2.1: Influence of the different parameters on the asymptotic values of the hydrodynamic variables

distance, there is no centrifugal force, the pressure remains almost the same but the density is largely decreased, with this drop being greater the higher is the value of δ (see Figure 2.3(a)). Since this decrease more than compensates for the loss of the centrifugal term to accelerate the flow the net result is an outward force responsible for high speeds around the polar axis. We thus have net acceleration of the flow around the polar axis if the density drops faster with latitude than the pressure does (Tsinganos and Vlastou-Tsinganos, 1988; Hu and Low, 1989).

The heating rate is dominated by σ_0 for large distances. In fact, from Eqs. (2.37) and (2.38), we have for large R and considering only higher-order terms

$$\sigma_0(R) \simeq \left(\frac{2\Gamma-3}{\Gamma-1}\right)\frac{Y_\infty \nu^2 V_0^3}{6r_0}\left(1+\frac{\delta}{|\mu|}\right)\frac{1}{R^2}, \tag{2.64}$$

$$\sigma_1(R) \simeq \left(\frac{\Gamma-2}{\Gamma-1}\right)\frac{Y_\infty \lambda^2 V_0^3}{\epsilon r_0}\frac{1}{R^3}. \tag{2.65}$$

For a monatomic gas $\Gamma = 5/3$ and, in this limit of large R, $\sigma_0 > 0$ while $\sigma_1 < 0$. The high concentration of the heating close to the base of the atmosphere and illustrated in Fig.2.6(d) is typical of a hydrodynamically dominated wind whereby dissipation of energy is mainly due to sound waves and occurs within a few radii. The inclusion of a magnetic field and associated Alfvén waves will enable dissipation to occur at large distances from the star and we expect to see a more uniform heating throughout.

The influence of the parameters on the asymptotic values of the hydrodynamic variables is summarized in Table 2.1 Since $|\mu| < 1$ and in most cases $\delta > 1$ and $\nu \gg 1$, we have taken $\delta\nu^2/|\mu| \gg 1$.

2.5 Two-Dimensional Character

In the previous two sections we have discussed separately the radial dependences and the variations in latitude. We have thus gained some insight about the influence of the different parameters of the problem. However, the great strength of this model is its 2D character and this can be seen by visualizing the different physical quantities in the meridional plane. Figures 2.7-2.10 show contour plots of the radial velocity, density, heating rate and effective sound speed. We have chosen to plot the various quantities only in the first quadrant, since they are all axisymmetric and also symmetric around the equator. We have also taken as cartesian coordinates $x = R\sin\theta$ and $y = R\cos\theta$. Our choice of parameters is related to typical stellar objects. The values of $\mu \neq -1$ are taken so as to yield non-zero outflow speeds at the equator.

The first case (Figs. 2.7) corresponds to values characteristic of the Sun, with $V_r(r_0, 0) = 5\text{kms}^{-1}$ and $\delta = 2$, $\epsilon = 1$ as suggested by the density profile of a polar coronal hole (Munro and Jackson 1977). Note that the degree of anisotropy in the radial speed becomes important only for sufficiently high latitudes and distances, while both the heating rate and sound speed (proportional to temperature in the ideal gas approximation) are more isotropic, but still slightly concentrated near the axis. The second object (Fig. 2.8) is a solar-like object ($M = M_\odot$, $R = R_\odot$) but with a much higher density anisotropy, $\delta = 1000$. The parameter ϵ is also larger in this second case, but this does not greatly affect the various quantities, as discussed before. When δ is very large, all quantities are strongly dependent on latitude. Furthermore the initial acceleration near the pole leads to very high speeds at those latitudes, while the heating rate is concentrated near the rotational axis. In any case, the transition from low to high values of δ affects mainly the variables for large latitudes, as opposed to the equator where they remain mostly unchanged.

The influence of μ can be seen if we compare Figs.2.9 and 2.10, which correspond to a star with $M = 12M_\odot$ and $R = 6R_\odot$. It is obvious that the form of the various curves does not change appreciably between these two sets of graphs, while the respective values do. Note in particular, the sharp increase in the heating rate throughout, from $\mu = -0.5$ to $\mu = -0.001$. Thus the parameter μ (when sufficiently close to zero) does not greatly affect the degree of anisotropy. The global solution is quite insensitive to the strength of rotation (at least when $\delta\nu^2 \gg \lambda^2$) as can be seen by comparing Fig.2.7 to Fig.2.9 (see also (Lima and Priest, 1993)).

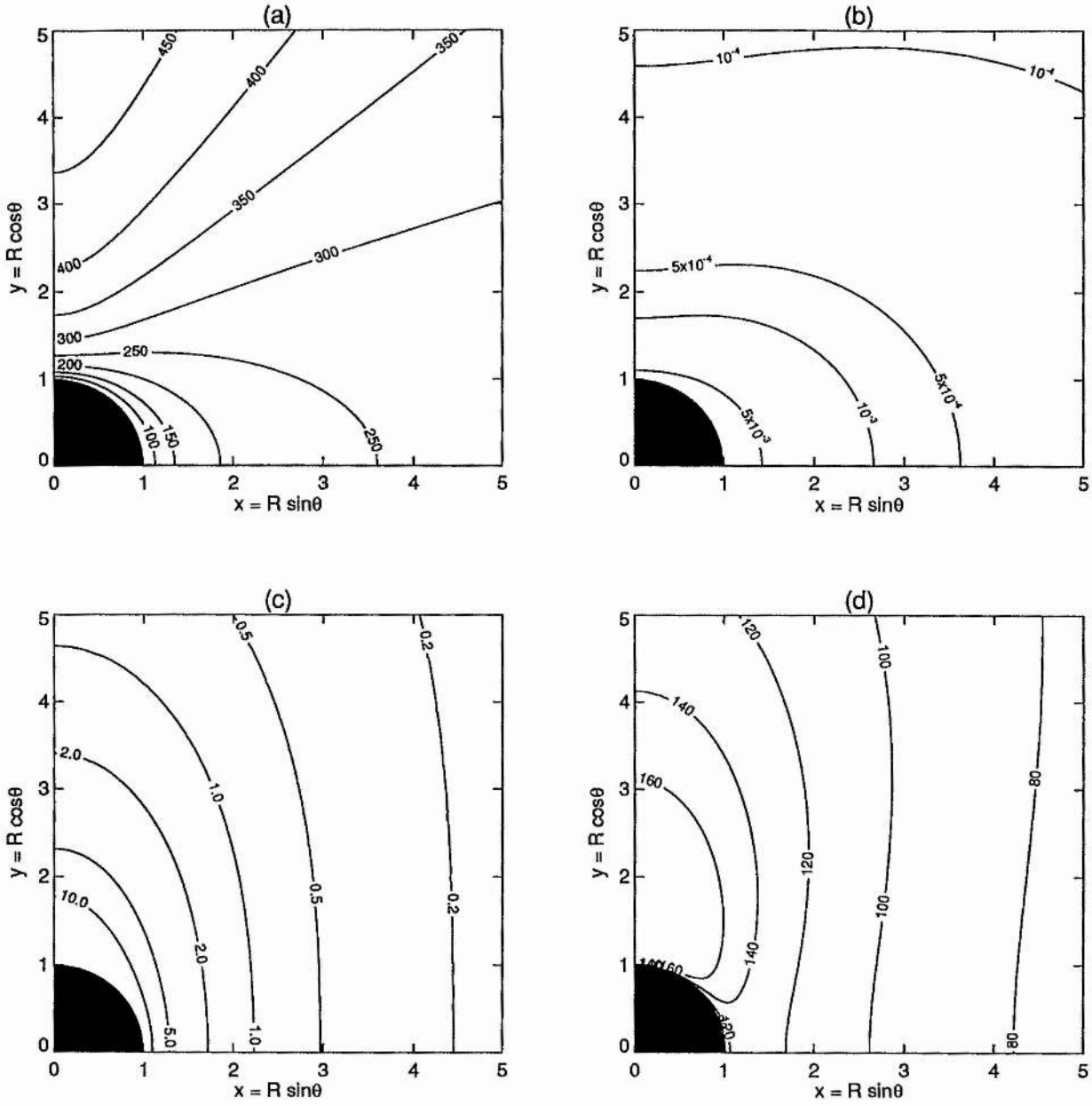

Figure 2.7: Contour plots of the radial velocity $V_r(R,\theta)/V_0$ in **(a)**, density $\rho(R,\theta)/\rho_0$ in **(b)**, heating rate $10^{-6}\sigma(R,\theta)/(V_0^3/2r_0(\Gamma-1))$ in **(c)** and sound speed $V_s(R,\theta)/V_0$ in **(d)** for $\lambda = 0.5$, $\nu = 120$, $\delta = 2$, $\epsilon = 1$, $\mu = -0.1$

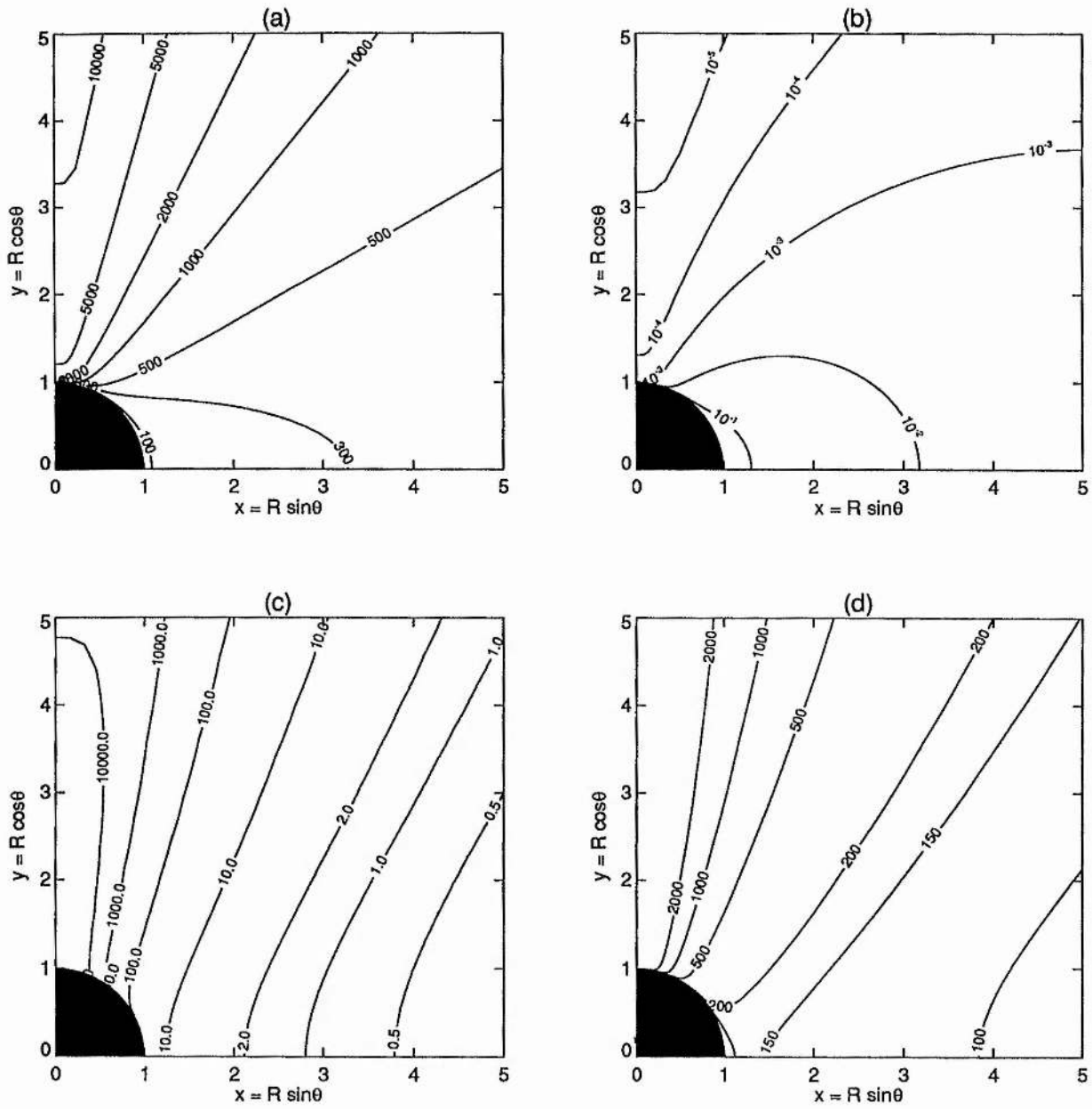

Figure 2.8: Contour plots of the radial velocity $V_r(R,\theta)/V_0$ in **(a)**, density $\rho(R,\theta)/\rho_0$ in **(b)**, heating rate $10^{-6}\sigma(R,\theta)/(V_0^3/2r_0(\Gamma-1))$ in **(c)** and sound speed $V_s(R,\theta)/V_0$ in **(d)** for $\lambda = 0.5$, $\nu = 120$, $\delta = 1000$, $\epsilon = 2$, $\mu = -0.1$

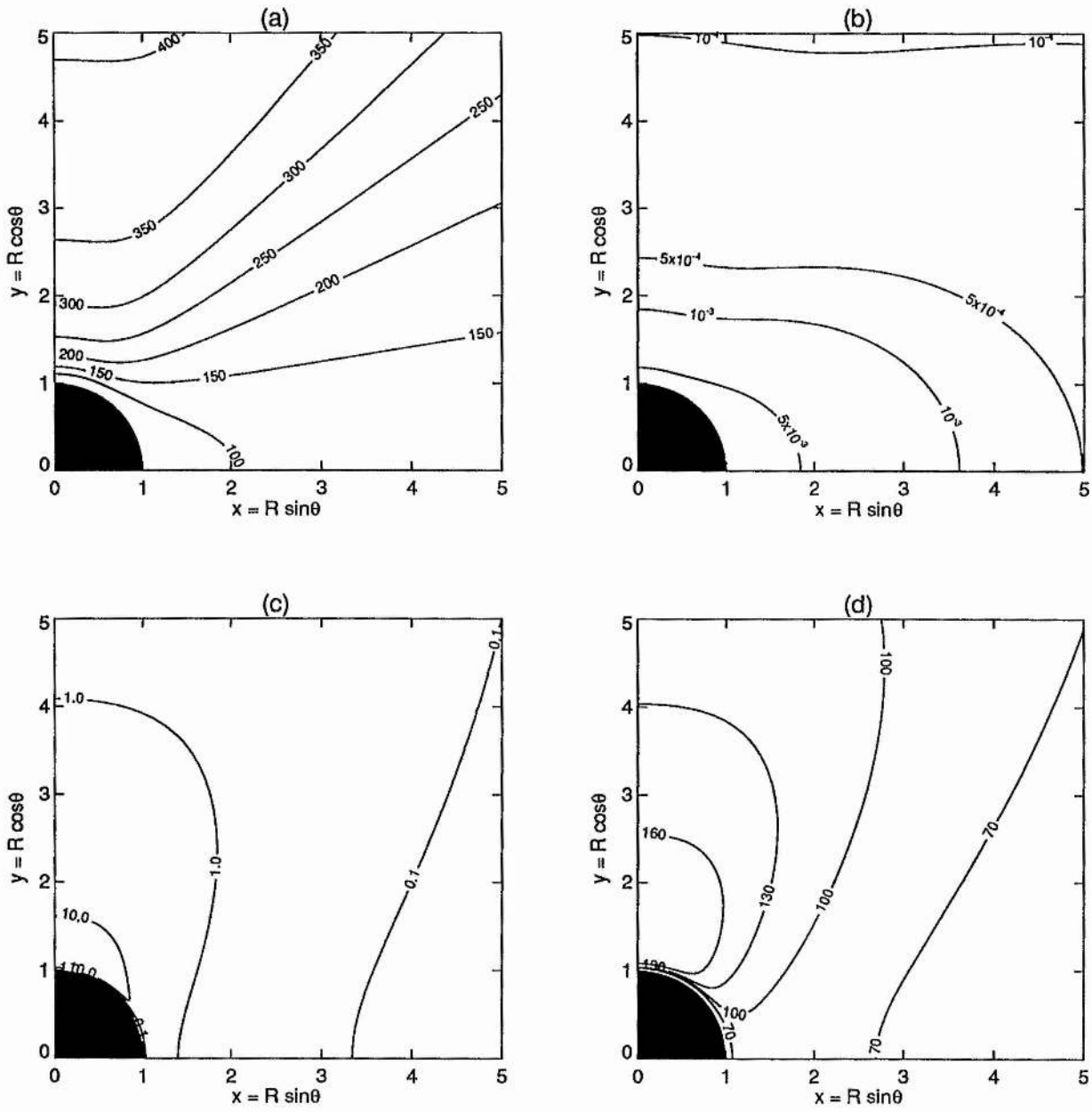

Figure 2.9: Contour plots of the radial velocity $V_r(R,\theta)/V_0$ in **(a)**, density $\rho(R,\theta)/\rho_0$ in **(b)**, heating rate $10^{-6}\sigma(R,\theta)/(V_0^3/2r_0(\Gamma-1))$ in **(c)** and sound speed $V_s(R,\theta)/V_0$ in **(d)** for $\lambda = 50$, $\nu = 170$, $\delta = 4$, $\epsilon = 2$, $\mu = -0.5$

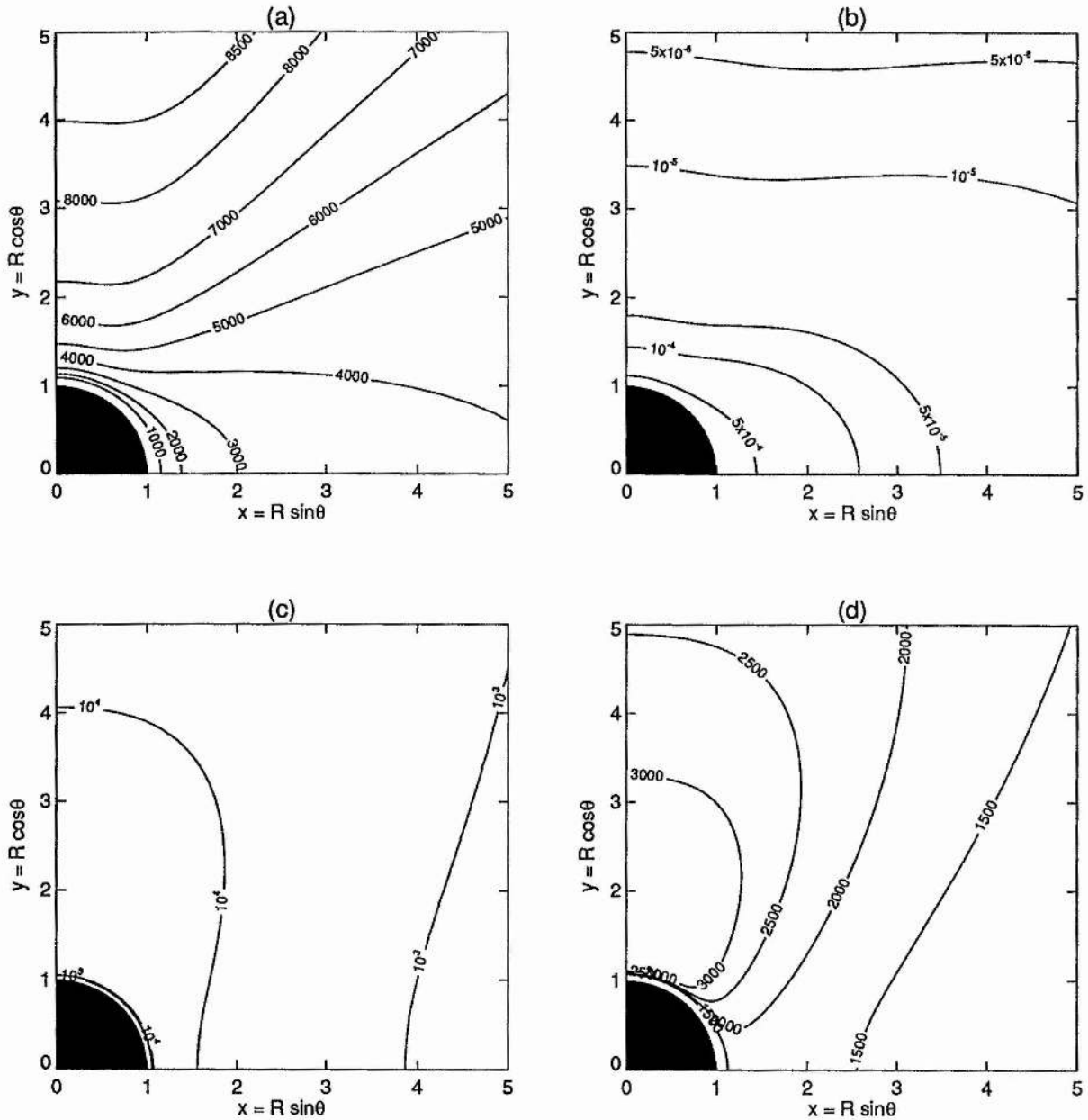

Figure 2.10: Contour plots of the radial velocity $V_r(R,\theta)/V_0$ in **(a)**, density $\rho(R,\theta)/\rho_0$ in **(b)**, heating rate $10^{-6}\sigma(R,\theta)/(V_0^3/2r_0(\Gamma-1))$ in **(c)** and sound speed $V_s(R,\theta)/V_0$ in **(d)** for $\lambda = 50$, $\nu = 170$, $\delta = 4$, $\epsilon = 2$, $\mu = -0.001$

2.6 Conclusions

The approach of looking for general solutions of the steady hydrodynamic equations for an axisymmetric wind originating from a rotating astrophysical object has led us to a new family of solutions. All quantities are dependent on both the radial distance and the co-latitude. The crucial assumptions were the neglect of the meridional velocity and the separation of variables.

A straighforward manipulation involving the $r-$ and $\theta-$components of the momentum balance equation yields a first-order differential equation. Solutions of this equation can be found via separation of variables. Thus the most general latitudinal dependences are obtained. These involve three constants, δ, ϵ and μ, which we will call the anisotropy parameters. Solution for the radial functions is given by a series of differential equations that involve the above three parameters plus two more (λ, ν) which are common to all wind models and associated with the strength of the rotation of the central object and of its gravitational field, respectively. The anisotropy parameters control the degree of collimation of the outflow (in the sense of higher values of radial speed around the poles as compared to the equator) as well as the anisotropy in the distribution of density, pressure and heating rate.

To obtain an accelerated wind throughout the whole of the atmosphere the parameter δ has to be positive. This means that density at the equator always exceeds density at the pole. In fact we can go from an almost spherically symmetric density distribution for low values of this parameter, to a highly anisotropic one for high values of δ. Large values of δ are also responsible for high values of the wind speed at the pole, since in these circumstances the density drops with latitude faster than pressure does.

The parameter μ establishes two qualitatively different solutions. Those with $\mu = -1$ have zero radial velocity at the equator. This favours the presence of a static region around the equator. When $\mu \neq -1$, there is an outflow for $\theta = 90°$. However this can never exceed the polar outflow, since $v_r(0) > v_r(\pi/2)$ for an accelerated wind (see Sect. 2.4.1). What causes this phenomenon is the higher concentration of material near the equator of the star. The flow is hydrodynamically constrained to escape from the polar regions with a higher velocity than from the equatorial ones. Also, very low values of $|\mu|$ can increase substantially both the outflow velocity and the total heating everywhere around the central object. In this sense, and for this limit $|\mu| \ll 1$, the influence of $|\mu|$ is opposite to the effect of gravity and similar to $1/\nu^2$.

Finally, the last of the new parameters, ϵ, is associated with the thickness of the cone around the pole for which the velocity is kept high or, alternatively, the thickness of the region around the equator for which the density is higher than the polar one. Very high values of ϵ result in a sudden drop (or increase) of V_r (or ρ) near the equator (or pole), and an almost uniform distribution throughout the remaining atmosphere. This is relevant for observations suggesting disks of higher density around the equator.

The radial profiles are typical of a hydrodynamic wind, with V_r rapidly attaining a constant asymptotic value, while most of the dissipation of energy occurs within a few radii of the central

object. The absence of a critical point (sonic point) in the velocity profile is related to our inability to define a local sound speed, since we do not assume a polytropic relation between density and pressure. A drawback of this model is the constraint of keeping the streamlines helicoidal. Thus we cannot obtain geometries (*e.g.* cylindrical) that greatly favour strong collimation around the pole, observed as jets in many astrophysical objects.

In summary, this model presents a self-consistent way of finding general separable solutions of the steady axisymmetric hydrodynamic equations and gaining some insight into the physics of the emission of material by a rotating object. The inclusion of the magnetic field and its importance in confining the flow of material will be discussed in the following chapter. Using the same technique described here, we will find solutions of the set of MHD equations.

Chapter 3

Magnetohydrodynamic Model

3.1 Introduction

This chapter will be devoted to the extension of the hydrodynamic model developed in Chapter 2 to include the effect of the magnetic field. We shall look for general solutions of the steady MHD equations for two-dimensional helicoidal outflows. As in the previous case, rather than adopting *a priori* a specific form for the latitudinal variation of the relevant quantities, we will try to keep the analysis as general as possible.

3.2 Solution

3.2.1 Basic Equations and Assumptions

Let us look for solutions of the set of steady MHD equations describing the dynamical interaction of an inviscid, compressible and highly conducting plasma, with an axially symmetric magnetic field created by a central rotating object. These are Maxwell's equation for the divergence of the magnetic field, the induction equation in the limit of large length-scales and equations for conservation of mass, angular momentum and energy. They have been extensively written down by many authors in the context of solar/stellar wind problems (Weber and Davis, 1967; Tsinganos, 1982; Sakurai, 1985; Tsinganos and Trussoni, 1991) and were introduced in Sect.1.3

$$\nabla \cdot \mathbf{B} = 0, \tag{3.1}$$

$$\nabla \times (\mathbf{V} \times \mathbf{B}) = 0, \tag{3.2}$$

$$\nabla \cdot (\rho \mathbf{V}) = 0, \tag{3.3}$$

$$\rho(\mathbf{V} \cdot \nabla)\mathbf{V} = -\nabla p + \frac{1}{4\pi}(\nabla \times \mathbf{B}) \times \mathbf{B} - \frac{\rho G M}{r^2}\mathbf{r}, \tag{3.4}$$

$$(\mathbf{V}\cdot\nabla)\left(\frac{p}{(\Gamma-1)\rho}\right)+(p\mathbf{V}\cdot\nabla)\left(\frac{1}{\rho}\right)=\sigma. \tag{3.5}$$

To determine the temperature, we need an equation of state, which in this case will be taken as the perfect gas law,

$$T=\frac{m_p}{2k_B}\frac{p}{\rho}. \tag{3.6}$$

In the above equations, $\mathbf{V}$ the velocity, $\mathbf{B}$ the magnetic field, ρ the density, p the pressure, T the temperature, σ the rate of addition of external energy per unit mass of fluid are the variables, while G the gravitational constant, M the mass of the central object, m_p the mass of a proton, k_B the Boltzmann's constant and Γ the ratio of specific heats are given constants.

We shall follow the general approach introduced in Chapter 2. The main goal will be to seek the most general separable solutions of the above system of equations. The distribution of the heating rate σ will be deduced self-consistently in order to conserve energy.

First we will assume axial symmetry. Furthermore, to make the above equations more tractable from an analytical point of view, a second simplifying assumption will be made: both the velocity and the magnetic fields will be taken as helicoidal without meridional components (*i.e.* $V_\theta = B_\theta = 0$). As we've seen in Sect. 2.2, this restriction on the velocity field, together with the assumption of axisymmetry, means that the streamlines are helices around cones of opening angle θ (their projections on the meridional plane are $\Psi(\theta) = const$, and correspond to straight lines $\theta = \text{const}$). Similarly, Eq.(3.1) and the condition $\partial/\partial\phi = 0$ enables us to define the poloidal magnetic field as

$$\mathbf{B}_P(r,\theta)=\nabla\times\left(\frac{A(r,\theta)}{r\sin\theta}\hat{\mathbf{e}}_\phi\right), \tag{3.7}$$

where $A(r,\theta)$ is the magnetic flux function. Thus, $B_\theta = 0$ implies that $A = A(\theta)$ and the magnetic field lines also have helicoidal geometry.

The system of equations, Eqs.(3.1)-(3.5), including both scalar and vector equations, can be re-written explicitly as a system of 7 scalar equations in 7 unknowns (V_r, V_ϕ, B_r, B_ϕ, ρ, p, and σ)

$$\frac{\partial}{\partial r}(B_r r^2)=0, \tag{3.8}$$

$$\frac{\partial}{\partial r}(rV_\phi B_r - rV_r B_\phi)=0, \tag{3.9}$$

$$\frac{\partial}{\partial r}(\rho r^2 V_r)=0, \tag{3.10}$$

$$\rho V_r\frac{\partial V_r}{\partial r}-\rho\frac{V_\phi^2}{r}=-\frac{\partial p}{\partial r}-\frac{B_\phi^2}{4\pi r}-\frac{B_\phi}{4\pi}\frac{\partial B_\phi}{\partial r}-\frac{\rho GM}{r^2}, \tag{3.11}$$

$$\rho V_\phi^2 \frac{\cos\theta}{\sin\theta} = \frac{\partial p}{\partial \theta} + \frac{B_r}{4\pi}\frac{\partial B_r}{\partial \theta} + \frac{B_\phi^2}{4\pi}\frac{\cos\theta}{\sin\theta} + \frac{B_\phi}{4\pi}\frac{\partial B_\phi}{\partial \theta}, \tag{3.12}$$

$$\rho V_r \frac{\partial V_\phi}{\partial r} + \rho \frac{V_r V_\phi}{r} = \frac{B_r B_\phi}{4\pi r} + \frac{B_r}{4\pi}\frac{\partial B_\phi}{\partial r}, \tag{3.13}$$

$$V_r \frac{\partial}{\partial r}\left(\frac{p}{(\Gamma-1)\rho}\right) + p V_r \frac{\partial}{\partial r}\left(\frac{1}{\rho}\right) = \sigma. \tag{3.14}$$

At this stage, we introduce a third simplifying assumption, namely that the variables r and θ be separable. This will transform the above system of partial differential equations into a system of ordinary differential equations and thus analytically more tractable.

3.2.2 Method of Solution

Denoting by r_0 the radius at the base of the atmosphere, we can non-dimensionalise all quantities with respect to their values at this reference level. In particular, $R = r/r_0$. Using the assumption of separation of variables, we can write the radial velocity, the azimuthal velocity and the azimuthal magnetic field as, respectively,

$$V_r(R,\theta) = V_0 Y(R) v_r(\theta), \tag{3.15}$$

$$V_\phi(R,\theta) = V_1 P(R) v_\phi(\theta), \tag{3.16}$$

$$B_\phi(R,\theta) = B_1 M(R) b_\phi(\theta), \tag{3.17}$$

where V_0, V_1 and B_1 correspond to their reference values. Note that, at this stage, the functions $v_r(\theta)$, $v_\phi(\theta)$ and $b_\phi(\theta)$ are completely arbitrary. From Eqs.(3.8), (3.10) we must have

$$B_r(R,\theta) = B_0 \frac{b_r(\theta)}{R^2}, \tag{3.18}$$

$$\rho(R,\theta) = \rho_0 \frac{g(\theta)}{Y R^2}, \tag{3.19}$$

with B_0 and ρ_0 as the values of the radial magnetic field and density at the reference level, while $b_r(\theta)$ and $g(\theta)$ are yet to be determined. Note that the radial magnetic field has a monopole geometry modified by the presence of $b_r(\theta)$.

Using the same technique as described in Chapter 2, let's eliminate the pressure term between the r- and θ- components of the momentum equation, Eqs.(3.11), (3.12), by differentiating the first one with respect to θ and the second with respect to r, and adding them. The resulting expression is

$$\frac{\partial}{\partial\theta}\left(\rho\frac{V_\phi^2}{r}\right)-\frac{\partial}{\partial\theta}\left(\rho V_r\frac{\partial V_r}{\partial r}\right)-\frac{1}{4\pi}\frac{\partial}{\partial\theta}\left(\frac{B_\phi^2}{r}\right)-\frac{1}{4\pi}\frac{\partial}{\partial\theta}\left(B_\phi\frac{\partial B_\phi}{\partial r}\right)-\frac{\partial}{\partial\theta}\left(\frac{\rho GM}{r^2}\right)$$
$$-\frac{\partial}{\partial r}\left(\rho V_\phi^2\frac{\cos\theta}{\sin\theta}\right)+\frac{1}{4\pi}\frac{\partial}{\partial r}\left(B_r\frac{\partial B_r}{\partial\theta}\right)+\frac{1}{4\pi}\frac{\partial}{\partial r}\left(B_\phi^2\frac{\cos\theta}{\sin\theta}\right)+\frac{1}{4\pi}\frac{\partial}{\partial r}\left(B_\phi\frac{\partial B_\phi}{\partial\theta}\right)=0. \tag{3.20}$$

Under the assumption of separation of variables, the above equation will be transformed into an ordinary differential equation involving functions of R alone. For that purpose, the functions of θ in each term must be proportional to one another. Thus, equating the two last terms, we may write

$$b_\phi\frac{\mathrm{d}b_\phi}{\mathrm{d}\theta}=\epsilon b_\phi^2\frac{\cos\theta}{\sin\theta}, \tag{3.21}$$

which implies that

$$\frac{\mathrm{d}}{\mathrm{d}\theta}\left(\frac{b_\phi^2}{\sin^{2\epsilon}\theta}\right)=0, \tag{3.22}$$

or, similarly

$$b_\phi(\theta)=\sin^\epsilon\theta, \tag{3.23}$$

where ϵ is an arbitrary constant. Note that the constant of integration arising from integrating the right-hand side of Eq.(3.22) has been set to unity, without loss of generality. Any other value for this constant can be incorporated into the radial dependence of $B_\phi(R,\theta)$. In what follows, the choice of the constants of proportionality between different terms as well as the constants of integration will be made so as to obtain the simplest possible solutions, without loss of generality. Between the 7^{th} and 8^{th} term, we can put

$$b_r\frac{\mathrm{d}b_r}{\mathrm{d}\theta}=\mu\epsilon b_\phi^2\frac{\cos\theta}{\sin\theta}, \tag{3.24}$$

giving

$$b_r(\theta)=\sqrt{1+\mu\sin^{2\epsilon}\theta}, \tag{3.25}$$

where μ is a constant. The 5^{th} and 8^{th} terms may be equated to give

$$\frac{\mathrm{d}g}{\mathrm{d}\theta}=2\delta\epsilon b_\phi^2\frac{\cos\theta}{\sin\theta}, \tag{3.26}$$

thus resulting in

$$g(\theta)=1+\delta\sin^{2\epsilon}\theta, \tag{3.27}$$

in which δ is the third arbitrary constant. As for the 6^{th} and 8^{th} terms we can write

$$g v_\phi^2 = b_\phi^2, \tag{3.28}$$

or, equivalently,

$$v_\phi(\theta) = \frac{\sin^\epsilon \theta}{\sqrt{1 + \delta \sin^{2\epsilon} \theta}}. \tag{3.29}$$

Finally, from the ϕ-component of the momentum equation, Eq.(3.13), and for the variables R and θ to separate in this expression, we must have

$$g v_r v_\phi = b_r b_\phi, \tag{3.30}$$

giving

$$v_r(\theta) = \sqrt{\frac{1 + \mu \sin^{2\epsilon} \theta}{1 + \delta \sin^{2\epsilon} \theta}}. \tag{3.31}$$

Equating the four remaining terms in Eq.(3.20) — 1^{st}, 2^{nd} 3^{rd} and 4^{th} — we obtain identities, provided the proportionality constants are chosen accordingly.

We have thus deduced the most general θ-dependences for the density and hydromagnetic field, under the assumption of separation of variables, Eqs.(3.23), (3.25), (3.27), (3.29) and (3.31). These include three arbitrary constants: δ, ϵ, μ. We recall that in the hydrodynamic case already treated, these same anisotropy parameters were present. They effectively controlled the anisotropy in the outflow and in the density distribution. In this present model, the expressions for $b_r(\theta)$ and $b_\phi(\theta)$ do not introduce any new parameters.

To restrict the allowed values of μ, let us return to Eq.(3.25). For B_r to decrease from pole to equator we must have $\mu < 0$. Furthermore, the above expression is only valid for $\mu \geq -1$. Another point worth mentioning has to do with the change in nature of the solution from $\mu = -1$ to $\mu \neq -1$. From Eqs.(3.25), (3.31) it is obvious that both the radial magnetic field and radial velocity attain a zero at the equator only for $\mu = -1$. For all other allowed values of this parameter both these quantities are different from zero. This property of the radial velocity was already present in the hydrodynamic model.

High values of the radial velocity more concentrated around the polar axis occur for higher values of δ and $|\mu|$ and lower values of ϵ, Eq.(3.31) and Fig. 2.1. The density is highly concentrated around the equator for high values of ϵ, while increasing δ results in higher densities but with a more isotropic distribution, Eq.(3.27) and Fig. 2.3.

In a previous model, Tsinganos and Trussoni (1991) – hereafter refered as TT91 – started their analysis by choosing a priori the simplest possible forms of $b_r(\theta)$, $g(\theta)$ and $v_r(\theta)$ that were able to simulate existing observations on the solar wind. Their *ad hoc* expressions constitute a special case of the more general forms deduced in this work, for $\epsilon = 1$ and $\mu = -1$.

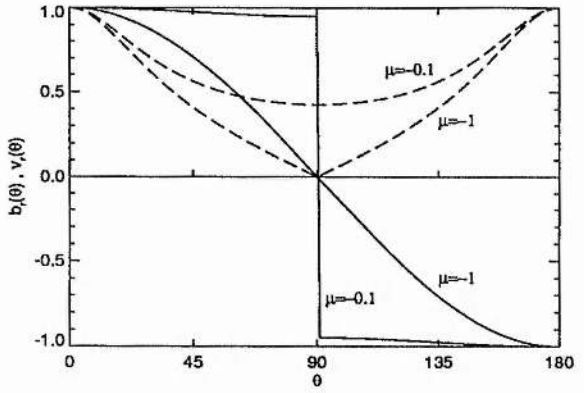

Figure 3.1: Latitudinal dependence of the radial magnetic field $b_r(\theta)$ (solid line) and of the radial velocity (dashed line) for $\epsilon = 1$ and $\delta = 4$

We should also draw attention to the direction of the hydromagnetic field in the two opposite hemispheres. The radial velocity, as deduced in Eq.(3.31) is directed outwards in both hemispheres. It represents an outflow in a natural way. However, from Eq.(3.25), b_r is defined as positive, *i.e.* directed outwards. If we want to model a realistic magnetic field that changes sign across the equator to conserve magnetic flux, we should use (b_r, b_ϕ) in one hemisphere and $-(b_r, b_\phi)$ in the opposite one. The latter is still a solution of Eq.(3.24). Note however, that there is a discontinuity in the radial magnetic field at the equator, for $\mu \neq -1$, with a corresponding current sheet, as in the terrestrial magnetosphere. This is illustrated in Fig. 3.1. Also, the sign reversal of b_ϕ across the equator is reminiscent of a dynamo-type azimuthal magnetic field as is indeed observed in sunspots. In the case of collimated outflows, this sign reversal favours the existence of bipolar outflows , whereas one sided jets are more often associated with an azimuthal field that does not change sign across the equator.

Mass Efflux

Another quantity of interest is the mass efflux, $\rho V_r r^2$, or, equivalently, the mass loss rate per infinitesimal solid angle $d\Sigma$ at the angle θ (see TT91). From the equation of conservation of mass Eq.(3.3) this has to be a function of θ alone

$$\rho V_r r^2 \equiv \dot{m}(\theta) = \rho_0 V_0 r_0^2 \sqrt{1 + \mu \sin^{2\epsilon}\theta}\sqrt{1 + \delta \sin^{2\epsilon}\theta}. \tag{3.32}$$

Figure 3.2 shows the variation of the mass efflux with latitude. It attains a zero at the equator only for $\mu = -1$, since the radial velocity vanishes there (see Eq.(3.31)). In this case, $\dot{m}(\theta)$ is maximum between the pole and the equator, the precise location of this extremum depending on the value of ϵ (and δ). It occurs for lower latitudes the bigger ϵ is, as illustrated in Fig. 3.2(a).

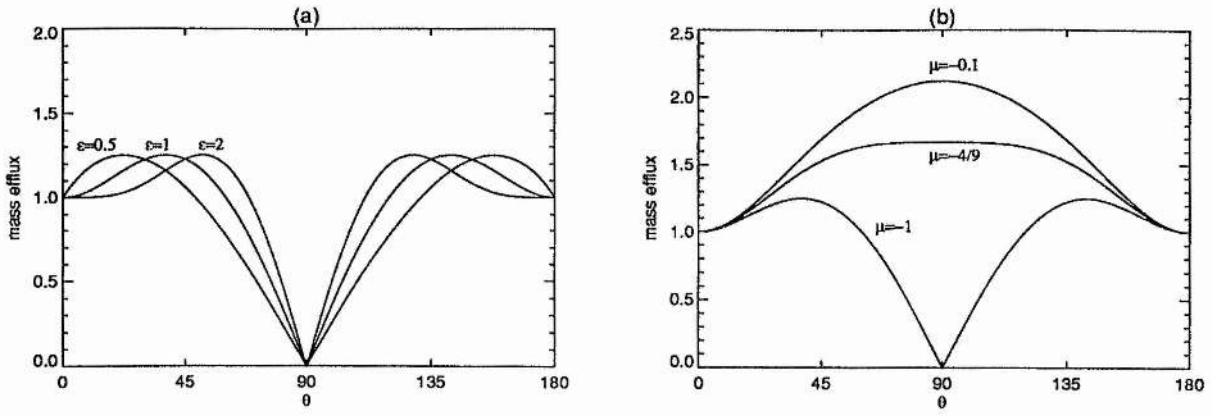

Figure 3.2: Latitudinal dependence of the mass efflux $\dot{m}(\theta)$ for $\delta = 4$: in **(a)** for $\mu = -1$, in **(b)** for $\epsilon = 1$

More precisely, we have

$$\frac{d\dot{m}}{d\theta} = \rho_0 V_0 r_0^2 \epsilon \sin^{2\epsilon-1}\theta \cos\theta \left(\mu \sqrt{\frac{1+\delta\sin^{2\epsilon}\theta}{1+\mu\sin^{2\epsilon}\theta}} + \delta \sqrt{\frac{1+\mu\sin^{2\epsilon}\theta}{1+\delta\sin^{2\epsilon}\theta}} \right), \tag{3.33}$$

which is always zero for $\theta = 90°$. Also,

$$\left(\frac{d^2\dot{m}}{d\theta^2}\right)_{\theta=90°} = -\rho_0 V_0 r_0^2 \epsilon \left(\mu \sqrt{\frac{1+\delta}{1+\mu}} + \delta \sqrt{\frac{1+\mu}{1+\delta}} \right), \tag{3.34}$$

which is negative for $\mu > -\delta/(2\delta+1)$. Thus, if $|\mu| < \delta/(2\delta+1)$ the maximum of $\dot{m}$ occurs for $\theta = 90°$, while if $|\mu| > \delta/(2\delta+1)$ it occurs for $0 < \theta < 90°$. This is shown in Fig.3.2(b). We simply note in passing that the first of these angular dependences of the mass loss is reminiscent of some observed intense mass loss rates that are thought to occur through equatorial stellar winds (*e.g.* from Be stars observed equator-on).

Angular Momentum and Angular Velocity

Going back to the ϕ-component of the momentum equation, Eq.(3.13), this can be manipulated to give

$$\frac{\partial}{\partial r}\left(r\sin\theta V_\phi - r\sin\theta \frac{B_r B_\phi}{4\pi\rho V_r} \right) = 0. \tag{3.35}$$

The solution to this equation introduces an arbitrary function of θ of the form

$$L(\theta) = r\sin\theta V_\phi - r\sin\theta \frac{B_r B_\phi}{4\pi\rho V_r}. \tag{3.36}$$

$L(\theta)$ is the total angular momentum per unit mass loss carried away by the wind, along each flow line $\theta = \text{const}$ (Weber and Davis, 1967). The first term on the right-hand side of Eq.(3.36) is the angular momentum carried by the advection of the flow while the second term represents the torque associated with the magnetic stresses.

Analogously, the solution to the induction equation, Eq.(3.9), introduces a further function of θ of the form

$$\Omega(\theta) = \frac{1}{r\sin\theta}\left(V_\phi - B_\phi\frac{V_r}{B_r}\right), \tag{3.37}$$

which corresponds approximately to the angular velocity of the roots of the field lines on the surface of the central object.

The azimuthal components of the velocity and magnetic fields can now be written in terms of these two free functions $L(\theta)$ and $\Omega(\theta)$. Thus, from Eqs.(3.36), (3.37) we arrive at

$$V_\phi = r_0\Omega(\theta)R\sin\theta\left(\frac{1 - M_A^2 L(\theta)/\Omega(\theta)r^2\sin^2\theta}{1 - M_A^2}\right), \tag{3.38}$$

$$B_\phi = \frac{B_0 r_0}{V_0\alpha^2}\Omega(\theta)R\sin\theta\sqrt{1+\delta\sin^{2\epsilon}\theta}\left(\frac{1 - L(\theta)/\Omega(\theta)r^2\sin^2\theta}{1 - M_A^2}\right), \tag{3.39}$$

where

$$V_0^A = \frac{B_0}{\sqrt{4\pi\rho_0}} \tag{3.40}$$

is the radial Alfvenic velocity at the base of the atmosphere,

$$\alpha = \frac{V_0^A}{V_0} \tag{3.41}$$

is the ratio of radial Alfvenic to radial velocities at the base, and

$$M_A^2 = \left(\frac{V_r}{V_A}\right)^2 = \frac{YR^2}{\alpha^2} \tag{3.42}$$

is the radial Alfvén Mach number (*i.e.*, the ratio of the radial velocity to the radial Alfvenic velocity, $V_A = B_r/\sqrt{4\pi\rho}$). An alternative physical interpretaion of α can be found from Eqs.(3.40), (3.41). In fact,

$$\alpha^2 = \frac{B_0^2/8\pi}{\rho_0 V_0^2/2}, \tag{3.43}$$

and represents the ratio of magnetic to kinetic energy density at the base of the atmosphere. If $\alpha \gg 1$, magnetic energy dominates there, whereas if $\alpha \ll 1$, most of the contribution comes from kinetic energy.

We want to find the most general forms of $L(\theta)$ and $\Omega(\theta)$ under the assumptions of this model. This will give us the form of the azimuthal hydromagnetic fields. In general, M_A starts

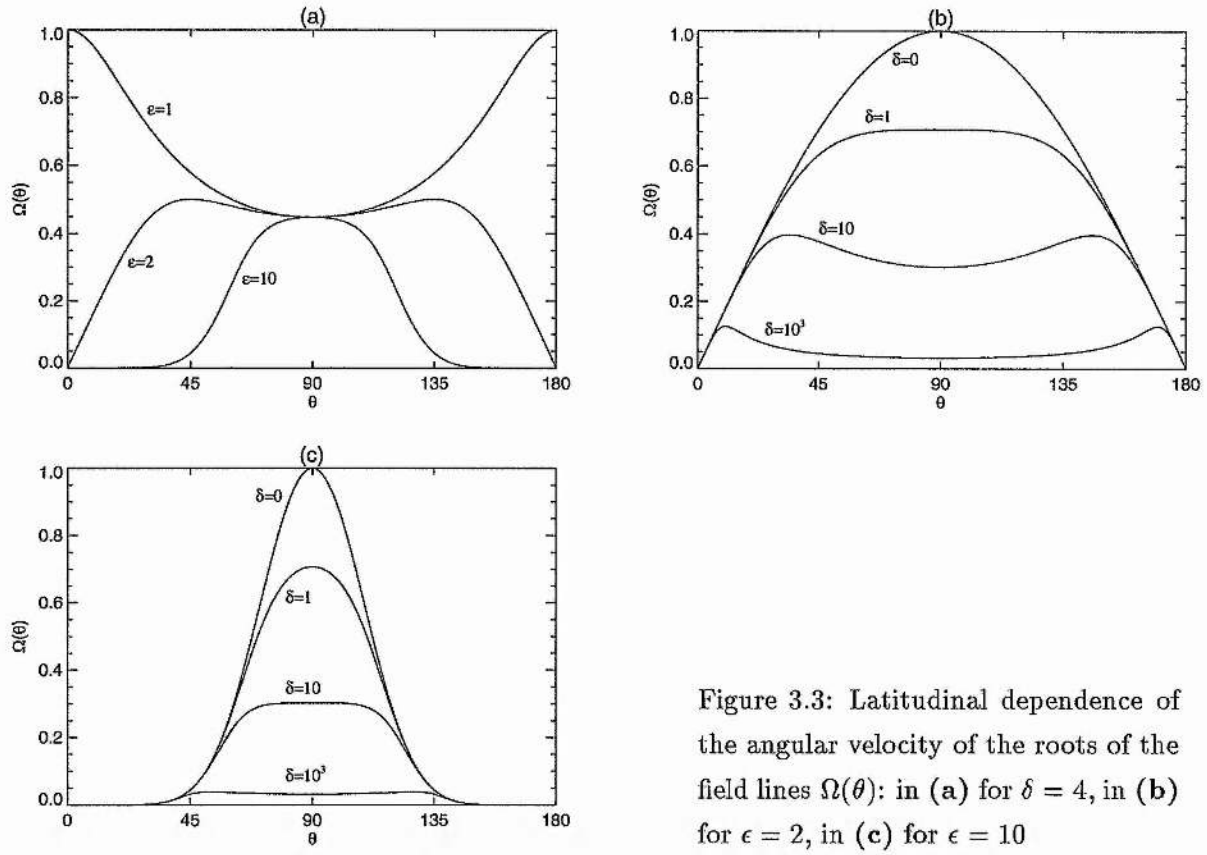

Figure 3.3: Latitudinal dependence of the angular velocity of the roots of the field lines $\Omega(\theta)$: in **(a)** for $\delta = 4$, in **(b)** for $\epsilon = 2$, in **(c)** for $\epsilon = 10$

with very small values ($M_A << 1$) at the base of the outflow and reaches very high asymptotic values ($M_A >> 1$) far away from the star. It is then obvious that there is a point at $R = R_*$, $Y = Y_* \equiv Y(R_*)$ for which $M_A = 1$ or, equivalently, the radial velocity of the outflow equals the radial Alfvenic velocity. At this point $Y_* R_*^2 = \alpha^2$. Looking back at Eqs.(3.38),(3.39), for both expressions to be finite at this critical point R_*, we must impose the condition that both the numerator and denominator vanish at the same time there. The result is an extra relationship between the two free functions $L(\theta)$ and $\Omega(\theta)$

$$L(\theta) = \Omega(\theta) r_*^2 \sin^2\theta. \tag{3.44}$$

This in turn leads to

$$V_\phi = \frac{r_0}{Y_*}\Omega(\theta)\sin\theta R\left(\frac{Y_* - Y}{1 - M_A^2}\right), \tag{3.45}$$

$$B_\phi = \frac{B_0 r_0}{V_0 Y_*}\frac{\Omega(\theta)\sin\theta\sqrt{1+\delta\sin^{2\epsilon}\theta}}{R}\left(\frac{R^2/R_*^2 - 1}{1 - M_A^2}\right). \tag{3.46}$$

If we now substitute Eqs.(3.29), (3.23) into Eqs.(3.16), (3.17), respectively, and compare the resulting expressions with Eqs.(3.45) and (3.46) we can deduce that $V_0 B_1 = V_1 B_0$, together with

the most general form for $\Omega(\theta)$,

$$\Omega(\theta) = \frac{\lambda V_0 Y_*}{r_0} \frac{\sin^{\epsilon-1}\theta}{\sqrt{1+\delta\sin^{2\epsilon}\theta}}, \tag{3.47}$$

where

$$\lambda = \frac{V_1}{V_0} = \frac{B_1}{B_0}, \tag{3.48}$$

$$L(\theta) = \lambda\alpha^2 V_0 r_0 \frac{\sin^{\epsilon+1}\theta}{\sqrt{1+\delta\sin^{2\epsilon}\theta}}. \tag{3.49}$$

The angular dependence of $\Omega(\theta)$ as the parameters ϵ and δ vary is worth of some attention and is plotted in Fig. 3.3. First note from these plots that for fixed δ, the behaviour of $\Omega(\theta)$ changes drastically as ϵ increases from its lowest value $\epsilon = 1$. For $\epsilon = 1$, $\Omega(\theta)$ has a *minimum* at the equator while for $\epsilon > 1$, $\Omega(\theta)$ has a *maximum* between pole and equator which moves closer to the equator the higher is the value of ϵ, Fig. 3.3(a). This maximum approaches the equator also when δ decreases for fixed $\epsilon \neq 1$ (Fig. 3.3(b)) and is more pronounced the larger is the value of ϵ, Fig. 3.3(c). This behaviour of $\Omega(\theta;\epsilon;\delta)$ which emerges naturally from the separation of variables in the governing equations can be compared, for example, with the rotation law of sunspots and solar photospheric magnetic fields where apparently Ω increases with θ in an analogous fashion. In fact, the graphs of Figs. 3.3(a,b,c) show a striking and remarkable similarity with the angular dependence of $\Omega(\theta)$ arising from the yearly-averaged rotation profiles of photospheric magnetic fields (Snodgrass, 1983; Wang et al., 1988; Wang et al., 1989; Nash, 1991). Thus, by comparing these observations of photospheric rotation profiles with the analytical expression given by Eq.(3.47) we may constrain the set of the allowed parameters (ϵ, δ) for solar applications. This will be explored in Chapter 4.

Close to the star, the torque associated with the magnetic stresses and represented by the second term in Eq.(3.36) dominates over the rotation term. For large distances from the star, where the magnetic field is already spread out, rotation takes over, and the first term in the above equation dominates. The requirement that a critical solution passes smoothly through the critical point ensures a constant flow of angular momentum across the interface between these two dynamically distinct regions, by fixing $L(\theta)$ for each field line $\theta = \text{const}$, as defined by Eq.(3.49). This condition ensures the system is in a steady state (Hu and Low, 1989).

Angular Momentum Efflux

We can now introduce the angular momentum efflux $\rho V_r r^2 L(\theta)$, or angular momentum loss rate per infinitesimal solid angle $d\Sigma$ at the angle θ,

$$\rho V_r r^2 L(\theta) \equiv \dot{l}(\theta) = \lambda\alpha^2\rho_0 V_0^2 r_0^3 \sin^{\epsilon+1}\theta\sqrt{1+\mu\sin^{2\epsilon}\theta}. \tag{3.50}$$

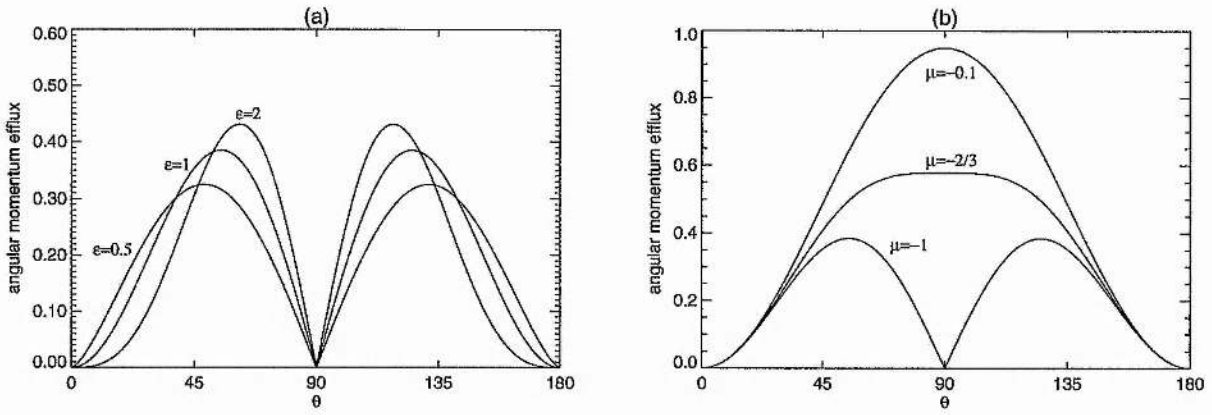

Figure 3.4: Latitudinal dependence of the angular momentum efflux $\dot{l}(\theta)$: in **(a)** for $\mu = -1$, in **(b)** for $\epsilon = 1$

The variation of $\dot{l}$ with latitude is shown in Fig. 3.4. As with the mass efflux, the angular momentum efflux vanishes at the equator for $\mu = -1$. In this case, the maximum of $\dot{l}$ is between pole and equator and increases with ϵ as in Fig. 3.4(a). An analysis of the extrema of Eq.(3.50) shows that the position of the maximum of $\dot{l}$ is critically dependent on the ratio $(\epsilon+1)/(2\epsilon+1)$. In fact,

$$\frac{d\dot{l}}{d\theta} = \lambda\alpha^2\rho_0 V_0^2 r_0^3 \sin^{\epsilon}\theta\cos\theta\left((\epsilon+1)\sqrt{1+\mu\sin^{2\epsilon}\theta} + \epsilon\mu\frac{\sin^{2\epsilon}\theta}{\sqrt{1+\mu\sin^{2\epsilon}\theta}}\right), \tag{3.51}$$

which is zero for $\theta = 90°$, while

$$\left(\frac{d^2\dot{l}}{d\theta^2}\right)_{\theta=90°} = -\lambda\alpha^2\rho_0 V_0^2 r_0^3\left((\epsilon+1)\sqrt{1+\mu} - \epsilon\frac{\mu}{\sqrt{1+\mu}}\right). \tag{3.52}$$

Thus, the second derivative of $\dot{l}$ at the equator is negative for $|\mu| < (\epsilon+1)/(2\epsilon+1)$, meaning that the angular momentum efflux is maximum there. If, on the contrary, $|\mu| > (\epsilon+1)/(2\epsilon+1)$, $\dot{l}$ is maximised somewhere between pole and equator. This is illustrated in Fig. 3.4(b) where for $\epsilon = 1$, this maximum occurs for $\theta = 90°$ when $|\mu| < 2/3$. In general, if $|\mu| < 1/2$ the maximum is at the equator, while if $|\mu| > 2/3$ it is always between pole and equator, provided $\epsilon > 1$.

In the TT91 model, the angular momentum efflux was assumed a priori, from which the simplest possible forms for the azimuthal hydromagnetic field were obtained. Furthermore, they imposed the constraints that $\dot{l}(\theta)$ should vanish at the pole and at the equator, and have a maximum value in between. In our more general analysis, the form of the angular momentum efflux is a direct consequence of the separation of variables and reproduces their results for $\epsilon = 1$, $\mu = -1$.

Solution for the Hydromagnetic Field and Density

The azimuthal components can now be obtained by substituting Eq.(3.47) into Eqs.(3.45), (3.46), and using Eq.(3.48)

$$V_\phi(R,\theta) = V_1 \frac{R\sin^\epsilon\theta}{\sqrt{1+\delta\sin^{2\epsilon}\theta}}\left(\frac{Y_*-Y}{1-M_A^2}\right), \tag{3.53}$$

$$B_\phi(R,\theta) = B_1 \frac{\sin^\epsilon\theta}{R}\left(\frac{R^2/R_*^2-1}{1-M_A^2}\right). \tag{3.54}$$

Note that V_ϕ is maximum at the equator. We recall that the radial hydromagnetic field and density are of the form

$$V_r(R,\theta) = V_0 Y(R)\sqrt{\frac{1+\mu\sin^{2\epsilon}\theta}{1+\delta\sin^{2\epsilon}\theta}}, \tag{3.55}$$

$$B_r(R,\theta) = \frac{B_0}{R^2}\sqrt{1+\mu\sin^{2\epsilon}\theta}, \tag{3.56}$$

$$\rho(R,\theta) = \frac{\rho_0}{YR^2}\left(1+\delta\sin^{2\epsilon}\theta\right). \tag{3.57}$$

Analogously to the hydrodynamic case, we can also define an "effective " sound speed and Mach number, as given by Eqs.(2.52), (2.53).

The reference values of the various quantities at the base correspond to

$$V_0 = V_r(R=1,\theta=0°), \tag{3.58}$$

$$V_1 = \sqrt{1+\delta}\left(\frac{1-1/\alpha^2}{\alpha^2/R_*^2-1}\right) V_\phi(R=1,\theta=90°), \tag{3.59}$$

$$B_0 = B_r(R=1,\theta=0°), \tag{3.60}$$

$$B_1 = \left(\frac{1-1/\alpha^2}{1/R_*^2-1}\right) B_\phi(R=1,\theta=90°), \tag{3.61}$$

$$\rho_0 = \rho(R=1,\theta=0°). \tag{3.62}$$

3.2.3 Balance of Forces and Conservation of Energy

At this stage, we still have to deduce an equation for $Y(R)$, together with the form for the pressure $p(R,\theta)$ — and hence the temperature $T(R,\theta)$ — and for the heating rate $\sigma(R,\theta)$. Going back to the r- and θ- components of the momentum equation – Eqs.(3.11) and (3.12), and for the variables R and θ to separate in these equations, we must have

$$Q(R,\theta) = Q_0(R) + Q_1(R)\sin^{2\epsilon}\theta, \tag{3.63}$$

similarly to the hydrodynamic case. $Q(R,\theta)$ is the dimensionless pressure defined by Eq.(2.32), while Q_0 represents the spherically symmetric part of the pressure and Q_1 includes the effects of the anisotropy. Substitution of Eqs.(2.32), (3.63) into Eqs.(3.11) and (3.12) yields the following three equations for $Q_0(R)$, $Q_1(R)$ and $Y(R)$

$$Q_1(R) = -\frac{\mu\alpha^2}{R^4} + \frac{\lambda^2}{\epsilon Y}\left(\frac{Y-Y_*}{1-M_A^2}\right)^2 - \left(1+\frac{1}{\epsilon}\right)\frac{\lambda^2\alpha^2}{R^2}\left(\frac{1-R^2/R_*^2}{1-M_A^2}\right)^2, \tag{3.64}$$

$$\frac{\mathrm{d}Q_1}{\mathrm{d}R} = -\frac{\delta\nu^2}{YR^4} - \frac{2\mu}{R^2}\frac{\mathrm{d}Y}{\mathrm{d}R} + \frac{2\lambda^2}{YR}\left(\frac{Y-Y_*}{1-M_A^2}\right)^2 - \frac{\lambda^2\alpha^2}{R^2}\frac{\mathrm{d}}{\mathrm{d}R}\left(\frac{1-R^2/R_*^2}{1-M_A^2}\right)^2, \tag{3.65}$$

$$\frac{\mathrm{d}Q_0}{\mathrm{d}R} = -\frac{\nu^2}{YR^4} - \frac{2}{R^2}\frac{\mathrm{d}Y}{\mathrm{d}R}, \tag{3.66}$$

$$\tag{3.67}$$

in which ν is the ratio of the escape speed to the radial speed at the base of the outflow as defined by Eqs.(2.17),(2.18).

To understand the interplay between different forces involved in the mechanism of this type of winds, let's describe one by one the various terms in the above equations. All of them are written so that the pressure gradient term is isolated on the left-hand side. Equation (3.64) represents the force equilibrium across the fieldlines. On the right-hand side of this, the various terms represent, repectively, the magnetic pressure, the centrifugal force and the magnetic tension. The last two equations express the equilibrium of forces along the radial direction. Equation (3.65) shows the anisotropic terms, namely, the anisotropic part of the gravitational and inertial forces, the centrifugal force and the magnetic tension term, respectively. The isotropic terms are shown on Eq.(3.66). These are related to the gravitational and inertial forces, respectively.

Equations (3.64) and (3.65) can be combined to give a single expression for $Y(R)$

$$\frac{\mathrm{d}Y}{\mathrm{d}R} = \frac{F(R)}{G(R)}, \tag{3.68}$$

where

$$F(R) = \frac{\delta\nu^2}{YR^4} + \frac{4\mu\alpha^2}{R^5} + \frac{2\lambda^2}{\epsilon}\frac{Y}{RM_A^2(1-M_A^2)^2}\left[\left(\frac{(1+\epsilon)M_A^2-\epsilon}{M_A^2}\right)\frac{R^4}{R_*^4} - ((2+\epsilon)M_A^2-(1+\epsilon))\right], \tag{3.69}$$

$$G(R) = -\frac{2\mu Y}{\alpha^2 M_A^2} - \frac{\lambda^2}{\epsilon(1-M_A^2)^2}\left[\left(\frac{2M_A^2-1}{M_A^4}\right)\frac{R^4}{R_*^4} - 1\right].$$

The above differential equation for $Y(R)$ requires a boundary condition. For convenience, we have chosen $Y(1) = 1$, which defines $V_0 = V_r(R = 1, \theta = 0)$, from Eq.(3.55).

From Eq.(1.21), we can now express temperature as

$$T(R,\theta) = \frac{mV_0^2}{2k_B}\frac{YR^2}{(1+\delta\sin^{2\epsilon}\theta)}\left[Q_0(R) + Q_1(R)\sin^{2\epsilon}\theta\right]. \tag{3.70}$$

Finally, from the heat equation Eq.(3.14) and for the variables to separate we must have

$$\sigma(R,\theta) = \left[\sigma_0(R) + \sigma_1(R)\sin^{2\epsilon}\theta\right]\frac{(1+\mu\sin^{2\epsilon}\theta)^{1/2}}{(1+\delta\sin^{2\epsilon}\theta)^{3/2}}, \tag{3.71}$$

analogously to the hydrodynamic case, where $\sigma_0(R)$ and $\sigma_1(R)$ are defined by Eqs.(2.37), (2.38). As previously (Chapter 2), the distribution of heating rate with latitude is such that there is a higher concentration of σ close to the pole for higher values of δ and $|\mu|$ and lower values of ϵ, Fig. 2.4.

3.3 The Special Case with $B_r = 0$

When there is only an azimuthal magnetic field B_ϕ but the velocity keeps both components, V_r and V_ϕ, the problem is significantly simplified. Because all the θ - dependences can be derived from a set of equations similar to Eqs.(3.11) and (3.12), with the term in B_r dropped in the last equation, it is obvious that $v_r(\theta)$, $g(\theta)$, $v_\phi(\theta)$ and $b_\phi(\theta)$ are the same as in the previous section. The radial velocity and density are still given by Eqs.(3.55) and (3.57), while the radial dependences of the azimuthal hydromagnetic field can be easily obtained from the conservation of angular momentum, Eq.(3.36), and from the induction equation, Eq.(3.9),

$$V_\phi(R,\theta) = \frac{\lambda V_0}{R}\frac{\sin^\epsilon\theta}{\sqrt{1+\delta\sin^{2\epsilon}\theta}}, \tag{3.72}$$

$$B_\phi(R,\theta) = \frac{B_1}{YR}\sin^\epsilon\theta. \tag{3.73}$$

These two expressions no longer contain a singularity at $R = R_*$. Since there is no poloidal magnetic field, the Alfvén Mach number, Eq.(3.42), is infinite.

Following the same procedure as in the previous section, we obtain for the pressure the following set of equations,

$$Q_1(R) = \frac{\lambda^2}{\epsilon Y R^4} - \left(1+\frac{1}{\epsilon}\right)\frac{\Lambda^2}{Y^2R^2}, \tag{3.74}$$

$$\frac{\mathrm{d}Q_1}{\mathrm{d}R} = -\frac{\delta\nu^2}{YR^4} - \frac{2\mu}{R^2}\frac{\mathrm{d}Y}{\mathrm{d}R} + \frac{2\lambda^2}{YR^5} + \frac{2\Lambda^2}{Y^3R^2}\frac{\mathrm{d}Y}{\mathrm{d}R}, \tag{3.75}$$

$$\frac{\mathrm{d}Q_0}{\mathrm{d}R} = -\frac{\nu^2}{YR^4} - \frac{2}{R^2}\frac{\mathrm{d}Y}{\mathrm{d}R}, \tag{3.76}$$

where we have introduced a new parameter

$$\Lambda = \frac{V_1^A}{V_0} = \frac{B_1}{\sqrt{4\pi\rho_0}V_0}, \tag{3.77}$$

namely the ratio of the Alfvenic velocity associated with the azimuthal magnetic field and the radial velocity, at the base of the atmosphere. Eqs.(3.74), (3.75) can now be combined to give

$$\frac{\mathrm{d}Y}{\mathrm{d}R} = \frac{Y}{R}\left[\frac{\epsilon\delta\nu^2R - 2(\epsilon+2)\lambda^2 + 2(\epsilon+1)\Lambda^2R^2/Y}{-2\epsilon\mu Y^2R^2 + \lambda^2 - 2\Lambda^2R^2/Y}\right]. \tag{3.78}$$

This equation has a critical point at $R = R_X$, $Y = Y_X$, say. In general, the position of this critical point has to be defined implicitly by imposing the condition that both the numerator and the denominator vanish at the same time. However, for $\delta = 0$ (spherically symmetric density), R_X and Y_X are given explicitly by

$$R_X = \left(\frac{\epsilon+3}{2\epsilon(\epsilon+1)|\mu|}\right)^{1/6}\left(\frac{\epsilon+2}{(\epsilon+1)\Lambda^2}\right)^{1/3}\lambda, \tag{3.79}$$

$$Y_X = \left(\frac{\epsilon+3}{2\epsilon(\epsilon+1)|\mu|}\right)^{1/3}\left(\frac{(\epsilon+1)\Lambda^2}{\epsilon+2}\right)^{1/3}, \tag{3.80}$$

and

$$R_X Y_X = \left(\frac{\epsilon+3}{2\epsilon(\epsilon+1)|\mu|}\right)^{1/2}\lambda. \tag{3.81}$$

3.3.1 Nature of Critical Point (R_X, Y_X)

In the simpler case $\delta = 0$, let us perform a first-order analysis around (R_X, Y_X). Similarly to Eq.(2.41) we can write

$$R = R_X(1+\alpha), \quad Y = Y_X(1+\tau) \tag{3.82}$$

and ignore terms of second-order and higher in α, τ. Substituting Eqs.(3.82) into Eq.(3.78), for $\delta = 0$, and using Eqs.(3.79), (3.80), we find

$$\frac{\mathrm{d}\tau}{\mathrm{d}\alpha} = \frac{c\alpha + e\tau}{a\alpha + b\tau}, \tag{3.83}$$

with

$$\begin{aligned} a &= -4R_X^2\Lambda^2 - 4\epsilon\mu R_X^2 Y_X^3, \\ b &= \lambda^2 Y_X - 6\epsilon\mu R_X^2 Y_X^3, \\ c &= 4(\epsilon+1)\Lambda^2 R_X^2, \\ e &= -2(\epsilon+2)\lambda^2 Y_X. \end{aligned}$$

We are now in a position to use the results of Appendix A to classify the nature of (R_X, Y_X). After some manipulation, we can write

$$a + e = -4R_X^2\Lambda^2 - 2\lambda^2 Y_X\left(\frac{\epsilon^2+2\epsilon}{\epsilon+1}\right), \tag{3.84}$$

which is always negative. Also,

$$-4(ae-bc) = 16\lambda^2 Y_X\left((\epsilon+2)\lambda^2 Y_X + (2\epsilon+5)\Lambda^2 R_X^2\right), \tag{3.85}$$

is always positive. Thus, the determinant Δ given by Eq.(A.7) is always positive, while $m_2 < 0 < m_1$, from Eq.(A.6). This falls into Case 2 of Table A.1 and the critical point (R_X, Y_X) is a saddle point (also called an $X-$type point). The slopes of the two solutions that cross it

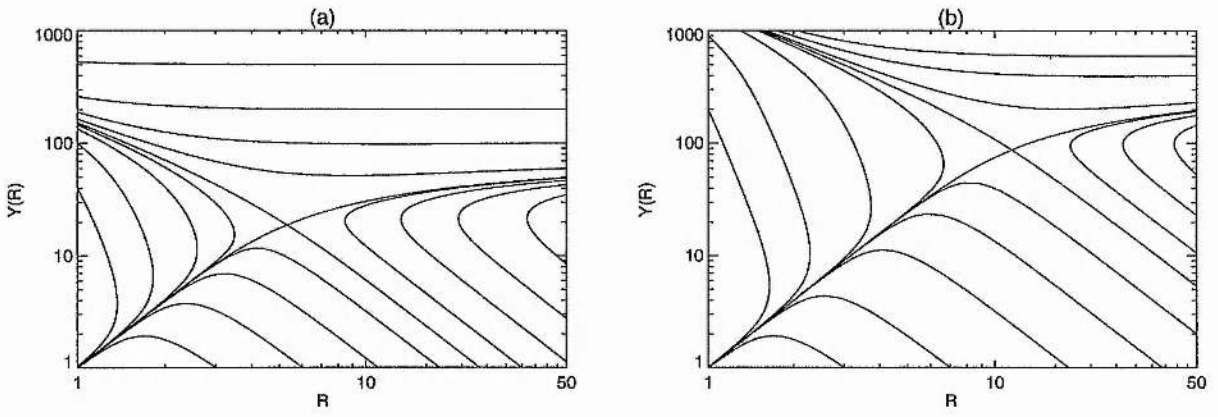

Figure 3.5: Topology of the radial dependence of the radial velocity $Y(R)$ for $\nu = 120$, $\lambda = \Lambda = 100$, $\delta = 0$, $\epsilon = 1$: in **(a)** for $\mu = -1$, in **(b)** for $\mu = -0.01$. Note the presence of the X-type critical point

are given by Eq.(A.8). They have opposite signs with $s_2 < 0 < s_1$, since $4bc > 0$ and thus $\Delta = \sqrt{(a-e)^2 + 4bc} > |(a-e)|$.

This critical point, introduced by TT91, is crucial in choosing the wind-type solution. It must be connected to the azimuthal magnetic field since when $\Lambda = 0$ there is no critical point. Recent suggestions (Tsinganos, 1994) indicate that it corresponds to the point where the radial component of the flow speed V_r equals the slow/fast MHD mode wave speed in that direction. Note that this last characteristic speed is defined in this case by the solution of a quartic involving the sound speed and the Alfvén speed associated with the azimuthal magnetic field (V_1^A in Eq.(3.77)).

3.3.2 Typical Solution

Having found the slopes across the critical point it is possible to integrate numerically Eq.(3.78). Fig. 3.5 shows two examples for $\lambda = \Lambda = 100$ and different values of μ. Note that there is only one wind-type solution, filtered out by the X-type point. The position of R_X moves downstream with μ approaching zero. Also, the asymptotic value of Y for large distances increases with a decrease of the absolute value of μ. In fact, in this limit, the dominant terms in Eq.(3.78) yield,

$$\frac{\mathrm{d}Y}{\mathrm{d}R} \simeq \frac{Y}{R}\left[\frac{2(\epsilon+1)\Lambda^2 R^2}{-2\epsilon\mu Y^3 R^2}\right], \tag{3.86}$$

which gives, after integration,

$$Y^3 \simeq \left(\frac{2(\epsilon+1)\Lambda^2}{\epsilon\,|\,\mu\,|}\right)\ln R. \tag{3.87}$$

3.4 Parametric Study of the Solution

3.4.1 Nature of Critical Points

In order to determine the full solution we need to solve Eq.(3.68), (3.69) for $Y(R)$. This is a first-order non-linear differential equation which can be integrated numerically, using a standard routine.

A first inspection shows that this equation has a critical point at $R = R_*$, $Y = Y_*$, where $M_A = 1$, or in other words where the radial velocity equals the radial Alfvenic velocity $V_A = B_r/\sqrt{4\pi\rho}$. The term critical point is used here in the sense that both the numerator and denominator must vanish there. In a more general geometry with meridional components, this point, known as the Alfvenic point, corresponds to the point where the poloidal speed equals the poloidal Alfvén speed. It is present in most magnetic wind models (Weber and Davis, 1967; Mestel, 1968) and is a consequence of the steady-state assumption. It delimits the magnetically dominated region beyond which the torque exerted by the magnetic field ceases to dominate over the angular momentum carried by the fluid. The exact position of this point cannot be found analytically in this case, which complicates any type of numerical treatment as we shall see later.

However, we can find its nature by means of a first-order analysis around it, analogously to what we did in the case with $B_r = 0$. Before that we must write Eqs.(3.68), (3.69) in another form

$$\frac{\mathrm{d}Y}{\mathrm{d}R} = \frac{2\lambda^2 Y^2 R^4[M_A^2((1+\epsilon)(1+R^4/R_*^4) - (2+\epsilon)M_A^2) - \epsilon R^4/R_*^4] + (\delta\nu^2 R + 4\mu\alpha^2 Y)\epsilon M_A^4(1-M_A^2)^2}{\lambda^2 Y R^5(M_A^4 - 2R^4/R_*^4 M_A^2 + R^4/R_*^4) - 2\epsilon\mu Y R^3 M_A^4(1-M_A^2)^2}. \tag{3.88}$$

A first-order expansion around (R_*, Y_*) yields, after substitution into the above expression, an equation of the form given in Appendix A (Eq.(A.1)), with $a = e = 1$ and $b = c = 0$. Thus, from Eq.(A.6), $m_1 = m_2 = 1$, and we are in Case 3 of Table A.1. This gives us a node (proper or improper). To be able to distinguish between the two, we should carry on the expansion into higher orders beyond the first. In a similar problem, TT91 find that expanding up to fourth order around (R_*, Y_*), all slopes are allowed. We are thus in the presence of a proper node, also called star-type point. This means that no particular solution is filtered out by the presence of this critical point.

There is a second critical point, (R_X, Y_X), say, found by satisfying simultaneously $F = G = 0$ in Eq.(3.69). Again using Eq.(3.88) and a first-order analysis around this point, we arrive at Eq.(A.1) with

$$
\begin{aligned}
a &= -6\epsilon\mu Y_X^2 R_X^3 M_A^4(X)(1-M_A^2(X))^2 - 8\epsilon\mu M_A^4(X)(1-M_A^2(X))(1-2M_A^2(X)) \\
&\quad +9\lambda^2 Y_X^2 R_X^5 M_A^4(X) + \lambda^2 Y_X^2 R_X^9/R_*^4(9-22M_A^2(X)) \\
b &= -2\epsilon\mu Y_X^2 R_X^3 M_A^4(X)(1-M_A^2(X))^2 - 4\epsilon\mu M_A^4(X)(1-M_A^2(X))(1-2M_A^2(X)) \\
&\quad +3\lambda^2 Y_X^2 R_X^5 M_A^4(X) + \lambda^2 Y_X^2 R_X^9/R_*^4(1-4M_A^2(X)) \\
c &= \epsilon\delta\nu^2 R_X^2 M_A^4(X)(1-M_A^2(X))^2 + 4\epsilon(\delta\nu^2 R_X^2 + 4\mu\alpha^2 R_X Y_X) M_A^4(X)(1-M_A^2(X))(1-2M_A^2(X)) \\
&\quad +4\lambda^2 Y_X^2 R_X^5 M_A^2(X)(3-4(2+\epsilon)M_A^2(X)) - 4\lambda^2 Y_X^2 R_X^9/R_*^4(4-5M_A^2(X)) \\
e &= 4\epsilon\mu Y_X^2 R_X^3 M_A^4(X)(1-M_A^2(X))^2 2\epsilon(\delta\nu^2 R_X^2 + 4\mu\alpha^2 R_X Y_X) M_A^4(X)(1-M_A^2(X))(1-2M_A^2(X)) \\
&\quad +2\lambda^2 Y_X^2 R_X^5 M_A^2(X)(3+3R_X^4/R_*^4 - 4M_A^2(X)) - 4\epsilon\lambda^2 Y_X^2 R_X^9/R_*^4
\end{aligned}
$$

where $M_A(X) = M_A(R = R_X)$.

It can be shown numerically that for the parameters of interest m_1 and m_2 given by Eq.(A.6) are always real, unequal and of unlike sign (Case 2 of Table A.1). Thus we are in the presence of a saddle or $X-$type point. Only two slopes are allowed through (R_X, Y_X), one positive and one negative (see Eq.(A.8)).

We should stress at this point that both the Alfvenic point, (R_*, Y_*), and this $X-$type point, are (loosely) called equilibrium or critical points since they satisfy the regularity condition $F(R) = G(R) = 0$. However, while the first one does not filter any solution (*i.e.* all slopes are allowed through it), this second one (as any saddle point) selects a particular type of solution, sometimes refered as the critical solution.

The position of (R_X, Y_X) can be given in approximate form in the limits $\alpha \gg 1$ and $M_A \gg 1$

$$
\begin{aligned}
R_X &\approx R_*^{4/3}\left[\frac{(\epsilon+3)}{2\epsilon|\mu|(\epsilon+1)}\right]\left[\left(\frac{\epsilon+2}{\epsilon+1}\right)\lambda\right]^{1/3}, \\
Y_X &\approx Y_*^{2/3}\left[\frac{(\epsilon+3)}{2\epsilon|\mu|(\epsilon+1)}\right]\left[\left(\frac{\epsilon+1}{\epsilon+2}\right)(\lambda\alpha)^2\right]^{1/3}.
\end{aligned}
\tag{3.89}
$$

We performed a numerical integration of Eqs.(3.68), (3.69) using the Adams method (NAG Fortran library). The general topology is shown in Fig.3.6 for a highly magnetized medium and for different values of μ and ϵ. The position of the critical points was found by the following iterative procedure. In the first step an estimate of R_* was used and the corresponding value of Y_* was determined using $Y_* R_*^2 = \alpha^2$. The position of R_X, Y_X was obtained by solving numerically the system $F(R) = 0$, $G(R) = 0$, for $M_A \neq 1$, Eq.(3.88). Special care was taken in ignoring spurious solutions. The second step consisted in the numerical integration of Eq.(3.68) from $R = R_X(1-\eta)$, where η is a small parameter, until $R = 1$. To integrate across the Alfvenic point, we used a constant slope in a small region around R_*. In the third step, the solution at the base of the atmosphere is considered. If $Y(1) > 1$, then we take a higher estimate for R_* and return to the first step. If, on the contrary, $Y(1) < 1$, a smaller R_* is chosen. The whole

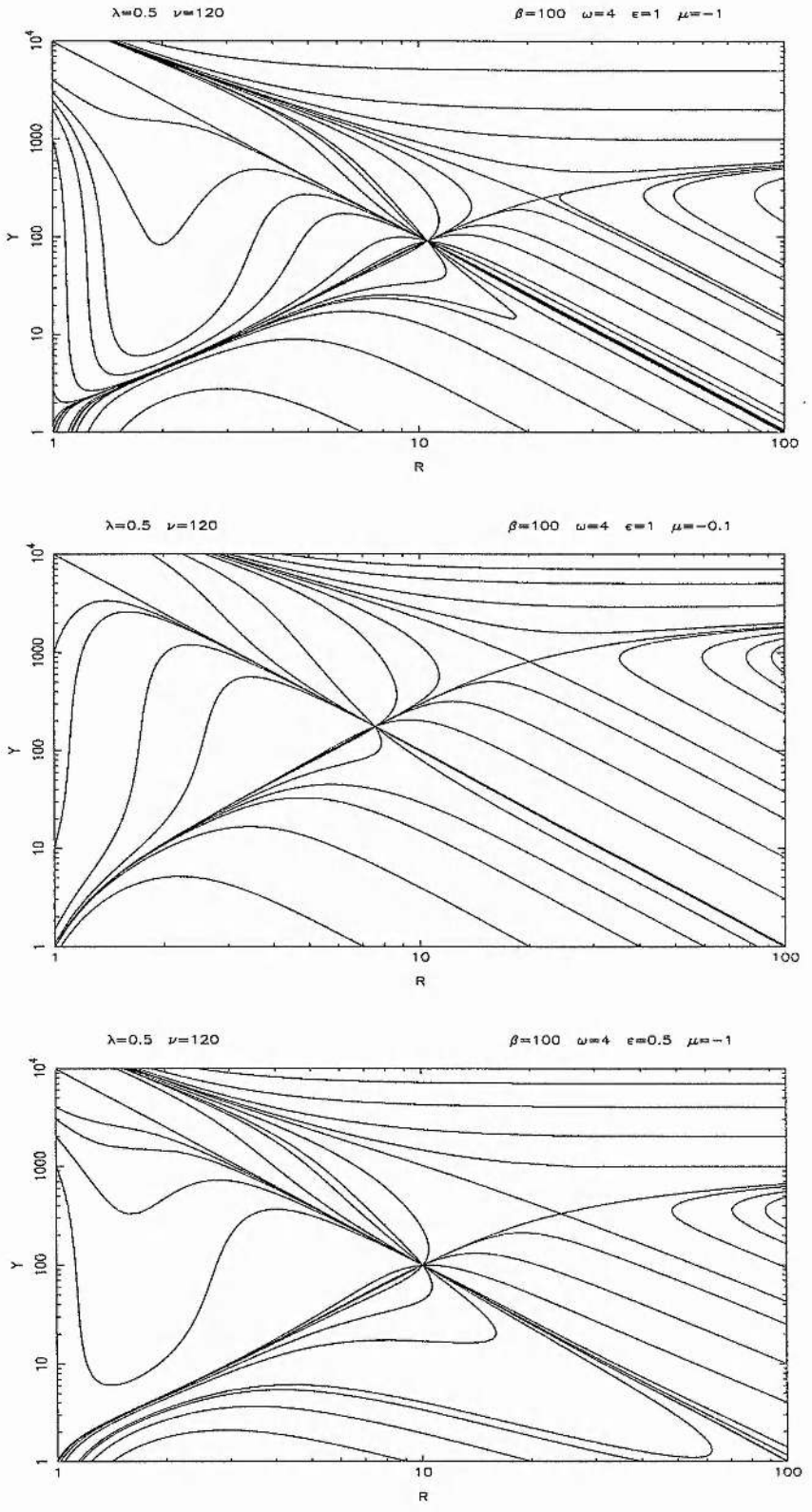

Figure 3.6: Topology of the radial dependence of the radial velocity $Y(R)$ for a solar-type highly magnetized star with $\lambda = 0.5$, $\nu = 120$, $\alpha = 100$, $\delta = 4$: in **(a)** for $\epsilon = 1$, $\mu = -1$, in **(b)** for $\epsilon = 1$, $\mu = -0.1$, in **(c)** for $\epsilon = 0.5$, $\mu = -1$. Note the presence of both critical points

ϵ	μ	R_*	R_X
0.5	-1	1.312	1.385
1	-1	1.248	1.285
2	-1	1.210	1.229
1	-0.1	1.157	1.168
1	-0.01	1.148	1.155
1	-0.001	1.147	1.153

(a)

ϵ	μ	R_*	R_X
0.5	-1	10.064	24.220
1	-1	10.550	21.862
2	-1	11.038	19.577
1	-0.1	7.581	20.084
1	-0.01	7.429	28.297
1	-0.001	7.413	41.173

(b)

Table 3.1: Location of both critical points for $\lambda = 0.5$, $\nu = 120$, $\delta = 4$: in **(a)** for $\alpha = 10$, in **(b)** for $\alpha = 100$

procedure is repeated, until a value of $Y(1)$ sufficiently close to 1 is found. We are thus left with a single solution crossing the $X-$type point with positive slope (s_1 from Eq.(A.8)) and satisfying the boundary condition $Y(1) = 1$. For this critical solution, the flow starts near the star with low speeds and connects to large distances where it attains large super-Alfvenic velocities. There is another critical solution, which crosses the X-type point with negative slope (s_2 form Eq.(A.8)) and is always decelerating. It corresponds to an accretion flow. There is a limiting value of ϵ above which we couldn't find a wind solution satisfying the boundary condition $Y(1) = 1$. For example, if $\lambda = 0.5$, $\nu = 120$ and $\delta = 4$, there is no solution for $\epsilon \gtrsim 5$, if $\alpha = 10$ and for $\epsilon \gtrsim 2$, if $\alpha = 100$.

Once the positions of both R_* and R_X are known, all other types of solutions can be easily found. They include breeze-type solutions that cross the Alfvenic point but not the X-type point, and reach sub-Alfvenic asymptotic speeds for large distances. Table 1 shows the position of both critical points for $\alpha = 10$ and $\alpha = 100$ and different values of ϵ and μ. We have taken $\lambda = 0.5$, $\nu = 120$ and $\delta = 4$, characteristic of a solar-type object. For $\alpha = 10$, both critical points are very close to each other and just outside the base of the atmosphere. As α increases, they move outwards and separate. The position of R_* shifts upstream as μ approaches zero, thus reducing the size of the magnetically dominated region. Striking is the fact that R_* moves inwards with an increase of ϵ for $\alpha = 10$, while the opposite is true for $\alpha = 100$.

3.4.2 Radial Velocity

In the case of a highly magnetized star ($\alpha = 100$), Fig. 3.7 shows that the initial acceleration is larger for $\mu = -1$ and decreases as μ appproaches zero. It also increases with an increase of ϵ. In fact, for $\alpha \gg 1$, the acceleration at $R \approx 1$ is given by (see Eqs.(3.68), (3.69))

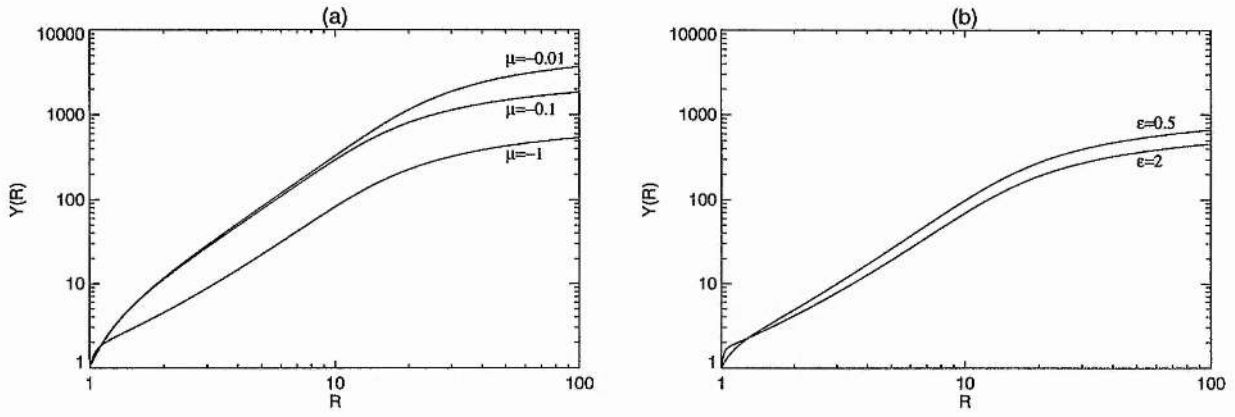

Figure 3.7: Radial dependence of the dimensionless radial velocity $Y(R)$ for a solar-type highly magnetized star with $\lambda = 0.5$, $\nu = 120$, $\alpha = 100$, $\delta = 4$: in **(a)** for $\epsilon = 1$, in **(b)** for $\mu = -1$

$$\frac{\mathrm{d}Y}{\mathrm{d}R} \approx \frac{(\epsilon\delta\nu^2 + 4\epsilon\mu\alpha^2) + 2\lambda^2\alpha^2(\epsilon + 1 - \epsilon\alpha^2/R_*^4)}{-2\epsilon\mu + \lambda^2(1 + \alpha^4/R_*^4)}. \tag{3.90}$$

Since $\lambda \approx 1$ and $\alpha \gg R_*$, the contribution of ϵ and μ in the denominator of the above expression is negligible. From the numerator, the initial acceleration increases with ϵ and decreases as μ approaches zero. To understand this we take $\delta = 0$, without any loss of generality. In other words, the gravitational force is independent of latitude. For $\mu = -1$, the radial velocity at the equator is zero, Eq.(3.55). Under these static conditions, the weight of the plasma is balanced by the centrifugal force and by the radial component of the Lorentz force, Eq.(3.11). At the pole and the same radial distance R, these two forces vanish due to their dependence on $\sin^{2\epsilon}\theta$ and we are left with only the same plasma weight. The result is a decelerating force which is bigger the greater is the drop of $\sin^{2\epsilon}\theta$ close to zero. Since this sinusoidal function decays more rapidly for smaller values of ϵ, we have an initial acceleration of the flow that increases with ϵ. For the case $\mu > -1$, there is an extra factor to balance the weight of the plasma at the equator, namely the inertial force due to the radial velocity no longer being zero there. The deceleration effect as we move to the pole is now increased, relative to the case $\mu = -1$. The initial acceleration is thus smaller for smaller values of $|\mu|$.

Using the same argument, it is easy to show that the acceleration close to the base drops as we increase α. In fact, while at the equator there is usually a positive (*i.e.* directed outwards) radial component of the Lorentz force, at the pole this force vanishes and so the result is a decelerating force, increasing with α. For a mildly magnetized case ($\alpha = 10$), Fig. 3.8 shows that the initial acceleration is very high and the radial velocity rapidly attains its asymptotic value. The variation with λ is similar since now the missing force at the pole is the centrifugal one. In

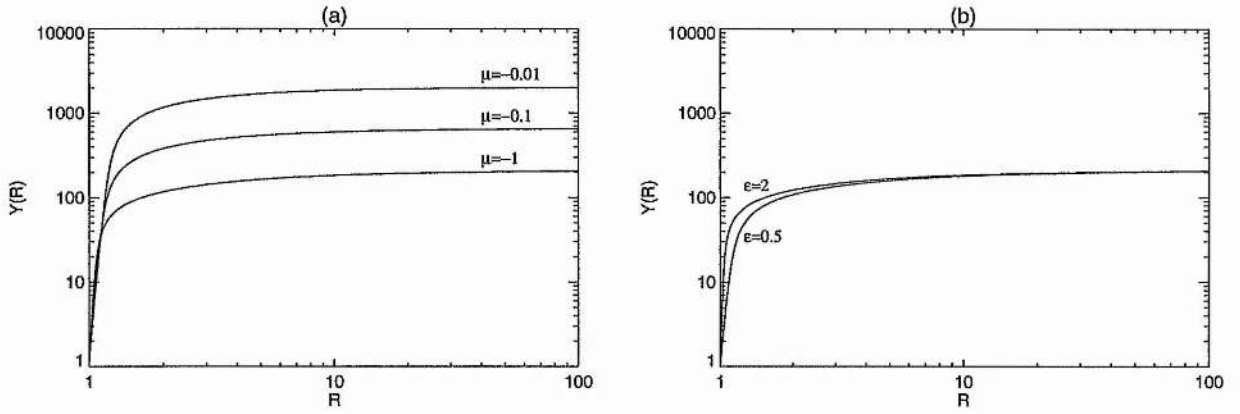

Figure 3.8: Radial dependence of the dimensionless radial velocity $Y(R)$ for a solar-type mildly magnetized star with $\lambda = 0.5$, $\nu = 120$, $\alpha = 10$, $\delta = 4$: in **(a)** for $\epsilon = 1$, in **(b)** for $\mu = -1$

other words, both the magnetic field and rotation are inhibiters of the initial acceleration of the outflow.

This acceleration at the base also increases with δ as in a purely hydrodynamic wind. The reason for this is associated with the fact that as we move from the equator to the pole, and for the same distance, the decrease of the plasma density is proportional to δ while the pressure only decreases slightly. There is an extra force at the pole to accelerate the wind and this force is larger the higher δ is (TT91).

When R is large, $Y(R)$ tends asymptotically to a certain value that can be considered, as a first approximation, independent of R (see Figs.3.7,3.8). This is clearly the case for low values of α. We can thus write

$$Y \rightarrow Y_\infty, \quad M_A^2 \rightarrow \frac{Y_\infty R^2}{\alpha^2}. \tag{3.91}$$

Under these conditions, $F(R)$ is dominated by the third term in Eq.(3.69), yielding

$$F \simeq \frac{2(\epsilon+1)\lambda^2\alpha^6}{\epsilon Y_\infty^2 R_*^4}\frac{1}{R^3}. \tag{3.92}$$

All other terms decay more rapidly with R. As for $G(R)$, the most important terms when R is large are the first two in Eq.(3.69), decaying as $1/R^2$. The ratio between first and second depends on $\epsilon\mu Y_\infty^3 R_*^4/\alpha^6\lambda^2$. For $\alpha \sim 1$ this is much greater than one, since Y_∞^3 dominates. For higher values of α, this is still greater than one since Eq.(3.91) now holds only for very high values of R. This can be seen by comparing Fig.3.7 (for $\alpha = 100$) with Fig.3.8 (for $\alpha = 10$). In the

former case, Y tends to a constant value much more slowly than in the later one. Thus, we can take

$$G \simeq -\frac{2\mu}{R^2} \tag{3.93}$$

and the asymptotic form of $Y(R)$ for large R can be obtained from Eqs.(3.92), (3.93) and after integrating Eq.(3.68)

$$Y^3 \simeq 3\left(1+\frac{1}{\epsilon}\right)\frac{\lambda^2\alpha^6}{|\mu|R_*^4}\ln R. \tag{3.94}$$

For $\alpha \gg 1$, the asymptotic speed increases logarithmically with R, and Y increases with an increase of α or a decrease of ϵ and $|\mu|$, as illustrated in Figs.3.7,3.8. Going back to Eq.(3.64), the second term on the right-hand side is negligible for $\alpha \gg 1$. Decreasing $|\mu|$ or ϵ makes Q_1 more negative, which results in a large pressure difference between the pole (where $Q = Q_0$) and equator (where $Q = Q_0 + Q_1$). This is responsible for higher terminal speeds as given by the above equation (see also TT91). When $\alpha < 1$, the logarithmic derivative $\mathrm{d}Y^3/\mathrm{d}\ln R$, for large R, is very small (behaving like α^6), and Y can be taken as constant. The flow is hydrodynamically dominated from $R = 1$, while both singular points, R_* and R_X, almost coincide in the region $R < 1$ (*i.e.* below the base of the atmosphere). We recall that in the hydrodynamic case (Chapter 2), Y approaches rapidly a constant value, independent of ϵ.

In summary, the effect of decreasing $|\mu|$ is on the one hand to diminish the relative importance of the magnetic effects by decreasing the size of the magnetically dominated region and, on the other hand, to increase the asymptotic value of the radial velocity. This is in contrast with the influence of α. As this parameter grows, the magnetic lever arm R_* increases and so does the asymptotic value of V_r. The global form of the outflow is much less sensitive to variations in ϵ.

3.4.3 Pressure

Once $Y(R)$ has been found, we can return to Eqs.(3.64), (3.66) and calculate the pressure. For large distances, the dominant term on the right-hand side of Eq.(3.66) is the second, giving the following asymptotic form for Q_0

$$Q_0 \simeq \left(1+\frac{1}{\epsilon}\right)\frac{\lambda^2\alpha^6}{|\mu|R_*^4 Y_\infty^2}\frac{1}{R^2}, \tag{3.95}$$

where Y_∞ is defined by Eq.(3.91). We have chosen the constant of integration so that Q_0 goes to zero when $R \to \infty$, as in a wind-type solution. In this limit, Y_∞ is almost constant, and so the above expression means that Q_0 decays to zero from positive values as $\sim 1/R^2$.

For $\alpha = 100$, Fig. 3.9(a) shows that Q_0 drops very steeply close to the base and after an intermediate "plateau", it decays as $1/R^2$ far from the surface. For $\alpha = 10$, Fig. 3.9(b), Q_0 takes its asymptotic form very close to the base of the atmosphere.

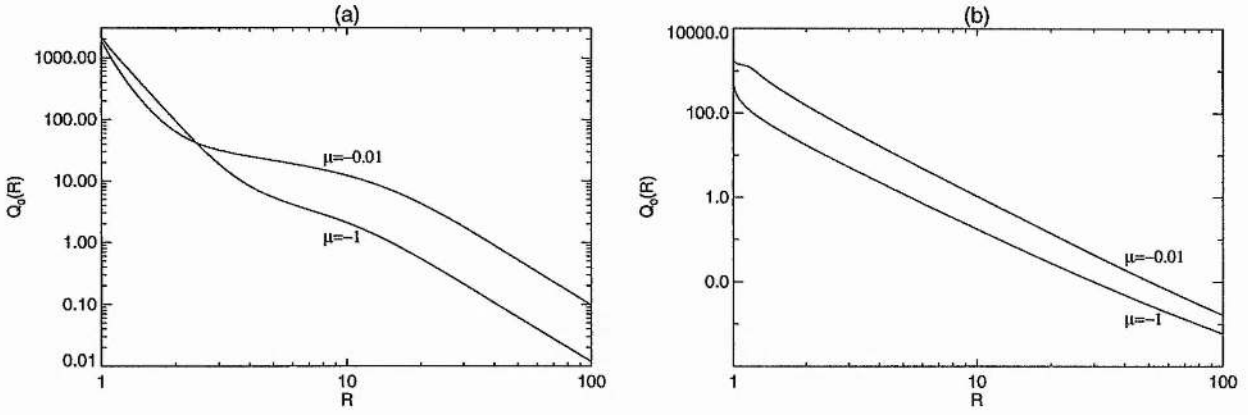

Figure 3.9: Radial dependence of the dimensionless pressure along the polar axis $Q_0(R)$ for a solar-type magnetized star with $\lambda = 0.5$, $\nu = 120$, $\delta = 4$, $\epsilon = 1$: in **(a)** for $\alpha = 100$, in **(b)** for $\alpha = 10$

But Q_0 represents only the spherically symmetric part of the pressure. The total pressure also includes the anisotropic part Q_1, given by Eq.(3.64). Close to the star, the first term in this equation, related to the magnetic pressure gradient, dominates over the others. This term is always positive and decays as $1/R^4$. As we move out from the star, this term ceases to dominate and the last term, associated with the magnetic tension, takes over (at least for $\alpha \gg 1$). This gives asymptotically

$$Q_1 \simeq -\left(1+\frac{1}{\epsilon}\right)\frac{\lambda^2\alpha^6}{R_*^4 Y_\infty^2}\frac{1}{R^2}. \tag{3.96}$$

In this limit of large distances, Q_1 increases to zero from negative values. There is thus a point, at some finite radius, for which Q_1 is minimum and negative. The total pressure is given by $Q = Q_0 + Q_1 \sin^{2\epsilon}\theta$. For large distances it is always positive. However, if Q_1 reaches a sufficiently low negative value then, for a certain range of values of R, Q can be negative and thus unphysical. We can find a limiting angle θ_m and limiting radius R_m beyond which ($\theta > \theta_m$, $R > R_m$) the total pressure becomes negative. Our solution would only be valid for $\theta < \theta_m$, i.e., in a cone around the polar axis.

This feature, already present in the TT91 model, is related to the constraint of keeping the field lines fixed as helices around the polar axis. They argued that force balance in the θ- direction implies that the magnetic tension term is directed towards the pole, as can be seen by the negative sign of the last term in Eq.(3.64). For large distances, the first two terms in this equation decay as $1/R^4$, while the negative tension term decays as $1/R^2$ and dominates. The only way to balance this is to have a pressure gradient $\mathrm{d}Q_1/\mathrm{d}R \sim Q_1/R$ decaying as $1/R^3$. Since the pressure at the pole is fixed by Q_0, then Q_1 has to be sufficiently low and negative so as to give a large and

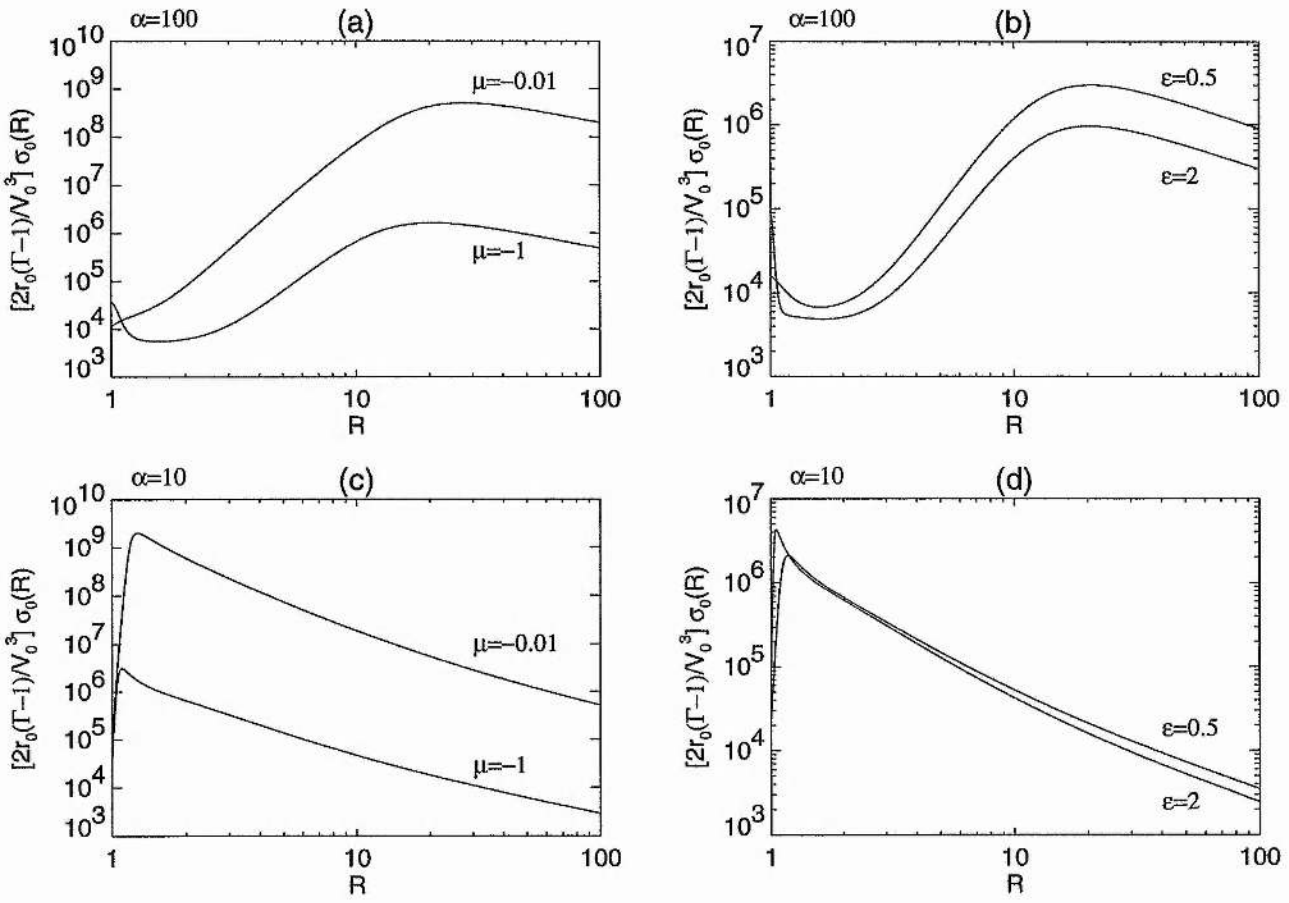

Figure 3.10: Radial dependence of the dimensionless heating rate along the polar axis $[2r_0(\Gamma-1)/V_0^3]\,\sigma_0(R)$ for a solar-type magnetized star with $\lambda = 0.5$, $\nu = 120$, $\delta = 4$: in **(a)** for $\alpha = 100$, $\epsilon = 1$, in **(b)** for $\alpha = 100$, $\mu = -1$, in **(c)** for $\alpha = 10$, $\epsilon = 1$, in **(d)** for $\alpha = 10$, $\mu = -1$

negative pressure difference between pole and equator, enough to balance the negative tension force.

The cone where the solution is valid becomes smaller for larger values of α and increases with a decrease of $|\mu|$ or ϵ. For $\alpha = 100$ and $\epsilon = 1$, $\theta_m = 16°$ if $\mu = -1$ and $\theta_m = 22°$ if $\mu = -10^{-3}$, while for $\alpha = 100$ and $\mu = -1$, $\theta_m = 24°$ for $\epsilon = 0.5$ and $\theta_m = 11°$ for $\epsilon = 2$. For $\alpha \leq 20$ and $\epsilon = 1$, the cone extends to the equator and the solution is valid everywhere.

3.4.4 Heating

Since the form of the heating rate was deduced self-consistently from the full set of equations through Eq.(3.5), it must reflect the acceleration of the outflow.

For a highly magnetized medium, $\alpha = 100$, Figs. 3.10(a,b) show that the heating rate at the

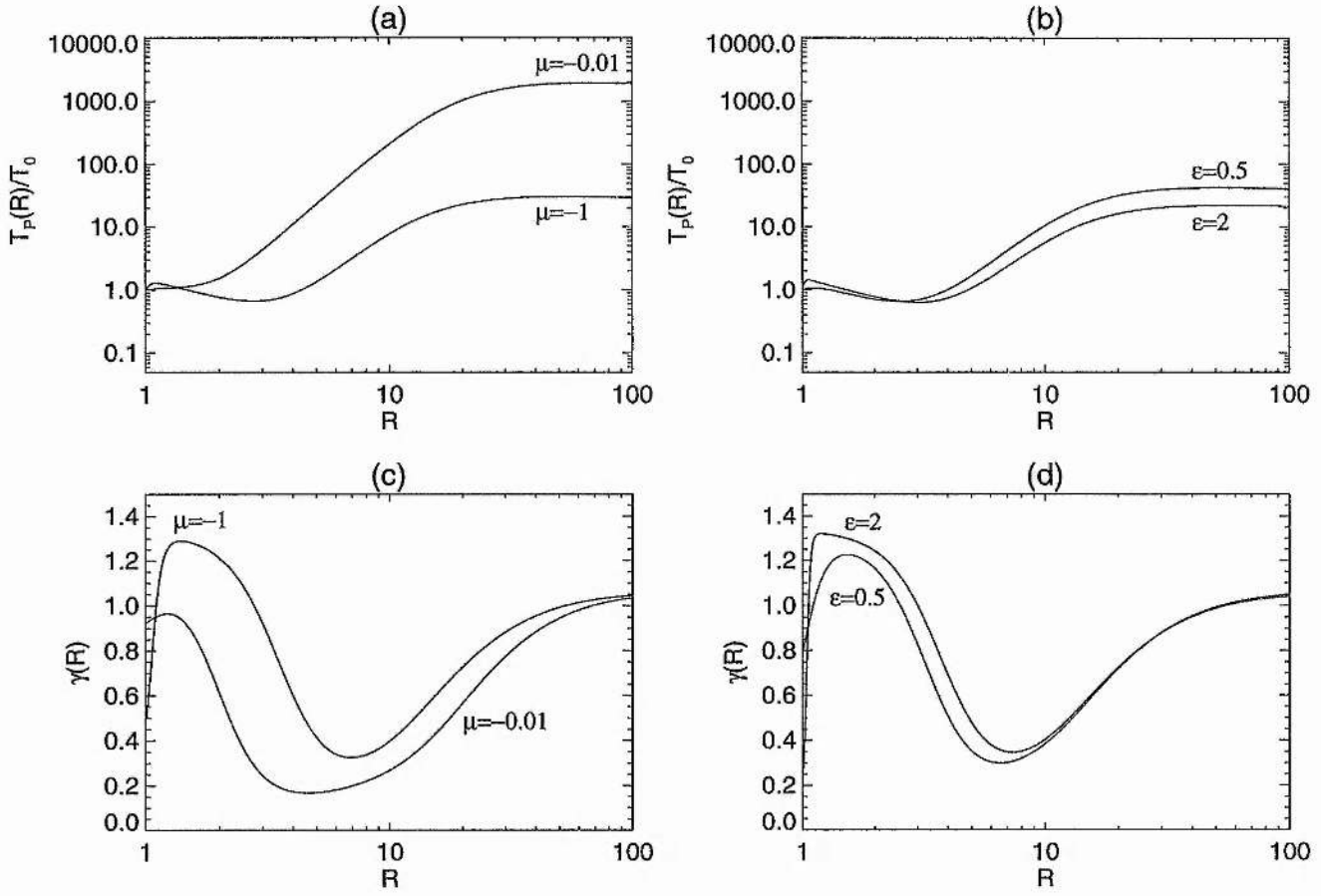

Figure 3.11: Radial dependence of the dimensionless temperature at the pole $T_P(R)/T_0$, where $T_0 = T_P(R = 1)$, and of the polytropic index $\gamma(R)$ for $\lambda = 0.5$, $\nu = 120$, $\alpha = 100$, $\delta = 4$: in **(a)** and **(c)** for $\epsilon = 1$, in **(b)** and **(d)** for $\mu = -1$

pole is low near the base of the star. This gives a reduced acceleration there, as was pointed out in Sect.3.6 (see Fig. 3.7). It then increases to a maximum further downstream and drops slowly further away. This higher concentration of σ_0 in the supersonic domain is more pronounced for values of μ closer to zero and for lower values of ϵ. It is responsible for the higher terminal speeds in these cases. Note also that for $\epsilon = 2$, Fig. 3.10(b) shows a high initial value of $\sigma_0 \sim 10^5$ reflected in a high initial acceleration as shown in Fig. 3.7(b). The heating then drops very steeply to values lower than those for $\epsilon = 0.5$. The corresponding acceleration of the outflow flattens out to smaller values than those for $\epsilon = 0.5$. Analogous crossings between these two sets of curves occurs for $\mu = -1$ and $\mu \neq -1$.

For lower values of α, the heating rate is more concentrated towards the base of the star (see Fig. 3.10(c,d)). The acceleration there is consequently higher than in the previous more magnetic case, (Fig.3.8). After a peak very close to the base, σ_0 then decays monotonically with distance and is unable to support a steady acceleration of the outflow. The radial velocity rapidly reaches

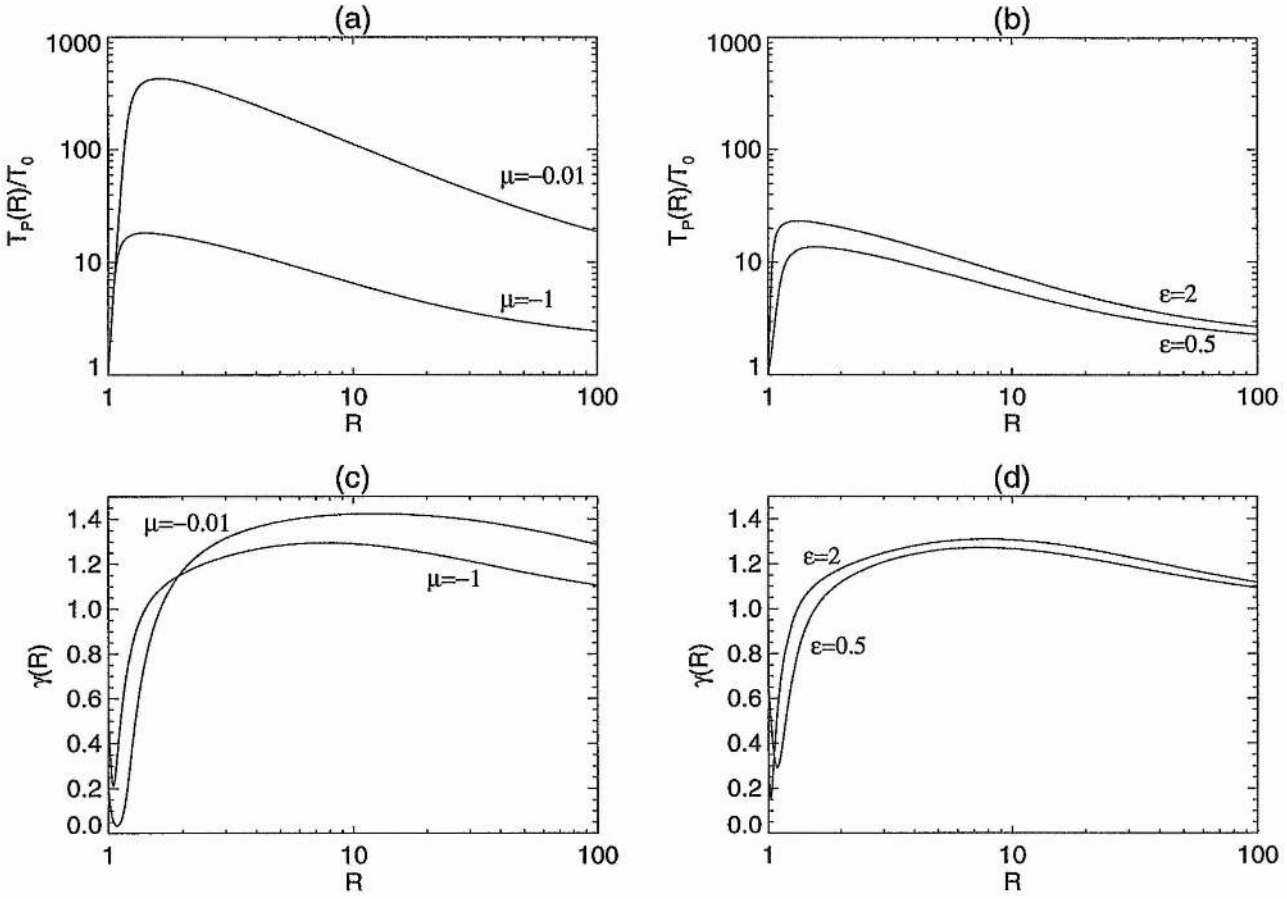

Figure 3.12: Radial dependence of the dimensionless temperature at the pole $T_P(R)/T_0$, where $T_0 = T_P(R = 1)$, and of the polytropic index $\gamma(R)$ for $\lambda = 0.5$, $\nu = 120$, $\alpha = 10$, $\delta = 4$: in **(a)** and **(c)** for $\epsilon = 1$, in **(b)** and **(d)** for $\mu = -1$

an almost-constant value, analogously to the purely hydrodynamic case described in Chapter 2. The total heating is larger the smaller $|\mu|$ is, resulting in higher asymptotic speeds.

3.4.5 Temperature and Polytropic Index

By using Eq.(3.5) instead of a polytropic relationship between pressure and density, $p \propto \rho^{\gamma}$, with γ as the constant polytropic index, we avoided constraining the exchange of energy so as to keep γ constant. From this more general approach, we can define an effective polytropic index by

$$\gamma \equiv \left[\frac{\partial ln p}{\partial ln \rho}\right]_{A=\text{const.}} \tag{3.97}$$

for each field line $A(\theta) = \text{const.}$ (see TT91). This is no longer a constant, but instead a function of R. The form of $\gamma(R)$ is closely associated with the variation of temperature with distance from the central object. In particular, if $\gamma < 1$ there is intense heating and the temperature increases,

while if $\gamma > 1$ there is a depletion of heating and the temperature decreases.

For $\alpha = 100$, the temperature is low at the base of the atmosphere and increases very slowly further out until it reaches an almost-constant asymptotic value at about $R \sim 30$, Fig 3.11(a,b). This value changes quite drastically with μ and ϵ. In particular, the asymptotic temperature increases with a decrease of $|\mu|$ or ϵ. These values can be compared with existing observations to constrain the values of these parameters.

The variation of the polytropic index, as shown in Fig. 3.11(c,d), presents a maximum close to the base. For $|\mu| \leq 0.1$ this maximum is still below $\gamma = 1$, with the result that the temperature always increases with distance. For $\mu = -1$, the maximum is above $\gamma = 1$, there is reduced heating and the temperature reaches a minimum. Further out, the distribution of the polytropic index shows a minimum below the isothermal value, corresponding to the region where the temperature is slowly increasing towards its asymptotic value. For large distances, γ approaches unity, as in an isothermal atmosphere.

For $\alpha = 10$, the temperature also starts with low values at the base, but now it increases rapidly to reach a maximum below $R \sim 2$, Fig. 3.12(a,b). It then decays very slowly with distance until an almost constant asymptotic value is reached. At $R = 100$, this value is 1 to 2 orders of magnitude lower than the corresponding one for $\alpha = 100$. The polytropic index in this case (Fig. 3.12(c,d)) shows a pronounced minimum very close to the base, where the temperature has a very steep gradient towards its maximum. After that, γ increases rapidly into a local maximum and falls off very slowly from then on. It approaches the isothermal value, although much more slowly than on the previous more magnetic case ($\alpha = 100$).

3.5 Two-dimensional Behaviour

We have chosen a mildly magnetized object ($\alpha = 10$) to illustrate the two-dimensional character of the solution deduced in this chapter.

Compare Fig. 3.13 with a similar one for an analogous hydrodynamic model, Fig. 2.7. The outflow speed at the pole (a quantity independent of all three anisotropy parameters) is smaller for this magnetic wind when compared to the fully hydrodynamic case. This is a consequence of the decrease of the initial acceleration with the magnetic field strength (*i.e.* with α), which essentially affects the radial velocity for small distances. Also the distribution of the sound speed (and temperature) is more uniform for the magnetized case, resulting in an almost isothermal atmosphere (Fig.3.14(a)). The highly anisotropic distribution of the Mach number, shown in Fig. 3.14(b), is a direct result of the fact that for $\mu = -1$ the radial velocity is always zero at the equator and so is the Mach number. Thus the sonic transition occurs close to the base for high latitudes and far from it near the equator.

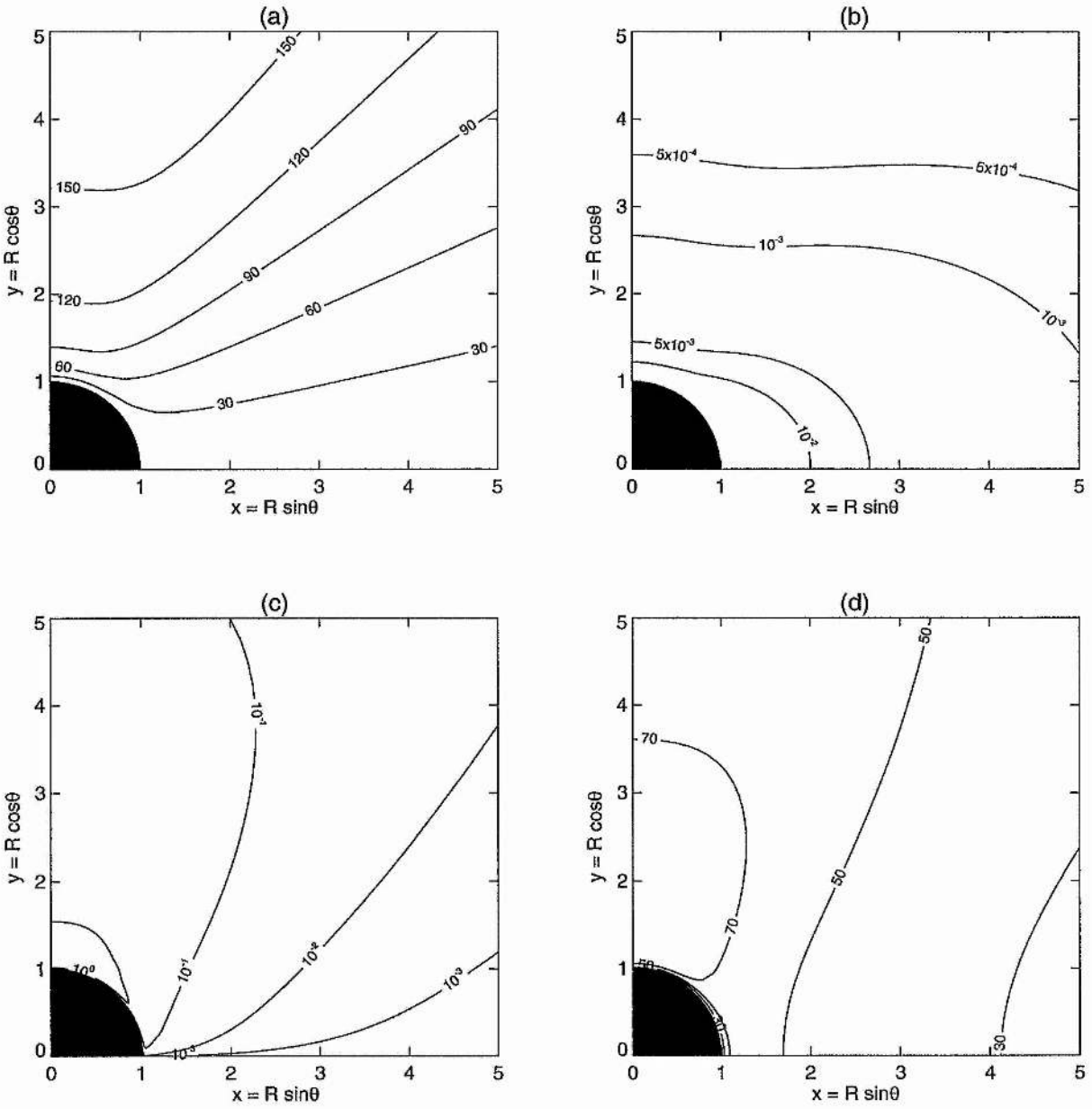

Figure 3.13: Contour plots of the radial velocity $V_r(R,\theta)/V_0$ in **(a)**, density $\rho(R,\theta)/\rho_0$ in **(b)**, heating rate $10^{-6}\sigma(R,\theta)/(V_0^3/2r_0(\Gamma-1))$ in **(c)** and sound speed $V_s(R,\theta)/V_0$ in **(d)** for $\lambda = 0.5$, $\nu = 120$, $\alpha = 10$, $\delta = 4$, $\epsilon = 2$, $\mu = -1$

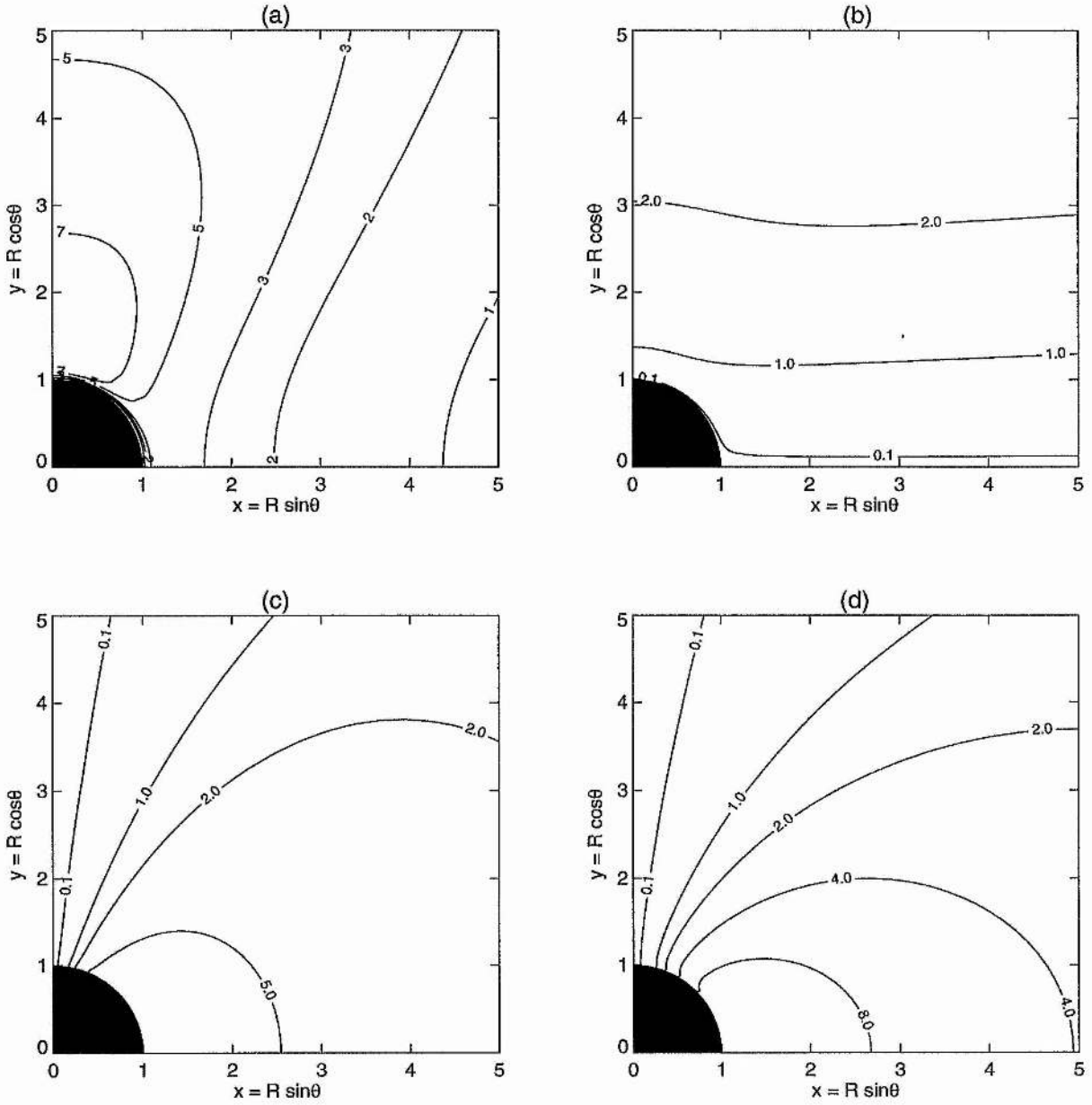

Figure 3.14: Contour plots of the temperature $10^{-3}T(R,\theta)/T_0$ in **(a)**, Mach number $M(R,\theta)$ in **(b)**, azimuthal velocity $V_\phi(R,\theta)/V_1$ in **(c)** and toroidal magnetic field $10^2 B_\phi(R,\theta)/B_1$ in **(d)** for $\lambda = 0.5$, $\nu = 120$, $\alpha = 10$, $\delta = 4$, $\epsilon = 2$, $\mu = -1$

3.6 Mass Loss and Angular Momentum Loss

The mass efflux, $\dot{m}(\theta)$ was defined in Sect.3.2.2 as the mass loss rate per infinitesimal solid angle $d\Sigma$. In this model, where all stream/fieldlines are open and there are no dead zones present, the whole of the outflow is lost from the central object and contributes for the rate of mass loss. We thus only need to integrate Eq.(3.32) in solid angle to obtain the mass loss rate, $\dot{M}$, an important quantity in stellar astrophysics.

$$\dot{M} \equiv \frac{dM}{dt} = 2\int_0^{2\pi}\int_0^{\pi/2} \dot{m}(\theta)\sin\theta d\theta d\phi, = 4\pi\rho_0 V_0 r_0^2 \int_0^{\pi/2} \sqrt{1+\mu\sin^{2\epsilon}\theta}\sqrt{1+\delta\sin^{2\epsilon}\theta}\sin\theta d\theta, \tag{3.98}$$

where the factor 2 is included to account for both hemispheres. The last integral in the above equation is in general difficult to solve for any value of ϵ. We shall take for simplicity $\epsilon = 1$, thus yielding

$$\dot{M} = 4\pi\rho_0 V_0 r_0^2 \int_0^{\pi/2} \sqrt{1+\mu\sin^2\theta}\sqrt{1+\delta\sin^2\theta}\sin\theta d\theta. \tag{3.99}$$

In the case of spherically symmetric density distribution ($\delta = 0$) the above equation is easily integrable and we get

$$\dot{M} = 2\pi\rho_0 V_0 r_0^2, \quad \text{for } \mu = -1 \tag{3.100}$$

$$\dot{M} = 2\pi\rho_0 V_0 r_0^2 \left[1 + \frac{1+\mu}{\sqrt{-\mu}}\ln\left(\frac{1+\sqrt{-\mu}}{\sqrt{1+\mu}}\right)\right], \quad \text{for } -1 < \mu < 0 \tag{3.101}$$

When μ approaches 0 the mass loss given by this last expression approaches $4\pi\rho_0 V_0 r_0^2$.

Another possibility is to take $\delta \neq 0$. The mass loss is now

$$\dot{M} = 4\pi\rho_0 V_0 r_0^2 \left[\frac{(1+\delta)^{3/2}-1}{3\delta}\right], \quad \text{for } \mu = -1 \tag{3.102}$$

$$\dot{M} \simeq 2\pi\rho_0 V_0 r_0^2 \left[1 + \frac{1+\delta}{\sqrt{\delta}}\sin^{-1}\sqrt{\frac{\delta}{1+\delta}}\right] \quad \text{for } |\mu| < 0.1 \tag{3.103}$$

This last expression was deduced under the assumption that $|\mu| \ll 1$, for which the mass efflux can be approximately written as $\dot{m}(\theta) \simeq \sqrt{1+\delta\sin^{2\epsilon}\theta}$. It yields $\dot{M} \simeq \pi\rho_0 V_0 r_0^2$ when δ approaches 0, similarly to Eq.(3.101).

Table 3.2 shows some values of the mass loss as given by Eqs.(3.100),(3.101) and (3.102),(3.103), for $\epsilon = 1$ and typical values of δ and μ. Note that the mass loss is quite sensitive to variations in δ, and is higher the more the equatorial density exceeds the density at the poles. In other

δ	μ	$\dot{M}/2\pi\rho_0 V_0 r_0^2$	Equation
0	-1	1.00	(3.100)
0	-0.5	1.62	(3.101)
0	-0.1	1.93	(3.101)
0	-0.01	1.99	(3.101)
0	-1	1.00	(3.100)
1	-1	1.22	(3.102)
10	-1	2.37	(3.102)
10^3	-1	21.11	(3.102)
0.1	< -0.1	2.06	(3.103)
1	< -0.1	2.57	(3.103)
10	< -0.1	5.40	(3.103)
10^3	< -0.1	49.72	(3.103)

Table 3.2: Mass losses for $\epsilon = 1$ and different values of δ and μ

words, density anisotropies that favour a concentration of material around the equator result in high mass loss rates. There is also a slight increase of $\dot{M}$ with the decrease of $|\mu|$, but only within a factor of two. These conclusions should still be valid for values of $\epsilon \neq 1$, since the form of the mass efflux does not change appreciably with the variation of ϵ (see Fig.3.2(a)).

Analagously, the rate of angular momentum loss, $\dot{J}$, can be obtained by integrating the angular momentum efflux, $\dot{l}(\theta)$ as defined by Eq.(3.50), in solid angle. Thus,

$$\dot{J} = 4\pi\lambda\alpha^2\rho_0 V_0^2 r_0^3 \int_0^{\pi/2} \sqrt{1+\mu\sin^2\theta}\,\sin^3\theta d\theta, \tag{3.104}$$

where we've taken again $\epsilon = 1$ for simplicity. After some straigthforward manipulation

$$\dot{J} = \pi\lambda\alpha^2\rho_0 V_0^2 r_0^3, \quad \text{for } \mu = -1 \tag{3.105}$$

$$\dot{J} \simeq \frac{8\pi}{3}\lambda\alpha^2\rho_0 V_0^2 r_0^3, \quad \text{for } |\mu| < 0.1 \tag{3.106}$$

For $\epsilon = 1$, the angular momentum loss rate increases by a factor of $8/3 \simeq 2.7$, when μ goes from -1 to values close to zero.

3.7 Conclusions

We have presented in this chapter a new set of solutions of the steady axisymmetric MHD equations relevant to stellar wind problems. They represent the most general separable solutions of Eqs.(3.1)-(3.6) with helicoidal geometry ($V_\theta = B_\theta = 0$).

Analogously to the case with no magnetic field, we have been able to obtain the general latitudinal dependences of the different quantities and these involve only the anisotropy parameters, δ, ϵ, μ, introduced in the previous chapter. The other three parameters of the problem, which come about in the solution for the radial functions, are λ and ν, together with α, a measure of the strength of the magnetic pressure. Altogether, there are six dimensionless parameters which control the general form of the solution.

The degree of collimation, together with the anisotropy in the density distribution, is effectively controlled by δ, ϵ and μ. This model could thus be applied to polar coronal holes, stellar and extragalactic jets and even star-forming regions. The solution for $\mu = -1$ has zero radial velocity at the equator with a continuous radial magnetic field across the equator. A discontinuity and associated current sheet arises for $\mu \neq -1$. Also, the angular velocity of the roots of the fieldlines at the surface of the central object is such that it reproduces qualitatively the observations only for $\epsilon > 1$.

Topologically, there are two distinct critical points present. The first one is the usual Alfvenic point and corresponds to the point where the radial velocity of the outflow equals the radial Alfvenic velocity. All solutions pass through this high-order singularity and it corresponds to an improper node or star-type point. There is a second critical point present downstream from this first one. It is an X-type critical point (or saddle point) and is responsible for filtering a single solution corresponding to a vanishing pressure at infinity — the wind-type solution. At this critical point, the r-component of the flow speed equals the slow/fast MHD mode wave speed in that direction.

The variation of ϵ is limited to our ability to find solutions that cross both these critical points and still satisfy the boundary conditions at the base of the atmosphere. Furthermore, because the field/streamlines are constrained to keep a helicoidal geometry, the pressure gradient for large distances has to be sufficiently large to balance the dominant tension force. Thus, in some cases the solution is not valid (*i.e.* corresponds to negative pressure) outside a cone around the polar axis. This limitation disappears for $\alpha \leq 20$.

There is a drastic change in the nature of the solution from low to high values of α. The solutions for low α manifest all the characteristics of a typical hydrodynamic wind, namely very large accelerations at the base of the atmosphere, heating rate and temperature decaying very rapidly with distance. The magnetically dominated cases ($\alpha \gg 1$) show lower accelerations at the base of the atmosphere, a more isotropic distribution of the heating rate and an almost isothermal atmosphere for large distances.

Density anisotropy (or δ) greatly favours the acceleration of the wind close to the base, while

the strength of rotation (or λ) and the gravitational field (or ν) slows down the initial speed. The global solution seems to be quite insensitive to variations in ϵ. The influence of μ, on the other hand, is such that a decrease of $|\mu|$ not only diminishes the relative importance of the magnetic effects by decreasing the size of the magnetic lever arm, R_*, but also increases the value of the initial acceleration as well as the asymptotic radial velocity for large distances. The total heating and the asymptotic plasma temperature increase for lower values of $|\mu|$.

Chapter 4

Applications to the Solar Wind

4.1 A Polar Coronal Hole

4.1.1 Observations

Low emission areas on the solar surface were firstly recognized by Withbroe et al (1971) using EUV observations carried out during the total solar eclipse of March 1970. At this time the Sun was near maximum activity. The existence of these coronal holes (CH's) of negligible electron density was later confirmed by Altschuler and Perry (1972) using a method based on K-coronameter data. All of these CH's were low latitude ones (within 60° from the equator). By superimposing maps of the coronal electron density with the calculated potential magnetic field, Altschuler et al (1972) concluded that CH's are associated with a weak and diverging magnetic field.

From X-ray images of the solar corona, Krieger et al (1973) identified a particular CH which showed a density scale height a factor of two smaller than in the surrounding closed regions. Wind measurements for the appropriate period were traced back to the Sun. A good agreement between the longitude of the solar surface of a recurrent high speed stream and the position of the hole was found. This suggested an association of equatorial coronal holes with high-speed streams.

For a particular hole observed by Skylab during the period 1973 June 29 to July 13 (*i.e.* roughly 2 years before solar minimum), Munro and Jackson (1977) – hereafter MJ – made a detailed study of its properties. These can be summarized as follows.

- The boundary of the CH is symmetric about the polar axis and nearly radial from 3 to $6R_\odot$.
- At these heights the boundary is located at $\simeq 25°$ latitude, while near the solar surface it doesn't go below 65°. This means that the increase of the hole's cross-sectional area from the surface to about $3R_\odot$ is 7 times greater than for a radial boundary.
- Radiation arising from the hole can be interpreted in terms of an axisymmetric density distribution which increases with colatitude.

- Use of a spherically symmetric model yields: (i) a distribution of velocities within the hole which shows a transition from subsonic to supersonic between 2.2 and $3R_\odot$; (ii) a temperature profile that increases with height from the surface to at least $2.5R_\odot$.

4.1.2 Parameters

The role of the magnetic field in MJ analysis is assumed passive, in the sense that it only defines the geometry of the coronal hole. We will thus apply the hydrodynamic model developed in Chapter 2 to this CH. The parameters λ, ν, ϵ, μ and δ have to be determined.

Assuming that most of the increase of the hole's boundary has ocurred between the surface and $2R_\odot$, we can take this boundary as almost radial from this radius outwards. For this range of distances, the aperture of the boundary is located at $\theta \simeq 65°$, as suggested by observations (see Sect.4.1.1). Such a geometry can be modelled using streamlines which are straight lines, as defined in our basic model. In other words, the validity of the model is restricted to $R \geq 2$.

To reproduce the position angle of the polarization brightness (a measure of the density within the hole) MJ have chosen a functional form for the density equivalent to Eq.(2.24), with $\epsilon = 1$. The remaining parameter was adjusted as $\delta = 2.14$. Their choice was made in order to fit the observations to a high degree of accuracy. The fact that it is reproducible by the above model means that the analysis developed in Chapter 2 has relevant solar applications.

Assuming that the wind emanating from the polar hole is similar to the high-speed streams that flow from equatorial CH's, MJ have estimated that the velocity should be of the order of $V \simeq 86\ \mathrm{km\,s^{-1}}$ at $2R_\odot$. For the equatorial rotational speed of the Sun, we've taken $V_\phi(R = 1, \theta = 90°) \simeq 2\ \mathrm{km\,s^{-1}}$ (see page 180 of Allen (1973)). This value is based on the rotation of sunspots. Since by Eq.(2.47) V_ϕ goes as $1/R$, then we must have $V_\phi(R = 2, \theta = 90°) \simeq 1\ \mathrm{km\,s^{-1}}$. Thus most of the contribution to the total velocity V comes from V_r and we can take $V_0 = V_r(R = 2, \theta = 90°) \simeq 86\ \mathrm{km\,s^{-1}}$. Using Eqs.(2.17), (2.18), with $r_0 = 2R_\odot$ we find $\nu = 5.08$. Also, $V_1 = \sqrt{1+\delta}\, V_\phi(R = 2, \theta = 90°) \simeq 1.8\ \mathrm{km\,s^{-1}}$ which gives $\lambda = 0.02$ from Eq.(2.16).

The last parameter to be determined is μ. From solar wind measurements near sunspot minimum carried out by Pioneer 10 and 11, Mihalov et al (1990) were able to estimate the latitudinal gradient of the solar wind velocity. At the time of measurements, Pioneer 10 was located at $\theta = 86°$ and measured an almost constant velocity of $400\ \mathrm{km\,s^{-1}}$ while Pioneer 11 was at $\theta = 73°$ and measured a speed of $620\ \mathrm{km\,s^{-1}}$. This corresponds to an average gradient

$$\left(\frac{\partial V_r}{\partial \theta}\right)_{\theta \simeq 80°} = -17\ \mathrm{km\,s^{-1}deg^{-1}} = -974\ \mathrm{km\,s^{-1}rad^{-1}} \tag{4.1}$$

Differentiating Eq.(2.46) with respect to θ and dividing the result term by term by this same equation we obtain an equation giving μ in terms of ϵ, δ, θ_0 and $Q = ((\mathrm{d}v_r/\mathrm{d}\theta)/v_r)_{\theta_0}$

$$\mu = \frac{(1+\delta\sin^{2\epsilon}\theta_0)Q + \delta\epsilon\sin^{2\epsilon-1}\theta_0\cos\theta_0}{\epsilon\sin^{2\epsilon-1}\theta_0\cos\theta_0 - (1+\delta\sin^{2\epsilon}\theta_0)Q\sin^{2\epsilon}\theta_0}. \tag{4.2}$$

After substituting for $\epsilon = 1$, $\delta = 2.14$, $\theta_0 = 80°$ and $Q \simeq -974/510\,\mathrm{rad}^{-1}$, this yields $\mu = -0.82$. Use of this value of μ to model the above CH, means that we're assuming a constant gradient from $\theta = 80°$ to at least the boundary of the coronal hole at $\theta = 65°$. The fact that both set of observations are near sunspot minimum helps to justify the use of data from around 1986 on observations of 1973.

We should point out that this increase in latitude of the average solar wind speed has been attributed to the latitudinal dependence of high-speed streams (Hundhausen et al., 1971). This is confirmed by observations carried out by Pioneer Venus and IMP 8 between 1984 and 1987 (Gazis, 1993). The solar wind speed showed little latitude dependence in 1984 and 1985, while strong latitude gradients occurred in 1986 and 1987. During the later of these periods (solar minimum), high-speed streams were excluded from the vicinity of the solar equator and the wind was mostly a low-speed one. At higher latitudes, the solar wind exhibited a usual stream structure with two high-speed streams per solar rotation. The latitude gradients at the boundaries of these high-speed streams were high near the equator.

Recent observations from *ULYSSES* on its way to the solar south pole identify a recurrent high speed stream at different heliographic latitudes (Bame et al., 1993). An increase with latitude of the outflow speed is reported. A corresponding latitudinal gradient of around 10 $\mathrm{km\,s^{-1}}$ deg^{-1} is inferred between $57° < \theta < 68°$. Such an estimate is similar to the value used above. For regions closer to the solar equator, namely $\theta \simeq 76°$, this gradient reaches a much higher value of 100 $\mathrm{km\,s^{-1}}$ deg^{-1}. Also, there is a measurable negative gradient of the average proton distance with heliographic latitude of around -0.1 cm^{-3} deg^{-1}, over a 24° range. These observations constitute the first direct measurement of wind speeds and densities for regions appreciably far from the ecliptic. They confirm the general trend found in the general solution presented in Chapter 2. Outflow velocities increase with latitude while densities are higher near equatorial regions than at the poles. The implication of such a collection of data in terms of models described in this work will be addressed in Sect. 4.3.

4.1.3 Solution

In summary, the parameters for this particular model are,

- $\lambda = 0.02$
- $\nu = 5.08$
- $\epsilon = 1$
- $\delta = 2.14$
- $\mu = -0.82$

Figure 4.1 shows the profiles relevant for MJ's coronal hole and obtained from the solution deduced in Chapter 2 with the above mentioned parameters.

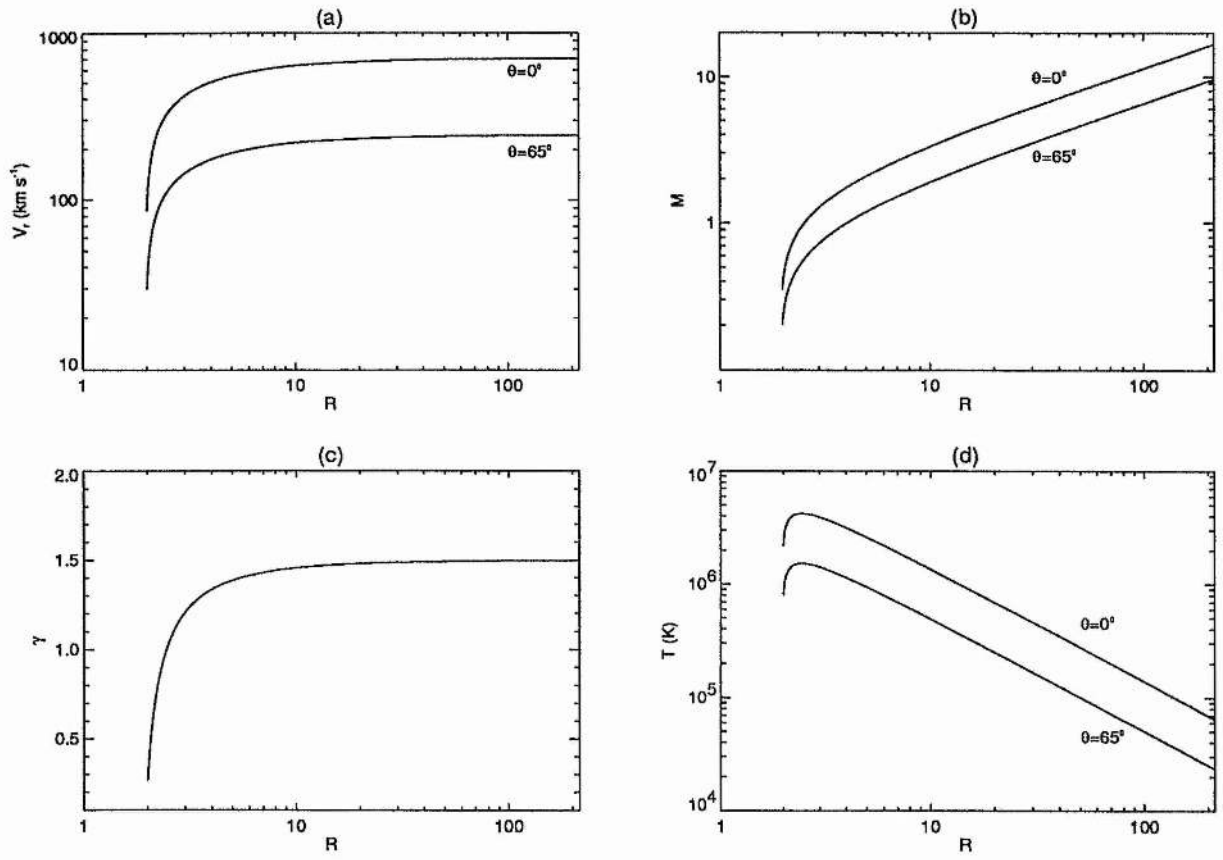

Figure 4.1: Radial velocity in **(a)**, Mach number in **(b)**, polytropic index in **(c)** and temperature in **(d)** for the polar coronal hole reported by Munro and Jackson (1977). The parameters are $\lambda = 0.02$, $\nu = 5.08$, $\delta = 2.14$, $\epsilon = 1$, $\mu = -0.82$

The radial velocity at the polar axis (Fig.4.1(a)) reaches $\sim$ 700 km s^{-1} at 1 a.u., while for the streamline limiting the hole ($\theta = 65°$) it attains $\sim$ 240 km s^{-1}. The first of these values is typical of high-speed streams measured at the ecliptic, while the later is below the average velocity for the slow solar wind (see Table 1.1). Also, if the reports from *ULYSSES* are correct, then we should expect an average wind speed over 850 km s^{-1} for regions close to the south pole of the Sun. Again, this is higher than our model predicts for $\theta = 90°$. These discrepancies might be associated with the assumption of straight streamlines used in the model. This results in a smaller acceleration than would be expected if the streamlines were allowed to diverge towards the equator.

A more rigorous fitting to the geometry of this particular hole has been assumed by MJ. They've used for the cross-sectional area of the hole, $A(R)$, the following expression

$$A(R) = A_0 R^2 k(R). \tag{4.3}$$

Here $A_0 = A(R = 1)$ and $k(R)$ is an empiric function proposed by Kopp and Holzer (1976) in the context of the geometry of flow-tubes. This function is unity when the tube is radial (e.g k(1)=1) and greater than one when the boundary of the tube diverges towards the equator. For this particular coronal hole, MJ found that $k(R)$ attains an almost constant value of 7.26 beyond $3R_\odot$, while most of the increase on k has ocurred below $2R_\odot$. Also, $k(R = 5)/k(R = 2) = 1.38$, while our model implies that $k(R) = 1$ throughout.

The transition from subsonic to supersonic flow occurs around $2.6R_\odot$ along the axis while at the boundary of the hole this occurs for $R \simeq 4.1R_\odot$ (Fig.4.1(b)). We recall that MJ's analysis predicted that the sonic point should lie between 2.2 and $3R_\odot$.

As expected, there is intense heating close to the base of the flow, where $\gamma < 1$ (Fig.4.1(c)). This corresponds to the region where the temperature is increasing with distance (Fig.4.1(d)) until it reaches a maximum near $R \simeq 2.5R_\odot$, as suggested by MJ's analysis. This maximum corresponds to around $4.2 \times 10^6\ K$ and $1.5 \times 10^6\ K$ for the polar axis and the boundary of the hole, respectively. From then on the temperature decays monotonically. At the orbit of the earth it varies between $2.4 \times 10^4\ K$ and $6.5 \times 10^4\ K$. These are just below typical values for high-speed streams (see Table 1.1). The value of γ, on the other hand, tends asymptotically to $\gamma = 3/2$, which corresponds to the Parker polytrope (Parker, 1958a).

In summary, the hydrodynamic model applied to MJ's coronal hole yields values for the velocity and temperature which agree reasonably well with his predictions and also with the measured values of the solar wind parameters at the earth's orbit (Feldman et al., 1977). The critical assumption has been the use of straight lines to model the coronal hole boundary.

4.2 Rotation of Photospheric Magnetic Features

4.2.1 The Snodgrass Profile

As discussed in Sect. 3.2.2, $\Omega(\theta)$ represents the angular velocity of the roots of the fieldlines at the base of the photosphere. This function can be compared with the rotation law of sunspots and photospheric magnetic fields. Snodgrass (1983) determined the rotation rate of magnetic features in the solar photosphere by cross correlating magnetograms from observations made over successive days. He found this rotation to be steady over the solar surface and independent of field strength, for the 15.5 yr. period of observations. Also there wasn't any measurable variation with time, something that supports the steady-state assumption used throughout this work. By fitting his observations with the functional form

$$\Omega(\theta) = a + b\cos^2\theta + c\cos^4\theta, \tag{4.4}$$

where θ is again the co-latitude, and using a least-squares method, he found $a = 2.902, b = -0.464$, $c = -0.328\ \mu\text{rad}\,\text{s}^{-1}$. The variance of these means ranges from $\sim 0.1\%$ at low latitudes to $\sim 1.1\%$

near the poles. In addition there is a slight dimple at the equator ($\sim 8\ \mathrm{m\,s^{-1}}$) not reproducible by the above expression. This profile agrees with the sunspot results of Newton and Nunn (1951) at sunspot latitudes.

4.2.2 Parameters

In order to compare the Snodgrass profile with our form of $\Omega(\theta)$, we must expand the right-hand side of Eq.(3.47) in powers of $\cos\theta$. After some straightforward manipulation, we find the first three terms in this expansion

$$\frac{r_0 R_*^2}{\lambda V_0 \alpha^2}\Omega(\theta) = \frac{1}{\sqrt{1+\delta}}\left[1 + \left(\frac{\delta-\epsilon+1}{2(1+\delta)}\right)\cos^2\theta + \left(\frac{3\delta^2 - 2(\epsilon^2+2\epsilon-3)\delta + \epsilon^2 - 4\epsilon + 3}{8(1+\delta)^2}\right)\cos^4\theta\right], \tag{4.5}$$

valid close to the equator. To obtain the best fit to zeroth order let us equate the constant term in Eq.(4.5) with a from Eq.(4.4). Also the ratio between the first and second terms and the first and third terms in Eq.(4.5) can be equated to $r_1 = a/b$ and $r_2 = a/c$, respectively. Altogether we have a system of three equations of the form

$$\frac{\lambda V_0 \alpha^2}{r_0 R_*^2} = \sqrt{1+\delta}\, a, \tag{4.6}$$

$$2(1+\delta) = (\delta - \epsilon + 1) r_1, \tag{4.7}$$

$$8(1+\delta)^2 = (3\delta^2 - 2(\epsilon^2+2\epsilon-3)\delta + \epsilon^2 - 4\epsilon + 3) r_2. \tag{4.8}$$

This system yields, after substitution for the Snodgrass values of $a = 2.902 \times 10^{-6}\ s^{-1}$, $r_1 = -2.902/0.464$ and $r_2 = 2.902/0.328$, $\epsilon \simeq 1.35$, $\delta \simeq -0.05$ and $\lambda V_0 \alpha^2 / r_0 R_*^2 \simeq 2.884 \times 10^{-6}\, s^{-1}$. A negative value of δ corresponds to a density distribution that increases from pole to equator in contradiction with the behaviour found for Munro and Jackson's coronal hole. However, under such conditions the wind is unable to accelerate to high terminal speeds.

In the purely hydrodynamic case, we've seen in Sect. 2.3 that the outflow is monotonically accelerating in the region $R > 1$ only if $\delta > \delta_0$, where δ_0 is defined by Eq.(2.45). In most cases of interest $\delta_0 > 0$. Thus, a hydrodynamic wind cannot accelerate if the density at the pole is higher than at the equator, for the same radial distance ((Tsinganos and Vlastou-Tsinganos, 1988; Lima and Priest, 1993)). With the inclusion of the magnetic field, the acceleration at the base of the atmosphere depends critically on $\delta\nu^2$, similarly to Eq.(3.90). If $\delta < 0$, this acceleration can be low enough resulting in a speed at the Earth's orbit below the required range of values for the solar wind. Such a property was discussed in Hu and Low (1989) where, by assuming a dipolar field, it was shown that if the density decreases towards the poles at a fixed radial distance (*i.e.* $\delta > 0$) the polar wind speed along open magnetic field lines can accelerate monotonically to high

terminal values. If the density is either independent of latitude ($\delta = 0$) or decreases towards the equator ($\delta < 0$) there is less internal energy per unit mass over the pole, precisely where the plasma can be accelerated out along open magnetic field lines. In these cases, the resulting terminal speeds are too low. Bearing this in mind, we shall take a positive value of δ instead, even though this might correspond to a worst fit to the rotation profile given by Snodgrass (1983).

The base of the atmosphere will be taken as the surface of the Sun. For the velocity at the base we will use $V_\phi(R = 1, \theta = 90°) \simeq 2\ \mathrm{km\,s^{-1}}$ as in Sect.4.2 and $V_0 = V_r(R = 1, \theta = 0°) \simeq 5\ \mathrm{km\,s^{-1}}$. This last value is based on observations of Doppler shifts of certain spectral lines formed at the coronal base. These shifts seem to be caused by the outflow of the solar wind (Withbroe, 1988). Using the above values we obtain $\nu = 124$.

The value of ϵ is going to be adjusted to fit the Snodgrass profile as best as possible. In fact, we can re-write Eq.(4.7) as

$$\epsilon = \left(1 - \frac{2}{r_1}\right)(1 + \delta). \tag{4.9}$$

For a given value of δ the above expression gives the value of ϵ that best reproduces the ratio $r_1 = a/b$ between the first two coefficients of the Snodgrass profile. The corresponding value of μ can be obtained from Eq.(4.2), where again we've taken Q from Mihalov et al (1990).

A difficult value to constrain is the parameter α, the inverse of the Alfvén Mach number at the base of the atmosphere. We will take $1 < \alpha < 10$, to represent an average value over the whole of the photosphere. From Eqs.(3.48), (3.59) we can write

$$\lambda = \frac{\sqrt{1+\delta}}{\alpha^2} \frac{V_\phi(R = 1, \theta = 90°)}{V_0} \left(\frac{1 - 1/\alpha^2}{1/R_*^2 - 1/\alpha^2}\right). \tag{4.10}$$

The value of R_*, the Alfvenic radius, is still unknown. A first approximation can be taken as $R_* = 1$, which is reasonable since $\alpha \leq 10$ (see Table 3.1). This gives us a first estimate of λ by direct substitution in the above equation. With all six parameters known (δ, ν, ϵ, μ, α, λ) we can integrate Eqs.(3.68), (3.69) and obtain a better approximation to R_*. Going back to Eq.(4.10) this yields our final value of λ.

4.2.3 Solution

Table 4.1 shows the parameters used in three representative models. We plot in Fig.4.2 the angular velocity of the roots of the fieldlines at the photosphere for the Snodgrass profile (S) and each of the models. Figure 4.3 shows the radial velocity, temperature, Mach number and Alfvenic Mach number as a function of distance from the Sun.

Model A corresponds to the best fit to $r1 = a/b$ of the Snodgrass profile, but using a value of δ just above zero. We've taken $\alpha = 2$ and note the low value of $V_r(1\ a.u.)$ in Fig.4.3(a). Keeping

Model	ν	δ	ϵ	μ	α	λ	R_*
A	124	0.01	1.31	−0.68	2	0.12	1.066
B	124	0.4	1.09	−0.68	6	0.017	1.137
C	124	0.5	1.04	−0.68	2	0.12	1.002

Table 4.1: Parameters and position of Alfvén radius, R_*, for three different Models A, B, C

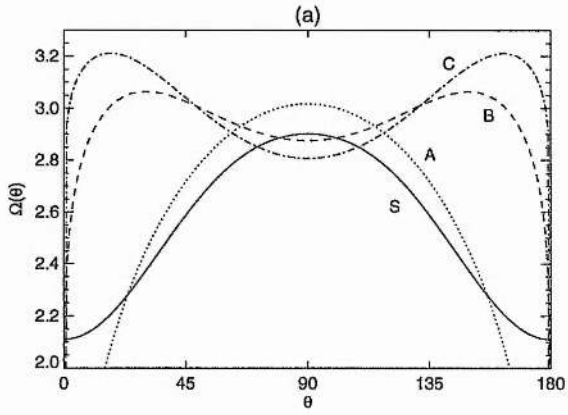

Figure 4.2: Comparison of the Snodgrass profile for the rotation of photospheric magnetic features (S) with the profile obtained by using Eq.(3.47) with the parameters of Models A,B,C (see Table 4.1)

the other parameters fixed we can only find solutions for $\alpha \leq 8$ with a maximum terminal value of $V_r(1\ a.u.) \simeq 100\ \mathrm{km\,s^{-1}}$ for $\alpha = 8$, which is still too low. Model B is a more realistic one at least in terms of terminal speed. However, δ is now high enough so that the Snodgrass profile is not well reproduced specially for latitudes higher than about 40° (see Fig.4.2). Model C corresponds to higher asymptotic velocities but even higher deviations from the Snodgrass profile.

From these elucidative examples, it is obvious that the terminal velocity is too low for values of δ that reproduce well the rotation profile of magnetic features (as in Model A). It starts to approach the observed values at the orbit of the Earth when δ is too high for a good fit of this profile. Even though Models B,C give a poor representation of the Snodgrass law for high latitudes, Fig. 4.2 shows that the agreement is good for latitudes below 35°, where most of the sunspots are confined. Figure 4.3(b) shows that temperatures at the Earth are typical of the low-speed solar wind (see Table 1.1), while the sonic point lies between 2 and $3R_\odot$ for Models B,C and much further out ($\sim 50R_\odot$) for Model A (Fig.4.3(c)). This last example should be discarded as a realistic description of the solar wind.

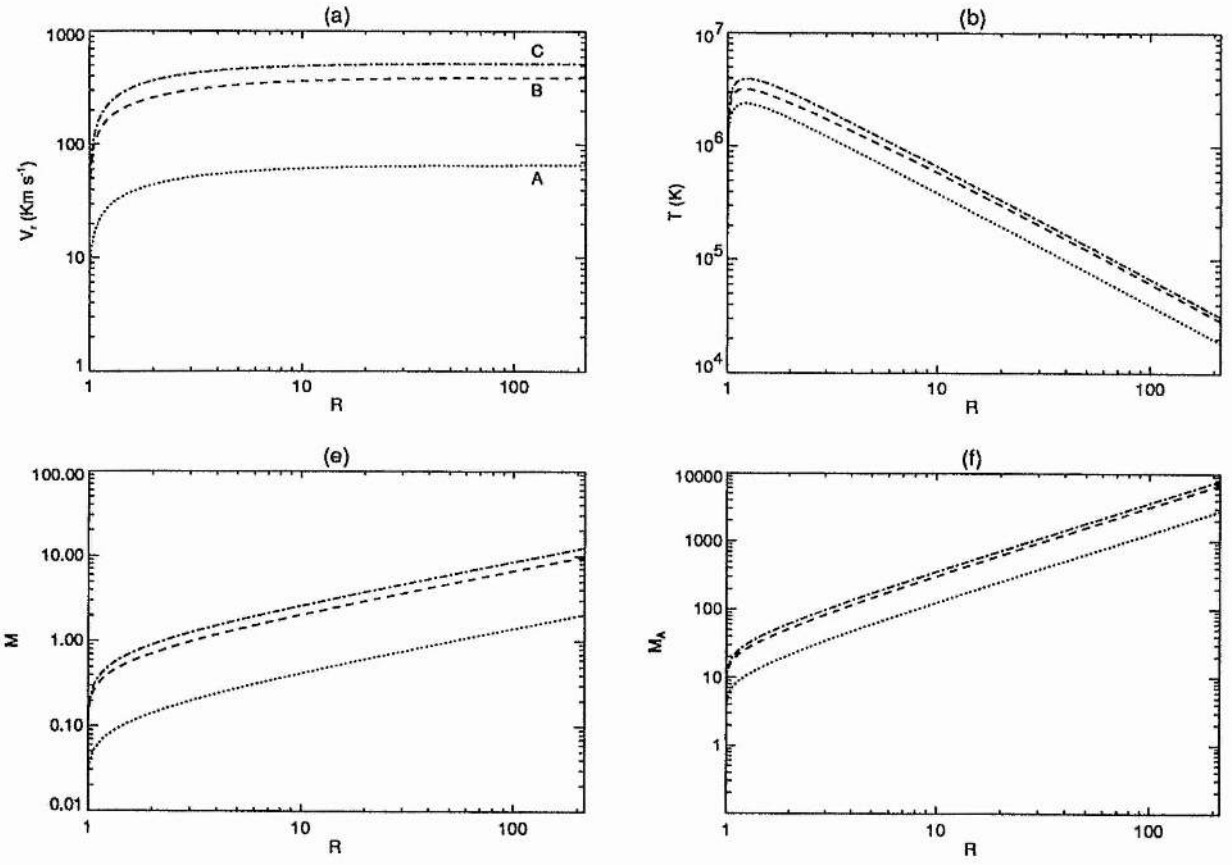

Figure 4.3: Radial velocity in **(a)**, temperature in **(b)**, Mach number in **(c)** and Alfvenic Mach number in **(d)** for Models A,B,C

We should stress at this point that we've only taken $\alpha > 1$. Better agreement might be achieved if we assume $\alpha < 1$. Under this limit, both critical points are close to each other and below the base of the atmosphere (see Tsinganos and Trussoni (1991)). Such a solution is qualitatively analogous to a purely hydrodynamic one and is better reproduced using the model described in Chapter 2.

Since the base of the solar wind is in some way connected to coronal holes, then we should really be comparing the theoretical rotation curve to the observed rotation of coronal holes. This seems to be much flatter then the corresponding profiles for photospheric magnetic fields or recurrent sunspots (Wagner, 1975), suggesting a better fit to the models presented in this section.

Finally, instead of making use of an expansion to get the approximate form of $\Omega(\theta)$, given by Eq. (4.5), an alternative approach would be to fit the observations with a theoretical curve, by varying the relevant parameters. This could be pursued using the simpler hydrodynamic approach.

4.3 The Variation of the Solar Wind with Latitude: Data from *ULYSSES*

4.3.1 Observations

On its journey to the south pole, *ULYSSES* has been collecting data in the past few months and providing a new insight into the global structure of the solar wind. On the basis of the variations of its characteristics with latitude, McComas et al (1994) assign four distinct regions. For low latitudes ($< 13°S$) the flow is dominated by a higher density, slow solar wind from the solar coronal streamer belt. The second region extending down to $30°S$ corresponds to mixed observations between a low-density, high-speed wind from the southern polar coronal hole and the high-density, slow solar wind (Bame et al., 1993). The third region, from around 30° to $36°S$, still shows influence of these two different domains, but now the probe is less influenced by the streamer belt flow. Finally, from $36°S$, *ULYSSES* has remained immersed in the high-speed solar wind flow due to the southern polar coronal hole. The above classification refers only to data up to $56°S$, although it is expected that the probe will remain under the influence of the coronal hole flow down to the maximum southern latitude of 80°, to be reached in September 94.

In any of the above domains, a general trend is observed. The flow speed increases with latitude and the density drops as we approach the south pole. This is the case for a recurrent high-speed stream observed between July 1992 and June 1993, when *ULYSSES* travelled from around 13° to $34°S$ (Bame et al., 1993). The maximum speed at the peaks ranges from around 500 $\mathrm{km\,s^{-1}}$ just below the ecliptic to values close to 900 $\mathrm{km\,s^{-1}}$ at a latitude of 34° S. The corresponding latitudinal gradient is higher in a small region around 14° S (100 $\mathrm{km\,s^{-1}/deg}$). For latitudes below 22° S, this gradient decreases to about 10 $\mathrm{km\,s^{-1}deg^{-1}}$. The minimum speed of the persistent solar wind also reveals a slight increase from the equator to the south

θ	V_r(km s^{-1})	r^2n(cm^{-3})
90	450	8.6
125	700	4
145	750	3

Table 4.2: Solar wind parameters obatined by *ULYSSES* (Goldstein et al 1994)

pole. We should stress that single peaks in the speed are usually associated with passages across the probe of the high-speed stream, whereas the valleys between peaks are due to crossings of the heliomagnetic streamer belt. Also important is the detection of a substantial variation of the average proton density with latitude, decreasing towards the pole. The average gradient corresponds to -0.1 cm^{-3}deg^{-1}.

Once *ULYSSES* has become immersed in the coronal hole flow, the increase in the bulk proton speed with latitude is less pronounced. Thus, from 36° to 56°S, the average speed is 740 km s^{-1} with a slope of only 1.9 km s^{-1} deg^{-1} (McComas et al., 1994). This can be compared with values observed for high-speed streams in the ecliptic plane at 1 a.u. of roughly 700 km s^{-1} (see Feldman et al (1977) and Table 1.1). If the solar wind speed continues to increase with latitude at this rate, an average velocity of over 800 km s^{-1} is expected at 80°S.i

In summary, the emerging scenario is that of a rapid increase of the outflow speed with latitude up to around 35°S followed by a substantially smaller gradient from then on. The density (scaled to 1 a.u.) drops from an ecliptic value of around 9 cm^{-3} to 3 cm^{-3} for latitudes of 60°S. This decrease is also less pronounced for higher latitudes than near the ecliptic (see also Phillips et al (1994), Goldstein et al (1994)).

Another useful piece of information regards observations of latitude gradients in the radial component of the heliospheric magnetic field (Smith et al., 1994). This component, over latitudes of 10° to 45°S and distances from 5.3 to 3.8 a.u., compares very well with measurements by the probe IMP-8 in the ecliptic at 1 a.u.. It corresponds to an observed value of around 3.5 nT. More importantly is the absence of any significative latitude gradient.

4.3.2 Possible Constraints on Parameters

We would like to estimate values for the parameters ϵ, δ and μ on the basis of the observations described above. At least down to 60°S, *ULYSSES* has revealed two distinct regions with very different latitudinal gradients of the wind speed. The frontier between these occurs for latitudes of around 35°S. Bearing this in mind, we shall take three three different sets of values from Goldstein et al (1994). Table 4.1, shows the proton bulk speed and scaled by r^2 to 1 a.u. proton number density, for the ecliptic and the latitudes of 35 and 55°S.

Let us define $\theta_0 = 107.5$ and $\theta_1 = 135$ corresponding to the middle points for the two regions. Assuming constant gradients for each of these regions, we can write

$$\frac{(\partial\rho/\partial\theta)_{\theta_0}}{(\partial\rho/\partial\theta)_{\theta_1}} = \frac{(\partial n/\partial\theta)_{\theta_0}}{(\partial n/\partial\theta)_{\theta_1}} = \left(\frac{\sin\theta_0}{\sin\theta_1}\right)^{2\epsilon-1} \frac{\cos\theta_0}{\cos\theta_1} = \frac{dn_0}{dn_1}, \tag{4.11}$$

where $dn_0 = (4 - 8.6)/(125 - 90)$ and $dn_1 = (3 - 4)/(145 - 125)$ correspond to the (constant) gradients of the number density, for the regions centered on θ_0 and on θ_1, respectively. Also,

$$\frac{(\partial\rho/\partial\theta)_{\theta_0}}{\rho(\theta_0)} = \frac{(\partial n/\partial\theta)_{\theta_0}}{n(\theta_0)} = \frac{2\epsilon\delta\sin^{2\epsilon-1}\theta_0\cos\theta_0}{1+\delta\sin^{2\epsilon-1}\theta_0} = \frac{dn_0}{n_0}. \tag{4.12}$$

Here, $n_0 = (8.6+4)/2$ corresponds to the average value of the density at θ_0, under the assumption of constant gradient. Solving Eqs.(4.11) (4.12) yields the values $\epsilon = 3.54$ and $\delta = 1.61$. To estimate μ we can compare values of V_r for two different latitudes, namely $\theta = 90°$ and $\theta = 145°$. This gives $\mu = -0.09$, resulting in low values of the latitudinal gradient of the radial component of the magnetic field (see Eq. (3.25)), as reported by Smith et al (1994).

While this method of determining the anisotropy parameters is useful to obtain first estimates, a more rigorous approach might be achieved by fitting more data points from *ULYSSES* observations to the appropriate curves.

4.4 Conclusions

In this chapter, solar observations were used to constrain the free parameters in both the hydrodynamic and magnetohydrodynamic models that were presented in Chapters 2,3, respectively.

Thus, in the case of a particular coronal hole, we've discussed the application of a purely hydrodynamic model. The restriction of keeping the streamlines straight meant that the acceleration couldn't be as high as if the lines delimiting the hole were allowed to diverge towards the equator, for low heliocentric distances. However, we still obtain reasonably good terminal speeds and temperatures.

For a magnetic model, we've taken observations of the rotation profile of photospheric magnetic features to help constrain some parameters. In this case, it seems that the best fit to this profile results in terminal speeds that are too low. If we take into account observations at the orbit of the earth, we find a poor agreement between the calculated and the observed profile at the photosphere. In any case, the models discussed are low magnetized ones.

Finally, very recent observations from *ULYSSES* heading towards the south pole of the ecliptic, have shed new light on the variation of the Solar Wind with latitude. In particular we were able to obtain more reliable estimates of the parameters introduced in this work.

Chapter 5

Conclusion

5.1 Summary

The initial motivation of this work was systematically to obtain solutions of the equations governing axisymmetric winds from astrophysical objects.

Observationally we are faced with winds that span all types, from almost spherically symmetric to highly collimated ones. The presence of equatorial disks of higher density mass is usually associated with the latter type. Thus, previous models have attempted to model such a geometry by using some free parameter, which could be included in both the velocity and density variations with latitude. This study covers the gap left by this approach and goes one step further in trying to obtain the most general separable solutions to the basic equations without any *a priori* specification on the form of the various quantities.

But to keep such a general approach mathematically tractable we had to impose some kind of restriction. In this case, the latitudinal component of the velocity field, for the hydrodynamic approach, and of both the velocity and magnetic fields, for the magnetohydrodynamic treatment, were taken as zero. Geometrically, this means that we are only concerned with helicoidal stream/fieldlines. Such a geometry is in fact suggested by several pieces of observation, namely some examples of extragalactic and stellar jets, as well as star formation regions (see Chapter 1). In common, they all manifest a high degree of collimation, which can be achieved in principle if we adopt helicoidal field lines.

The first attempt uses a purely hydrodynamic wind (Chapter 2). The solution yields five parameters. Three of these are the so-called anisotropy parameters, δ, ϵ and μ and they control the way the different quantities vary with latitude. Of the other two, λ is associated with the rotation speed of the central object and ν with its gravitational field. The main conclusions of this simple model are:

- To construct a solution that is always accelerating from the base of the atmosphere to large distances, δ must be positive. This means that density at the equator must always exceed density at the pole. Such a constraint naturally favours concentration of mass around

equatorial regions, a pre-requisite for a disk.

- Static conditions at the equator are only achieved for $\mu = -1$. Also, we always have higher radial velocities at the pole than at the equator, for an accelerated wind. This degree of collimation can be increased without limit.

- If we want to model a disk of material around the equator, its thickness can be adjusted by varying the parameter ϵ. The heating rate that consistently satisfies the basic equations decays in general from pole to equator and its latitudinal profile is more sensitive to δ and ϵ.

- The radial profiles of the different physical quantities are typical of hydrodynamic wind models, such as the initial one proposed by Parker (1958a). Thus we have a radial velocity increasing very rapidly close to the base of the atmosphere and attaining an asymptotic constant value within a few radii of the central object. This acceleration requires a heating rate mostly concentrated at small distances.

- Since no polytropic relationship between pressure and density was assumed, the effective polytropic index varies with distance.

- An application of this model has been made to a well-studied solar coronal hole (Chapter 4). The results show that velocities and temperatures at the orbit of the earth are similar to observed values for the solar wind.

The inclusion of the magnetic field introduces a sixth parameter in the analysis, α, the ratio of the radial Alfvén velocity to the radial velocity at the base of the atmosphere. Again here it is possible to find a fully separable solution. Velocity, density, pressure and heating rate depend on latitude in exactly the same way as deduced for the simpler hydrodynamic model. For this MHD solution

- The magnetic field shows a discontinuity at the equator for $\mu \neq -1$ and a corresponding current sheet.

- Only for values of $\epsilon > 1$ does the angular velocity of the roots of the fieldlines at the base of the atmosphere depend on latitude in a similar way to the observed rotation profile of photospheric magnetic features.

- Topologically there are two critical points present in the solution for the radial dependence of the outflow velocity. One of them is the familiar Alfvenic point and corresponds to a high-order singularity. It does not filter any particular solution passing through it. Downstream of this point an $X-$ type point is present. Two solutions cross it. One is always decelerating and this is not appropriate to describe a wind. The relevant one is always accelerating and corresponds to zero pressure at infinity.

- The distribution of the heating rate is more isotropic for more magnetized winds, while the temperature can be made almost constant for large distances if α is sufficiently large. This asymptotic value can also be varied by adjusting the anisotropy parameters.

- The mass loss increases with the degree of anisotropy of the density distribution (or δ) and is less sensitive to the other anisotropy parameters.

In summary, a very simple technique based on separation of variables has provided us with a powerful weapon to obtain general solutions of the two-dimensional wind equations, with a helicoidal geometry for the field/streamlines. In the case of the Sun, the observations constrain, in principle, most of the parameters of the problem. For other astrophysical winds it is a difficult task to obtain estimates for all of them on the basis of observations.

5.2 Future Work

We're experiencing an exciting new period of solar observations, with new data from *ULYSSES* on its journey outside the plane of the ecliptic helping us to visualize for the first time the global structure of the solar wind. Such data is crucial in constraining, in particular, the anisotropy parameters relevant for the solar wind that appear naturally in the equations developed during this work. We intend to carry on this task on the near future and to improve the analysis made in Sect. 4.3.

Applications to other stars could also be attempted. One crucial parameter in this type of application is the mass loss rate. We've discussed in Sect. 3.6 how this quantity depends on the various parameters of the problem. The large margins of error usually involved here (*e.g.* in T Tauri's) could pose a problem.

The most interesting question is whether this simple technique for finding separable solutions still works in the case of a general geometry of the field/streamlines (and not necessarily helicoidal). In other words, is it possible to find a general solution of the problem when both the velocity and magnetic field have all three components ? It might be necessary in this case to use as independent variables the radial distance r and the magnetic flux function $A(r,\theta)$ and to consider expansions of the relevant quantities on A (see Sauty and Tsinganos (1994)).

Appendix A

Classification of Critical Points

A first-order differential equation of the form

$$\frac{\mathrm{d}y}{\mathrm{d}x} = \frac{cx + ey}{ax + by} \tag{A.1}$$

can be written as a system of two simultaneous linear differential equations

$$\frac{\mathrm{d}x}{\mathrm{d}t} = ax + by, \tag{A.2}$$

$$\frac{\mathrm{d}y}{\mathrm{d}t} = cx + ey. \tag{A.3}$$

The point $(0, 0)$ satisfies simultaneously

$$\frac{\mathrm{d}x}{\mathrm{d}t} = 0, \quad \frac{\mathrm{d}y}{\mathrm{d}t} = 0, \tag{A.4}$$

and is thus called an equilibrium or critical point of Eq.(A.1) or the related system given by Eqs.(A.2), (A.2). Topologically, such critical points can be classified in four fundamental types, as follows,

- *saddle point* or $X-$*point* – point crossed by two critical solutions, with two different slopes.
- *node*
  - *improper node* – only two slopes are allowed. An infinite number of solutions cross the point with one of the slopes. Only one solution crosses it with the other slope.
  - *proper node* or *star point* – an infinite number of solutions cross this point, each one with a different slope.

- *spiral point* – no solution crosses the critical point. The trajectories around it are spirals.
- *center* – the trajectories correspond to circles and thus no solution crosses this critical point.

One fundamental result establishes the nature of a critical point once the roots of the characteristic equation of the linear system, Eqs.(A.2),(A.2),

$$m^2 - (a+e)m + (ae - bc) = 0, \tag{A.5}$$

are known. These are

$$m_1 = \frac{(a+e) + \sqrt{\Delta}}{2}, \quad m_2 = \frac{(a+e) - \sqrt{\Delta}}{2}, \tag{A.6}$$

where the determinant Δ is given by

$$\Delta = (a+e)^2 - 4(ae - bc). \tag{A.7}$$

Specifically, we can classify the critical point $(0,0)$ of Eq.(A.1) using the table below (Boyce and DiPrima, 1986).

Case	Nature of characteristic roots	Nature of critical point
1	$m_1 > m_2 > 0$ or $m_2 < m_1 < 0$	improper node
2	$m_2 < 0 < m_1$	saddle point
3	$m_1 = m_2$	node (proper or improper)
4	$m_1, m_2 = r \pm si$	spiral point
5	$m_1 = si$, $m_2 = -si$	center

Table A.1: Nature of critical point of Eq.(A.1)

In the case of either a saddle point or an improper node, it is straightforward to show that, in the linear approximation, the slopes of the two solutions that cross the point, s_1, s_2, are given by

$$s_1 = \frac{-(a-e) + \sqrt{(a-e)^2 + 4bc}}{2b}, \quad s_2 = \frac{-(a-e) - \sqrt{(a-e)^2 + 4bc}}{2b}. \tag{A.8}$$

Note that in this case the determinant $\Delta = (a-e)^2 + 4bc$ equals the one given by Eq.(A.7).

Bibliography

Allen, C. W. 1973, *Astrophysical Quantities*, The Athlone Press, London

Altschuler, M. D. and Perry, R. M. 1972, *Sol. Phys.* **23**, 410

Altschuler, M. D., Trotter, D. E., and Orral, F. Q. 1972, *Sol. Phys.* **26**, 354

Bachiller, R. and Gómez-González, J. 1992, *The Astron. and Astrophys. Review* **3**, 257

Bame, S. J., Goldstein, B. E., Gosling, J. T., Harvey, J. W., McComas, D. J., Neugebauer, M., and Phillips, J. L. 1993, *Geophys. Res. Lett.* **20(21)**, 2323

Bertout, C. 1989, *Ann. Rev. Astron. Astrophys.* **27**, 351

Biermann, L. 1951, *Z. Astrophys* **29**, 274

Biermann, L. 1953, *Extrait des Mem. Soc. Roy. Sci. Liège Collection, No.4* **13**, 291

Biermann, L. 1957, *Observatory* **77**, 109

Bohlin, J. D. 1976, in D. J. William (ed.), *Physics of Solar Planetary Environments*, Vol. 1 of *Proc. of the International Symposium on Solar Terrestrial Physics*, p. 114, American Geophysical Union

Bohlin, J. D. and Sheeley Jr., N. R. 1978, *Sol. Phys.* **56**, 125

Bouvier, J. 1989, *Astron. J.* **99(3)**, 946

Bouvier, J. and Bertout, C. 1989, *Astron. Astrophys.* **211**, 99

Bouvier, J., Bertout, C., Benz, W., and Mayor, M. 1986, *Astron. Astrophys.* **165**, 110

Boyce, W. E. and DiPrima, R. C. 1986, *Elementary Differential Equations and Boundary Value Problems*, p. 443, John Wiley & Sons

Chapman, S. 1957, *Smithsonian Contrib. Astrophys.* **2**, 1

Chen, H., Ringuelet, A., Sahade, J., and Kondo, Y. 1989, *Astrophys. J.* **347**, 1082

Coles, W. A., Rickett, B. J., Rumsey, V. H., Kaufman, J. J., Turley, D. G., Ananthakrishnan, S., Armstrong, J. W., Harmons, J. K., scott, S. L., and Sime, D. G. 1980, *Nature* **286**, 239

Dupree, A. K. 1986, *Ann. Rev. Astron. Astrophys.* **24**, 377

Feldman, W. C., Asbridge, J. R., Bame, S. J., and Gosling, J. T. 1977, in O. R. White (ed.), *The Solar Output and Its Variations*, p. 351, Colorado Associated University Press, Boulder

Gazis, P. R. 1993, *J. Geophys. Res.* **98(A6)**, 9391

Goldstein, B. E., Neugebauer, M., Gosling, J. T., Bame, S. J., Phillips, J. L., McComas, D. J., and Balogh, A. 1994, *Ulysses Observations of Solar Wind Plasma Parameters in the Ecliptic from* 1.4 *to* 5.4 *AU and Out of the Ecliptic*, submitted to Space Science Reviews

Gosling, J. T., Borrini, G., Asbridge, J. R., Bame, S. J., Feldman, W. C., and Hansen, R. T. 1981, *J. Geophys. Res.* **86**, 5438

Hall, G. and Watt, J. M. 1976, *Modern Numerical Methods for Ordinary Differential Equations*, Clarendon Press, Oxford

Hartmann, L., Hewett, R., Stahler, S., and Mathieu, R. D. 1986, *Astrophys. J.* **309**, 275

Hartmann, L. and Noyes, R. W. 1987, *Ann. Rev. Astron. Astrophys.* **25**, 271

Heyvaerts, J. and Norman, C. A. 1989, *Astrophys. J.* **347**, 1055

Hu, Y. Q. and Low, B. C. 1989, *Astrophys. J.* **342**, 1049

Hundhausen, A. J. 1972, *Coronal Expansion and Solar Wind*, Springer-Verlag

Hundhausen, A. J., Bame, S. J., and Montgomery, M. D. 1971, *J. Geophys. Res.* **76**, 5145

Joy, A. H. 1945, *Astrophys. J.* **102**, 168

Kopp, R. A. and Holzer, T. E. 1976, *Sol. Phys.* **49**, 43

Krieger, A. S., Timothy, A. F., and Roelef, E. C. 1973, *Sol. Phys.* **29**, 505

Lima, J. J. G. and Priest, E. R. 1993, *Astron. Astrophys.* **268**, 641

Lima, J. J. G. and Priest, E. R. 1994, *Two-dimensional models for solar and stellar winds: MHD solutions with helicoidal geometry*, to be submitted to *Astron. Astrophys.*

Linsky, J. L. 1985, *Sol. Phys.* **100**, 333

Low, B. C. and Tsinganos, K. 1986, *Astrophys. J.* **302**, 163

McComas, D., Phillips, J. L., Bame, S. J., Gosling, J. T., Goldstein, B. E., and Neugebauer, M. 1994, *Ulysses Solar Wind Observations to* 56° *South*, submitted to Space Science Reviews

Mestel, L. 1968, *Mon. Not. R. Astron. Soc.* **138**, 359

Mihalov, J. D., Barnes, A., Hundhausen, A. J., and Smith, E. J. 1990, *J. Geophys. Res.* **95(A6)**, 8231

Mundt, R. 1986, *Protostars and Planets II*, p. 414, University Arizona Press, Tucson

Mundt, R., Ray, T. P., Bührke, T., Raga, A. C., and Solf, J. 1990, *Astron. Astrophys.* **232**, 37

Munro, R. H. and Jackson, B. V. 1977, *Astrophys. J.* **213**, 874

Nash, A. G. 1991, *Astrophys. J.* **366**, 592

Neugebauer, M. and Snyder, C. W. 1966, *J. Geophys. Res.* **71**, 4469

Newton, H. W. and Nunn, M. L. 1951, *Mon. Not. R. Astron. Soc.* **111**, 413

Owen, F. N., Hardee, P. E., and Cornwell, T. J. 1989, *Astrophys. J.* **340**, 698

Paresce, F. and Nota, A. 1989, *Astrophys. J.* **341**, L83

Parker, E. N. 1958a, *Astrophys. J.* **123**, 664

Parker, E. N. 1958b, *Phys. Fluids* **1(3)**, 171

Parker, E. N. 1963, *Interplanetary Dynamical Processes*, Interscience Publishers, New York

Phillips, J. L., Balogh, A., Bame, S. J., Goldstein, B. E., Gosling, J. T., Hoeksema, J. T., McComas, D. J., Neugebauer, M., Sheeley, N. R., and Wang, Y. M. 1994, *J. Geophys. Res.* **21(12)**, 1105

Pneuman, G. W. and Kopp, R. A. 1971, *Sol. Phys.* **18**, 258

Priest, E. R. 1982, *Solar Magnetohydrodynamics*, Geophysics and Astrophysics Monographs,

Reidel Publishing Company
Reipurth, B. 1989, *Nature* **340(6228)**, 42
Rickett, B. J. and Coles, W. A. 1991, *J. Geophys. Res.* **96(A2)**, 1717
Ringuelet, A. E. and Iglesias, M. E. 1991, *Astrophys. J.* **369**, 463
Sakurai, T. 1985, *Astron. Astrophys.* **152**, 121
Sakurai, T. 1987, *Publ. Astron. Soc. Jpn.* **39**, 821
Sakurai, T. 1990, *Comp. Phys. Rep.* **12**, 247
Sauty, C. and Tsinganos, K. 1994, *Astron. Astrophys.* **287**, 893
Smith, E. J., Neugebauer, M., Balogh, A., Bame, S. J., Lepping, R. P., and Tsurutani, B. T. 1994, *Ulysses Observations of Latitude Gradients in the Heliospheric Magnetic Field: Radial Component and Variances*, ESLAB Symposium Proceedings
Snodgrass, H. B. 1983, *Astrophys. J.* **270**, 288
Suess, S. T., McComas, D. J., and Hoeksema, J. T. 1993, *Geophys. Res. Lett.* **20(3)**, 161
Trussoni, E. and Tsinganos, K. 1993, *Astron. Astrophys.* **269**, 589
Tsinganos, K. 1982, *Astrophys. J.* **252**, 775
Tsinganos, K. 1994, private communication
Tsinganos, K. and Low, B. C. 1989, *Astrophys. J.* **342**, 1028
Tsinganos, K. and Sauty, C. 1992a, *Astron. Astrophys.* **255**, 405
Tsinganos, K. and Sauty, C. 1992b, *Astron. Astrophys.* **257**, 790
Tsinganos, K., Surlantzis, G., and Priest, E. R. 1993, *Astron. Astrophys.* **275**, 613
Tsinganos, K. and Trussoni, E. 1990, *Astron. Astrophys.* **231**, 270
Tsinganos, K. and Trussoni, E. 1991, *Astron. Astrophys.* **249**, 156
Tsinganos, K. and Vlastou-Tsinganos, G. 1988, *Astron. Astrophys.* **193**, 125
Vogel, S. N. and Kuhi, L. V. 1981, *Astrophys. J.* **245**, 960
Wagner, W. J. 1975, *Astrophys. J.* **198**, L141
Waldmeier, M. 1957, *Die Sonnenkorona*, Vol. 2, Verlag Birkhaüser, Basel
Wang, Y. M., Jr., N. R. S., Nash, A. G., and Shampine, L. R. 1988, *Astrophys. J.* **327**, 427
Wang, Y. M., Nash, A. G., and Jr., N. R. S. 1989, *Astrophys. J.* **347**, 529
Weber, E. J. and Davis, L. J. 1967, *Astrophys. J.* **148**, 217
Withbroe, G. L. 1988, *Astrophys. J.* **325**, 442
Withbroe, G. L., Dupree, A. K., Goldberg, L., Huber, M. C. E., Noyes, R. W., Parkinson, W. H., and Reeves, E. M. 1971, *Sol. Phys.* **21**, 272
Withbroe, G. L., Feldman, W. C., and Ahluwalia, H. S. 1991, *Solar Interior and Atmosphere*, p. 1087, University of Arizona Press, Tucson